



DOTTORATO DI RICERCA IN FISICA

XXIV ciclo

**MAGNETISM STRUCTURE AND CHEMICAL ORDER IN THE 3D
METALS AND THEIR ALLOYS AT EXTREME PRESSURES**

Raffaella Torchio

Tutors: Prof. S. Mobilio, Prof. S. Pascarelli, Prof. C. Meneghini

Coordinatore: Prof. O. Ragnisco

Tesi realizzata con il supporto dell' Università Italo Francese

UNIVERSITÉ
FRANCO
ITALIENNE

UNIVERSITÀ
I T A L O
FRANCESE

THÈSE

Pour obtenir le grade de

DOCTEUR DE L'UNIVERSITÉ DE GRENOBLE

Spécialité : **PHYSIQUE**

Arrêté ministériel : 7 août 2006

Présentée par

Raffaella TORCHIO

Thèse dirigée par Dr. **Sakura Pascarelli** et
codirigée par **Prof. S. Mobilio** et **Prof. C. Meneghini**

préparée au sein du **European Synchrotron Radiation Facility**
dans l'**École Doctorale de Physique**

Magnétisme, structure et ordre chimique dans les métaux 3d et leur alliages à très hautes pressions

Thèse soutenue publiquement le **23 janvier 2012**,
devant le jury composé de :

Prof. Settimio MOBILIO

Professeur à l' Università degli Studi di ROMA TRE, Italie; Membre

Dr. Sakura PASCARELLI

Responsable des lignes de lumière à l' ESRF, Grenoble, France; Membre

Prof. Francesco SACCHETTI

Professeur à l' Università degli Studi di Perugia, Italie; Président

Prof. M.Luisa F-dez GUBIEDA

Professeur à l' Universidad del Pais Vasco, Espagne; Rapporteur

Prof. Stefan KLOTZ

Directeur de recherche CNRS et Professeur à l' Université P&M Curie, Paris; Rapporteur



Abstract

This thesis concerns the study of the magnetic and structural transformations that occur in the 3d metals when they are compressed up to extreme pressures. The investigation has been carried out using polarized X-ray absorption (X-ray magnetic circular dichroism or XMCD) coupled to X-ray diffraction and DTF calculations and applied to the cases of cobalt, nickel and iron-cobalt (FeCo) alloys. In particular, in cobalt we present the first experimental evidence of pressure-induced suppression of ferromagnetism and we explore the interplay between structural and magnetic changes. The case of nickel, that is structurally stable over a wide range of pressures, allows to go deeper into the interpretation of the K-edge XMCD signal, so far still unsettled. Finally the investigation of the FeCo alloys is aimed at understanding the role played by the chemical order in tuning the high pressure structural and magnetic properties.

Resumé

Cette thèse traite des transformations structurelles et magnétiques qui se produisent dans les métaux 3d quand ils sont comprimés jusqu'à des pressions extrêmes. L'étude a été réalisée en utilisant les techniques d'absorption polarisée des rayons X (Dichroïsme circulaire magnétique de rayons X ou XMCD) et de diffraction des rayons X, couplées à des calculs DFT; elle a été appliquée aux cas du cobalt, du nickel et des alliages de fer et cobalt (FeCo). En particulier, cette thèse présente la première preuve expérimentale de la suppression du ferromagnétisme du cobalt, induite par la pression, et explore la relation entre les changements structurels et magnétiques. Le cas du nickel, structurellement stable sur une large échelle de pressions, permet d'aller plus loin dans l'interprétation du signal XMCD au seuil K, encore débattue aujourd'hui. Enfin, l'enquête sur les alliages FeCo vise à comprendre le rôle joué par l'ordre chimique dans la détermination des propriétés structurelles et magnétiques en conditions de haute pression.

Riassunto

Questa tesi riguarda lo studio delle trasformazioni magnetiche e strutturali che avvengono nei metalli 3d quando sono sottoposti a pressioni estreme. L'indagine è stata svolta usando le tecniche di assorbimento di raggi X polarizzato (X-ray magnetic circular dichroism o XMCD) e diffrazione da raggi X, accoppiate a calcoli teorici DFT. Tale studio è stato applicato ai casi di cobalto, nichel e leghe di ferro-cobalto (FeCo). In particolare, per il cobalto, si presenta la prima evidenza sperimentale della soppressione del ferromagnetismo indotta dall'applicazione della pressione e si indaga la relazione tra le trasformazioni magnetiche e quelle strutturali. Il caso del nichel, strutturalmente stabile in un ampio intervallo di pressioni, permette di approfondire l'interpretazione del segnale XMCD alla soglia K, a tutt'oggi ancora dibattuta. Lo studio delle leghe di FeCo è invece volto alla comprensione di quale sia il ruolo giocato dall'ordine chimico nel determinare le proprietà strutturali e magnetiche in condizioni di alta pressione.

Contents

Abstract	5
Resumé	7
Riassunto	9
Introduction	iii
1 Magnetism and structure in the <i>3d</i> metals	1
1.1 Itinerant ferromagnetism	1
1.1.1 Basic bands theoretical results for the transition metals	4
1.2 The magnetism of alloys: covalent magnetism	7
1.3 Structure and magnetism in the <i>3d</i> metals	10
1.4 High pressure studies	12
1.4.1 Pressure effects on magnetism and structure in the <i>3d</i> metals	13
1.5 The iron case	16
2 Experimental methods	19
2.1 High-pressure experimental methods	19
2.1.1 Amagnetic diamond anvil cells	19
2.1.2 Pressure measuring methods	25
2.2 X-ray Absorption Spectroscopy	27
2.2.1 X-ray Magnetic Circular Dichroism	28
2.2.2 XMCD on the 3d metals under high pressure	30
2.2.3 Interpretation of the K-edge XMCD signal	31
2.3 Polarized XAS under high pressure: experimental details	33
2.3.1 The dispersive beamline ID24	34
2.3.2 The HP XMCD setup	36

3	Cobalt	41
3.1	Introduction	41
3.2	Extreme conditions structure and magnetism in cobalt	42
3.2.1	The HP/HT phase diagram	42
3.2.2	High pressure structure	43
3.2.3	Elastic anomalies	45
3.2.4	High pressure magnetism	46
3.3	Experiment	49
3.4	Results and discussion	49
3.5	Conclusions	57
4	Nickel	59
4.1	Introduction	59
4.2	Extreme conditions structure and magnetism in nickel	60
4.2.1	The HP/HT phase diagram	60
4.2.2	High pressure magnetism	61
4.3	Experiment	62
4.4	Results and discussion	64
4.5	Conclusions	72
5	Iron-Cobalt Alloys	75
5.1	Introduction	75
5.2	Overview of structural, magnetic and chemical properties in FeCo	76
5.2.1	The $\text{Fe}_{1-x}\text{Co}_x$ (x,T) phase diagram	76
5.2.2	Ambient magnetic properties	77
5.2.3	High pressure studies	81
5.3	Experiment	82
5.4	Results and discussion	85
5.5	Conclusions	114
6	Conclusions	117
	Bibliography	123

Introduction

The appearance of ferromagnetism in Fe(bcc), Co(hcp), and Ni(fcc) metals is one of the most fundamental questions in solid-state physics. In these transition metals, magnetism plays a fundamental role in determining the physical properties; for example, it greatly influences the crystalline structure, stabilizing bcc Fe and hcp Co instead of hcp Fe and fcc Co predicted in absence of magnetic interactions. Our modern understanding of the magnetic structure of metals relies on the Stoner-Wolfahrt model, which points out that the density of state at the Fermi level and the electronic correlations are the two most crucial factors at absolute zero temperature.

In Fe, Co and Ni magnetism arises from the partially filled spin-polarized $3d$ band whose properties are strongly determined by the crystal structure and by external factors such as temperature, magnetic field, and pressure. Therefore, exploring the stability limits of ferromagnetism as a function of these thermodynamical variables is an essential issue to get a deeper insight on its appearance.

Application of pressure is an effective way to address the complex interplay between magnetic, structural and electronic degrees of freedom. Directly acting on the interatomic distances it allows to modify the band hybridization strength thus inducing structural and magnetic instabilities. The knowledge and understanding of correlations between structure and magnetism is of paramount importance both from a fundamental and a technological point of view. First for the implications in geophysics for planetary interior's studies, being the Earth core mainly composed of iron dominated alloys; secondly for the tremendous number of technological applications in which these metals are involved such as high-density magneto-optical storage media.

The compression of interatomic distances leads to the broadening of the electronic bands, which reflects in a decreased density of state at the Fermi level. In the framework of the Stoner-Wolfahrt model this implies that at sufficiently high compression the condition for ferromagnetism stability is no longer satisfied, and ferromagnetism is lost.

In iron the collapse of ferromagnetism with pressure has been experimentally observed

in correspondence to the bcc-hcp structural phase transition around 13 GPa. An intense debate is still open to understand which, between structural and magnetic degrees of freedom, plays a driving role in the bcc ferromagnetic to hcp non-ferromagnetic transition. In cobalt, the suppression of ferromagnetism is predicted to occur with the hcp-fcc transition in the 100-150 GPa range and the pressure limits for ferromagnetism stability have been established only recently with the results presented in this Thesis and, simultaneously, by Ishimatsu and co-workers. Ni is predicted to maintain a stable fcc ferromagnetic phase up to the 10^2 GPa range, however the pressure limit of ferromagnetism in fcc Ni is still not established.

The scientific goal of this project has been to probe magnetism, structure and chemical order in 3d metals and their alloys at extreme pressures by means of K-edge polarized absorption.

K-edge X-ray Absorption Spectroscopy (XAS) and associated techniques exploiting the polarization properties of synchrotron radiation, have shown to be very useful in probing simultaneously the structural, electronic and magnetic properties of the transition metals at high pressure, for example in pure iron where they allowed to simultaneously follow the structural-magnetic phase transition from bcc-ferromagnetic to hcp- non ferromagnetic around 13 GPa. In fact, polarized X-ray absorption spectroscopy contains intrinsic structural, electronic, and magnetic probes through Extended X-ray Absorption Fine Structure (EXAFS), X-ray Absorption Near Edge Structure (XANES) and X-ray Magnetic Circular Dichroism (XMCD). The first two clearly determine and quantify the local symmetry, while the third is very sensitive to polarized magnetic moments variation. Thus, at each pressure point, simultaneous information on both the magnetic and the structural properties of the system are provided without any relative pressure incertitude, which is very important in the high pressure domain where the reproducibility of high-pressure hydrostatic conditions is difficult to obtain.

The study of electronic structure properties of materials at extreme conditions is a challenging problem both from theoretical and experimental viewpoints. On one hand, high pressure and temperature conditions push experimental data towards limits where conventional data analysis and interpretation approaches start to present their weaknesses. On the other hand, a complete theoretical understanding of the deep interplay between the electronic and atomic structure of systems in such conditions is still far from being reached. A tight connection between theoretical and experimental results is an asset in view of making significant advances in the field.

At this purpose a close collaboration was established with the ESRF (European Synchrotron Radiation Facility) Theory group (Y.O. Kvashnin, L.Genovese, P. Bruno). In a parallel theoretical PhD project entitled *Ab initio study of transition metals under high pressure* theoretical methods are currently developed to address electronic and structural properties of 3d transition metals under extreme conditions, in view of a better under-

standing of the mechanisms at the atomistic scale determining their behavior. In particular the experimental-theoretical collaboration has been devoted to the interpretation of the K-edge XMCD signal behavior under pressure, still controversial in the literature.

In this Thesis, combined XANES-XMCD and X-ray Diffraction (XRD) measurements are used to explore the high pressure limits for ferromagnetism stability and associated structural transitions in the case of cobalt, nickel and iron-cobalt (FeCo) alloys. The case of the FeCo alloy was investigated in order to study the role played by the chemical order in tuning the structural and magnetic properties under compression. The following main results were obtained.

In cobalt, our results provide the first experimental evidence of the pressure induced collapse of ferromagnetism occurring around 120 GPa where the fcc/hcp phase fraction is at least 40%. The XMCD signal decreases linearly and continuously up to total extinction whereas a progressive change in the arrangement of the first atomic shells from an hcp- to an fcc-like local structure is observed starting from around 80 GPa. Thus the magnetic response in Co seems to be quite independent from the structural modifications. A coherent scenario correlating magnetism, elastic-structural anomalies and theoretical results is furnished, highlighting major differences with the iron case.

In the case of nickel, the structural stability of the fcc phase over a wide pressure range offers a unique opportunity to experimentally investigate how magnetism is modified by the simple compression of interatomic distances. New high pressure K-edge XANES-XMCD measurements coupled to XRD measurements on pure Nickel are presented up to 200 GPa, a record pressure for absorption techniques. Our data show that fcc Ni is structurally stable and ferromagnetic up to 200 GPa contrary to the recent predictions of an abrupt transition to a paramagnetic state at 160 GPa. Moreover, novel DFT calculations describing the different behavior of orbital and spin moments in compressed Ni, point out that the pressure evolution of the Ni K-edge XMCD closely follows that of the p projected orbital moment rather than that of the total spin moment. The disappearance of magnetism in Ni is predicted to occur above 400 GPa.

The structural and magnetic phase diagram of $\text{Fe}_{1-x}\text{Co}_x$ under high pressure is attractive because of the very different behavior of the pure components: Fe loses its ferromagnetism across the bcc-hcp transition around 13 GPa and Co retains an hcp ferromagnetic phase up to around 100 GPa. Our systematic study in an unexplored pressure ($P \leq 70$ GPa) and composition range ($0.5 \leq x \leq 0.9$) provides a detailed description of the pressure-induced structural and magnetic transitions occurring in this range pointing out the close relationship between structure, magnetism and chemical order in this system. The comparison with DFT calculations shows that the chemical order plays a crucial role in determining the high pressure magnetic and structural properties. A first (x,P) magnetic and structural phase diagram for FeCo is drawn.

The results of the present work have been the subject of the following publications:

1. *Pressure-induced collapse of ferromagnetism in cobalt up to 120 GPa as seen via x-ray magnetic circular dichroism*, R. Torchio, A. Monza, F. Baudelet, S. Pascarelli, O. Mathon, E. Pugh, D. Antonangeli, J. Paul Itié, *Phys. Rev. B Rapid communications*, *Phys. Rev. B* **84**, 060403(R) (2011)
2. *XMCD measurements in Ni up to 200 GPa: resistant ferromagnetism.*, R. Torchio, Y.O Kvashnin, S. Pascarelli, O. Mathon, C. Marini, L. Genovese, P. Bruno, G. Garbarino, A. Dewaele, F. Occelli, P. Loubeyre, *Phys. Rev. Lett.* **107**, 237202 (2011)
3. *Structure and magnetism in compressed Iron-Cobalt alloys*, R.Torchio, S. Pascarelli, O. Mathon, C. Marini, S. Anzellini, P. Centomo, C. Meneghini, S. Mobilio, N.A. Morley and M.R.J. Gibbs, *High Pressure Research* **31** (2011) 148-152

completing papers are under preparation.

This Thesis is organized as follows:

Physical background and experimental techniques

- In Chapter 1 an historical overview of the scientific understanding of magnetism in the transition metals is given, with particular attention devoted to the Stoner band model in its merits and limitations. A *covalent magnetism* model, addressing the description of magnetism in *3d* metal alloys is presented and the close interrelationship between structure and magnetism in the transition metals is discussed. The effect of pressure on structure and magnetism is analyzed on the basis of the experimental and theoretical results present in the literature and the case of iron is reported as an example.
- Chapter 2 surveys some high-pressure apparatus. In particular, the diamond anvil cells and related equipment. The polarized XAS technique is described and the scientific and technical implications given by the high pressure setup are discussed. Special focus is dedicated to the interpretation of the K-edge X-ray Magnetic Circular Dichroism signal. Finally the principle of the energy dispersive spectrometer and high pressure XMCD setup of beamline ID24 is briefly described, pinpointing its suitability to this kind of experiments.

Experimental results and discussion

- In Chapter 3, 4 and 5 our new results on, respectively, cobalt, nickel and iron-cobalt alloys are presented. In each chapter the most relevant experimental and theoretical literature is overviewed and the experimental setup, used in each experiment, described. Then, the experimental results are discussed in comparison with previous studies and theoretical calculations.

Finally the overall conclusion of this work are presented.

Magnetism and structure in the *3d* metals

In this chapter an historical overview of the fundamental understanding of magnetism in the transition metals is given, with particular attention devoted to the Stoner band model. A covalent magnetism model, describing the magnetism of metallic alloys is presented. The close relationship between structure and magnetism in the 3d metal is discussed and the relevance of high pressure studies in addressing this complex interplay is underlined. The structural and magnetic modifications induced by compression in these metals are analyzed on the basis of the experimental and theoretical results present in the literature and the case of iron is reported as an example.

1.1 Itinerant ferromagnetism

In the history of magnetism and still today the magnetic properties of the transition metals Fe, Co and Ni and their alloys have constituted the core of the whole field of magnetism. The reason is that for these metals the electronic structure gives rise to sizable magnetic moments at room temperature. While the rare earths (or *4f* elements) have also been important in magnetism, they become attractive for potential applications only when alloyed with the transition metals, because this raises their Curie Temperature above room temperature. Therefore the scientific understanding and technological applications of the *3d* transition metals have dominated the field.

The difficulty and, at the same time, fascination with the transition metals is mainly in their duality between localized and delocalized, so called *itinerant*, behavior. This duality forms the core of the electronic many-body problem and is the essence of magnetism.

The atomic moments in Fe, Co and Ni are not multiples of the Bohr magneton but rather odd fraction of it, therefore cannot be explained by a successive orbital occupation as described by the Hund's rule. The puzzle about the broken Bohr magneton numbers in the ferromagnetic metals was solved through the development of band theory, which

was first applied to magnetic systems around 1935 by Mott [1], Slater [2, 3], and Stoner [4, 5]. The simplest band-like model of the ferromagnetic metals is often called the Stoner-model or Stoner-Wohlfarth-Slater-model and underlies our modern understanding of the magnetic structure of metals.

The assumption behind the SWS-model is that the bonding interaction between the 3d electrons causes a smearing of their energy into a band. In the presence of a Weiss Field (the exchange field \mathbf{H}^{ex}) the centers of gravity of the states characterized by opposite spins exhibit an exchange separation, the exchange splitting Δ , determining an unbalance in the spin-up and spin-down electron (holes) population. The magnetic moment \mathbf{m} is then given by the difference in the number of electrons in the majority and minority bands, as defined in Fig. 1.1 according to:

$$\mathbf{m} = \mu_B(N_e^{maj} - N_e^{min}) = \mu_B(N_h^{maj} - N_h^{min}) \quad (1.1)$$

In the band picture the number of majority and minority states is non integer and the magnetic moments are non integers multiples of the Bohr Magneton. This simple relation between electron and hole moments is exact only if the bands states are well defined in their energy spread about the Fermi level. In practice this is only approximately true for the 3d transition metals as will be explained in the next section.

The exchange field \mathbf{H}^{ex} generating the splitting of the electronic states is not a true magnetic field as it produces no electromagnetic induction and no Lorenz force. It finds its origins in the Heisenberg exchange interaction [6] which results in the formations of unpaired spin states. Heisenberg's original formulation describes localized electrons, while its first application to de-localized itinerant electrons is due to Stoner [4, 5]. The exchange field does not act on the orbital moment nor on the nuclear moment. Once the electron spin polarization and hence the spin moment is established by the exchange interaction, the coupling of the spin moment and the orbital moment is determined by the weaker spin-orbit interaction.

The Stoner theory establish a criterion for ferromagnetism stability at T=0:

$$I_S DOS(E_F) > 1 \quad (1.2)$$

where I_S is a measure of the exchange interaction and $DOS(E_F)$ is the density of states at the Fermi level. Thus the Stoner criterion is fulfilled either for a strong exchange interaction or for a large $DOS(E_F)$. In the transition metals the 3d bandwidth is small leading to a large $DOS(E_F)$ which satisfies 1.2. The quantity I_S , called Stoner parameter, is found to be a quasi-atomic property which depends very little on chemical or metallurgical effects (bonding, alloying, etc...).

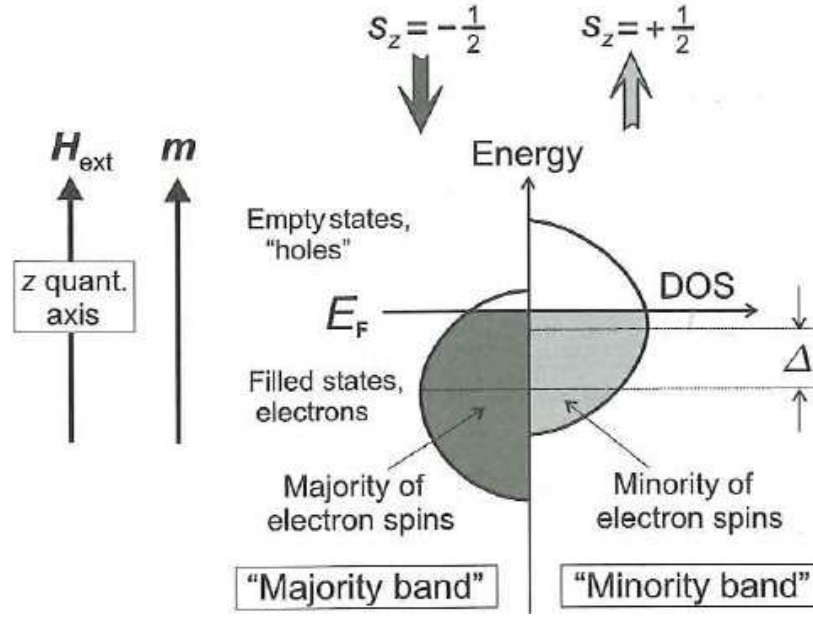


Figure 1.1: The Stoner model of ferromagnetic transition metals, illustrated for the $3d$ shell. Filled electron states below the Fermi energy E_F are shown shaded, hole states above E_F are shown unshaded. The spin states with the largest number of electrons are called "majority band" and the other "minority band". The labels "spin up" and "spin down" only have meaning with respect to a quantization direction, generally defined as that of the external field \mathbf{H}^{ex} . The density of states generated by the s-p electrons is not shown for clarity.

The Stoner model roughly applies to the metals at $T=0$ but fails at finite temperatures where unphysically high Curie temperatures are predicted and the calculated paramagnetic susceptibility does not describe the experimentally observed Curie Weiss law. The reason for this is that the magnetic moments are supposed to disappear through spin-flip excitations to the Stoner continuum, associated with the reversal of single electron spins, a process that costs too much energy. The understanding of finite temperature magnetism in the metals came only after, in the seventies, with the inclusion of thermally induced collective magnetic excitations, the so-called *spin waves* or *magnons* [7] (Fig. 1.2) thanks to the pioneering work of Moriya, Hubbard, Hasegawa, Korenman, Gyorffy, Edwards, and others [8–15]. Basically, the *spin wave model* distributes the spin-flip of a single electron (Stoner excitation) over many lattice sites [16]. After the broad consensus reached on the fact that orientational fluctuations of the local magnetization represent the essential ingredients to a thermodynamic theory, several different approaches were developed (see [17] for a review). Despite its limitations, the Stoner model however posed the basis for the modern spin polarized band theory which can nowadays describe most aspects of magnetism in the transition metals.

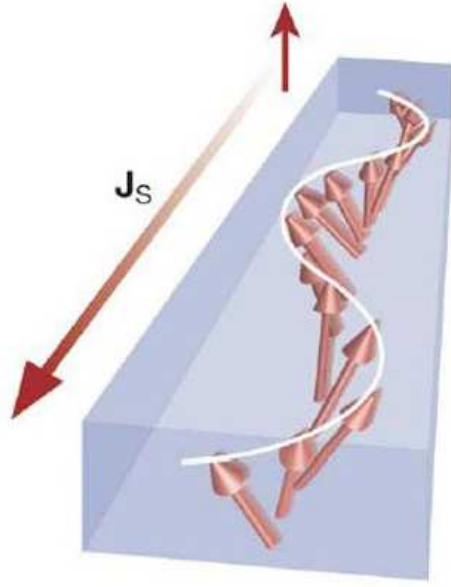


Figure 1.2: A schematic illustration of a spin-wave spin current: spin angular momentum carried by collective magnetic moment precession.

1.1.1 Basic bands theoretical results for the transition metals

The calculated DOS for Fe, Co, Ni and non magnetic Cu are shown in Fig. 1.3 [18]. Their shape is quite similar but Cu, as expected, shows no exchange splitting. The exchange splitting Δ , defined as the relative shift of the largest peak in the DOS, is of the order of 1 eV.

The structures in the density of states are due to the overlap interactions of the d -states on neighboring atoms, with the atoms located on lattice points of well defined symmetry. Due to the larger number of nearest neighbors, the density of states of the closed packed systems (Co hcp and Ni fcc) is much more compact and does not show the pronounced minima and maxima typical of the bcc DOS. The most important difference in the four DOS plotted in Fig. 1.3 is the position of the Fermi level, separating the occupied states from the unoccupied states, accounting for an increasing number of d electrons in going from Fe to Cu. Figure 1.3 also shows the density of states generated by the s - p electrons, which is much smaller and flatter, and is clearly visible only at energies above the d bands, while it underlies the $3d$ DOS at lower energies. The s - p bandwidth is around 10 eV while the d bandwidth is about 3 eV.

In Co and Ni there are, to first order, no majority spin d holes. The notion that magnetism in Ni and Co is mainly due to the electrons in only one spin band has led to the definition of "strong" ferromagnets. In contrast, Fe is called a "weak" ferromagnet because there are sizable d bands contribution in both spin channels. The band splitting leaves the shape of the two subbands almost unchanged. This behavior, called *rigid band behavior*, occurs in pure metals and alloys of metals (magnetic) and metalloids (non-

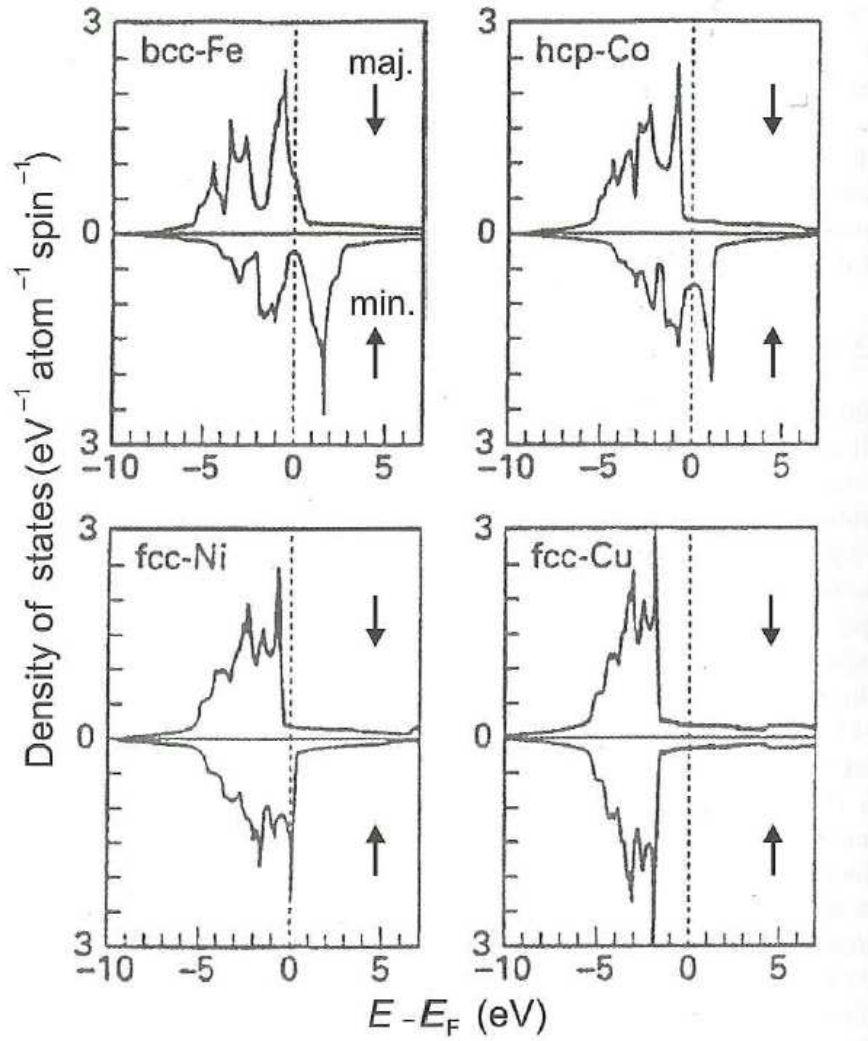


Figure 1.3: Density of states of Fe, Co, Ni and Cu for the majority and minority spins from [19]. The Fermi energy is set to zero.

magnetic). In alloys which consist of more than one magnetic constituent (like FeCo, for instance) the interaction between the different atoms leads to changes in the electronic structure which go beyond this simple picture.

Integrated properties of the d band are shown in Fig. 1.4. Calculations are from Wu and co-workers [16, 19] within the full-potential-linearized augmented plane wave method. In the top panels integrated number of d states (left) and summed $s+p+d$ states (right) are shown. In the bottom panels are the corresponding integrated spin moments. This results provide important information: first, the spin magnetic moments in the transition metals are almost entirely due to the d electrons, as very similar values are obtained with or without $s-p$ electrons. Close inspection actually reveals that the $s-p$ contribution has opposite sign with respect to the d contribution and is of the order of $-0.04\mu_B \leq m^{sp} \leq -0.07\mu_B$ for Fe and Co and $-0.02\mu_B \leq m^{sp} \leq -0.04\mu_B$ for Ni. Second, the hole spin moments

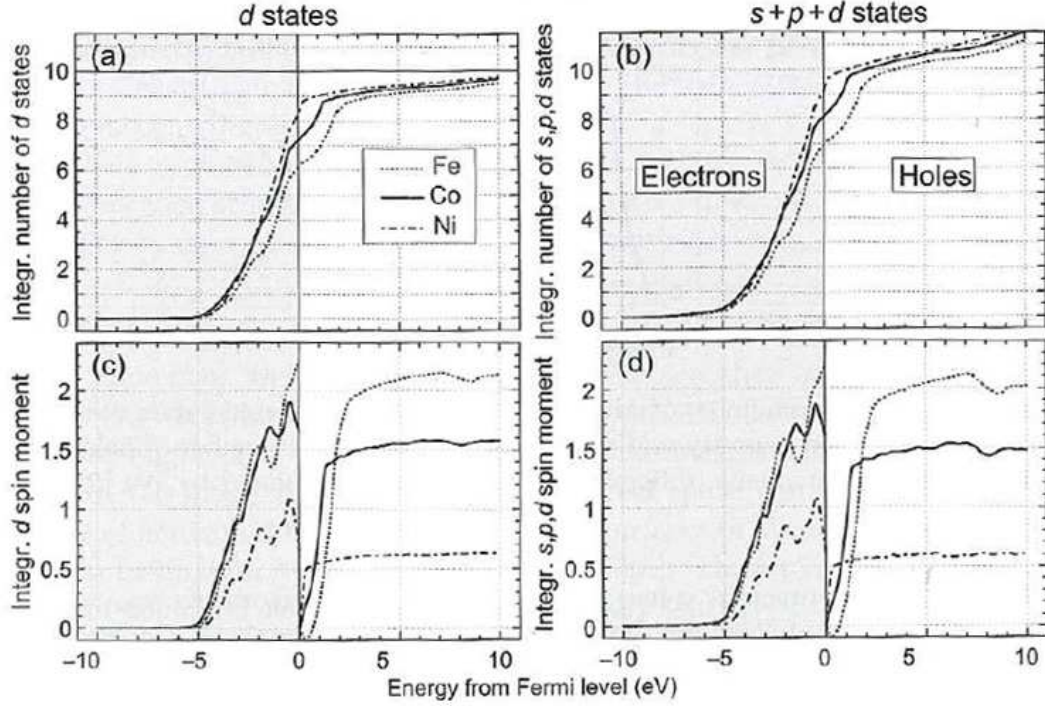


Figure 1.4: a) integrated number of d states (electrons and holes) and b), integrated number of $s+p+d$ states in Fe, Co, and Ni. c) and d) integrated electron and hole moments for d and $s+p+d$ states. Data are from [19] as represented in [16]. The integration is $-10 \leq E - E_F \leq 0$ eV for electrons and $0 \leq E - E_F \leq 10$ eV for holes.

are slightly reduced relative to the electron moments, as at 10 eV above the Fermi energy the number of unfilled d states (holes) has still not converged to the expected value of 10 and 5% states are missing. This was firstly pointed out by Wu and co-workers [19, 20] and arises from hybridization of the d states with the more delocalized $s-p$ states; thus some of these hybridized d states lie at higher energies above E_F .

The orbital moment $m_0 = -\mu_B \langle l_z \rangle$ arises from an imbalance in the occupation of $+m_l$ and $-m_l$ states. In the 3d metals the orbital moment is largely quenched by the

	Fe bcc		Co hcp		Ni fcc	
	$m_{spin}(\mu_B)$	$m_{orb}(\mu_B)$	$m_{spin}(\mu_B)$	$m_{orb}(\mu_B)$	$m_{spin}(\mu_B)$	$m_{orb}(\mu_B)$
Theory	2.21	0.06	1.57	0.14	0.61	0.07
exp	2.13	0.08	1.52	0.14	0.57	0.05

Table 1.1: Spin and orbital moments for Fe, Co, Ni. Calculated values are from [21], experimental values are from [26].

crystal field and only arises from the spin-orbit interaction; its contribution to the total magnetization accounts for a 5-10%.

Nowadays theoretical approaches based on the density functional theory using different basis function and approximations for the exchange correlation potential furnish quite satisfactory results for the *3d* metals spin moments. The typical variation encountered between different methods as well as between theoretical and experimental values is around 4-9 % [16]. Poorer is the agreement between calculated and experimental values of orbital moments, however this was much improved by the work of Eriksson and co-workers where orbital polarization and spin-orbit interaction were included within the Linear Muffin Tin Orbital (LMTO) approach.

In Table 1.1.1 we report calculated values of the spin and orbital magnetic moments by Eriksson et al. [21]. The agreement with experimental results is quite good.

1.2 The magnetism of alloys: covalent magnetism

Itinerant magnetism in a variety of transition-metal systems such as elemental anti-ferromagnets, impurity systems (transition metals in transition metals) and certain transition-metal compounds cannot be described by the Stoner model rigid-band theory. Magnetism in these cases is shown to arise from spin-dependent interactions between the *d* states of neighboring transition metal atoms [22].

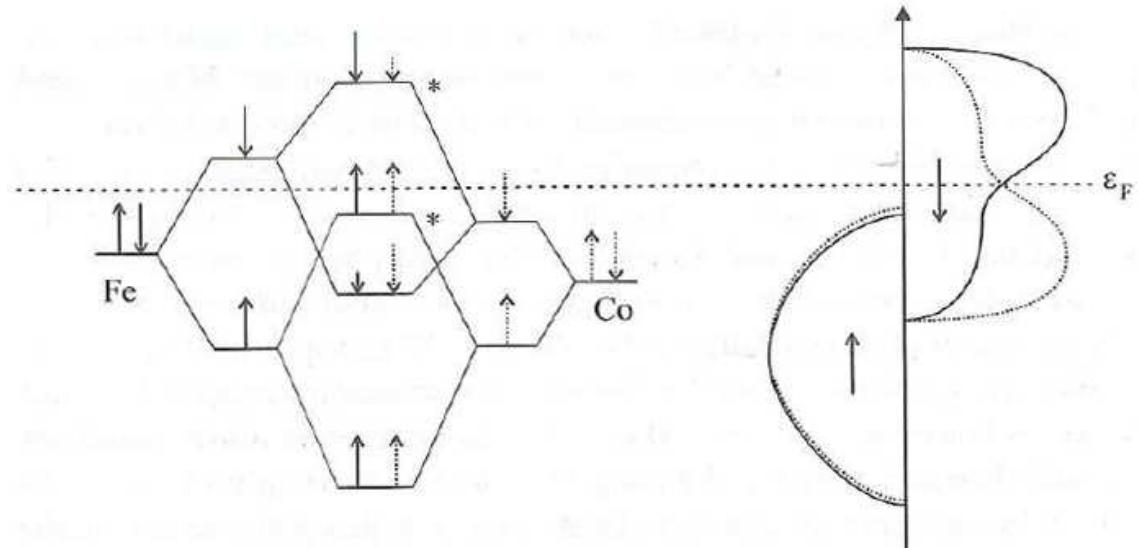


Figure 1.5: MO diagram of the covalent interaction in FeCo and its translation into the density of states, after [25].

As an example the Fe-Co system is chosen. Due to their vicinity in the periodic table these two metals have similar electronic structure and electronegativity, therefore any substantial charge transfer between them can be ruled out. Pure Fe and pure Co

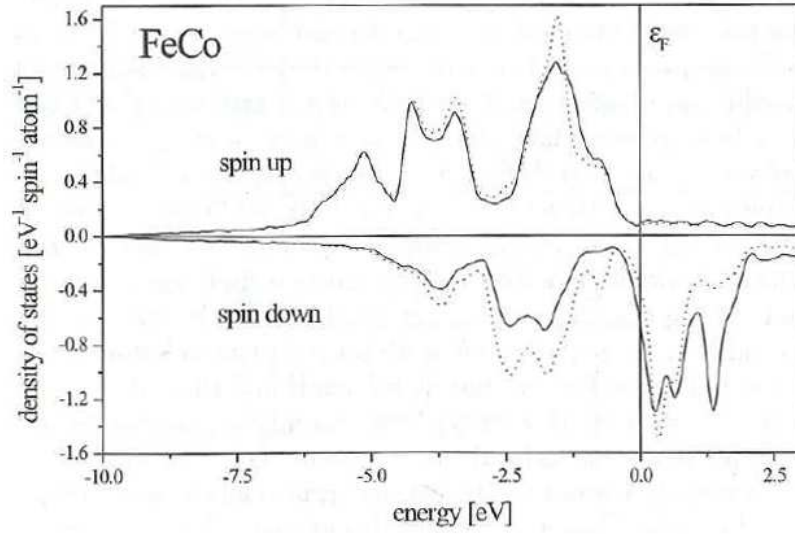


Figure 1.6: Density of states of the FeCo alloy (at 50% of Co), Fe-DOS full line and Co-DOS dotted line; after [25].

crystallize in bcc and hcp symmetry respectively. $\text{Fe}_{1-x}\text{Co}_x$ crystallizes in a body centered structure up to $x \leq 0.75$. On alloying they will form a common band as long as the energies of the respective Fe and Co states are comparable. If a rigid band behavior were assumed one would simply fill the resulting band with the available number of electrons, allowing a charge transfer of half electron from cobalt to iron. This charge transfer, as mentioned above, is unphysical not only because of the comparable electronegativities but also for the metallic character of the bond. Indeed band structure calculations [23, 24] show that the common band picture is valid only for the fully occupied spin-up band - where the same number of electrons for both Co and Fe, namely 5, are present - whereas this is not the case for the spin-down bands.

Fig. 1.5 shows how the Fe-Co magnetism can be understood from a simple molecular orbital (MO) scheme. One starts from the non spin-polarized states of Fe and Co. Due to the additional electron, the Co states will be lower in energy than the Fe ones. If one now allows for a band splitting, Fe will show a larger splitting than Co. Since only states with the same spin energy can interact, Fe and Co spin up, which are about at the same energy will form a common band. For the spin-down states, a higher energy difference occurs. When these states form a molecular (hybrid) orbital, the occupation of the atomic electrons will be inversely proportional to the energy difference between the atomic level and the MO-level. This means that for the spin down bonding MO more Co than Fe electrons will be transferred and viceversa for the antibonding state (this is sketched in Fig 1.5 using a variable length of the spins arrows). If this picture is now translated into a density of states (right panel of Fig. 1.5), it leads to an unperturbed DOS for spin-up (the Co DOS in Fig. 1.5 right panel is slightly shifted to make it visible) and a distortion for the spin down DOS according to the MO mechanism.

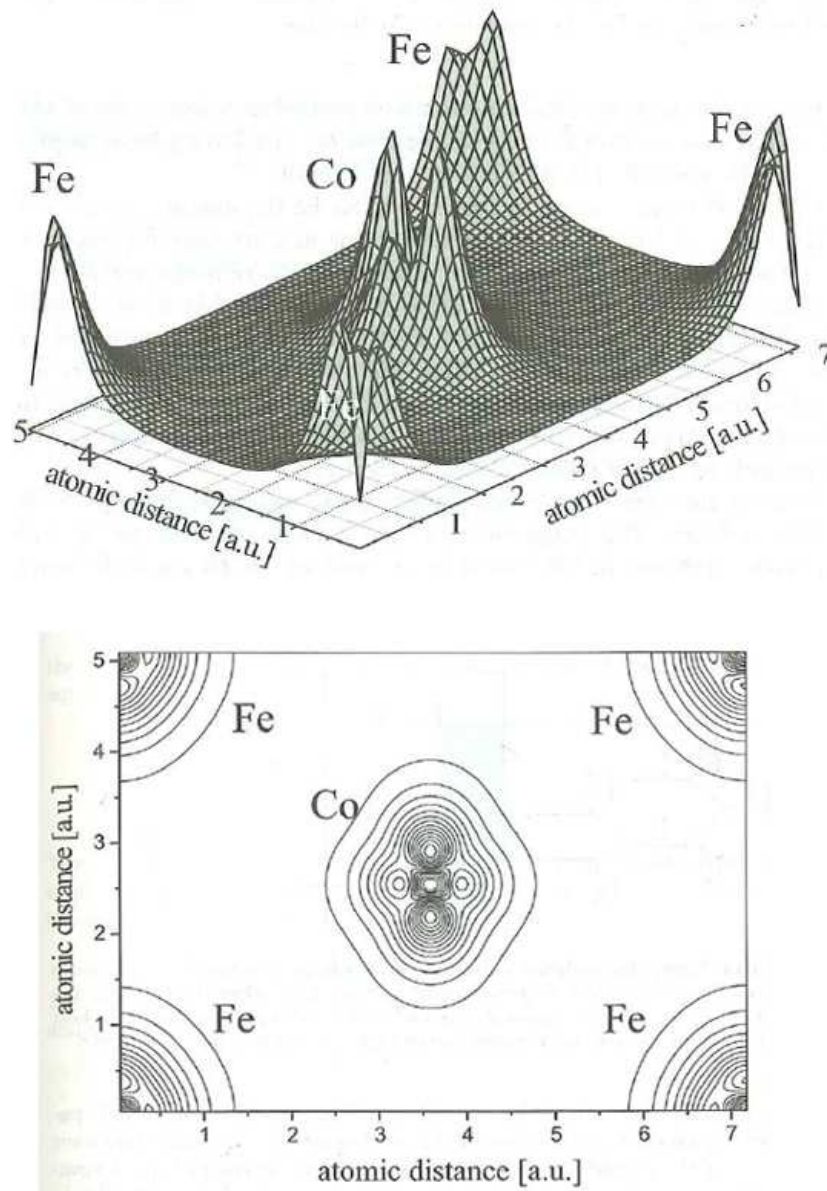


Figure 1.7: Magnetization density (top) and magnetization density contours plot (bottom) in a [011] plane for the ordered phase of FeCo, after [25].

Fig. 1.6 shows an actual DOS from a calculation of the electronic band structure for $\text{Fe}_{1-x}\text{Co}_x$ $x=0.5$. The mechanism sketched in Fig. 1.5 can be identified with a common band for the spin up DOS and the redistribution of spectral weight in the spin down band. Since this redistribution enhances the number of Co states below the Fermi level, Co can accommodate its additional electron without the need of a charge transfer.

It can be also interesting to look at how the magnetization density - i.e. the difference between the spin-up and the spin-down electron density - is distributed within a magnetic solid. Such an analysis can be drawn from neutron diffraction experiments or, nowadays

more easily, from calculations of the electronic structure. Figure 1.7 shows the results of a full potential LMTO (Linear Muffin Tin Orbital) calculation for the ordered phase of FeCo. It can immediately be seen that the magnetization density is far from being uniformly distributed over the whole crystal as one would expect for an itinerant electron magnet. However this is not really surprising since the carriers of the magnetic moments are the d -electrons which are certainly not delocalized themselves. This result points out that the assumption of free electrons does not really stand for the transition metals. Since the magnetization density is produced by the narrow $3d$ -bands it appears to be fairly localized around the atomic positions. Moreover, from the contour plot (Fig. 1.7 bottom panel), it can be noticed how aspherical the spin density is and particularly around Co. This feature is again a direct consequence of the covalent interactions present in the FeCo alloy.

1.3 Structure and magnetism in the 3d metals

The crystal structures for most metallic elements have been known for a long time and it was early recognized that they show a pattern which could be related to the chemical periodicity of the elements. The $4d$, $5d$, and the nonmagnetic $3d$ transition elements all follow the same structural sequence $hcp \rightarrow bcc \rightarrow hcp \rightarrow fcc$ through the series as a function of atomic number.

This behavior can be traced back to the electronic structure and the interaction of the s and d bands in these elements [27]. The major role is played by the progressive filling of the d band and by the fact that the characteristic shapes of the bcc, fcc and hcp density of states are essentially element independent [28, 29]. Fig. 1.8 shows an excerpt from the periodic table concentrating on the s - d transition metals series.

The magnetic elements Mn, Fe and Co however, deviate from this general trend. Mn which would be expected to be hcp, forms a highly complicated structure (the α -Mn) with 58 atoms per unit cell. Also its magnetic structure is extremely complicated exhibiting anti-ferromagnetism together with non-collinear spin ordering. The most stable phases for Fe and Co are the bcc and hcp structures respectively although they would actually fall into the hcp (Fe) and fcc (Co) group. The origin of this deviation lies in the $3d$ metals magnetic order. The number of valence electrons is the sum of the s and d electrons. In the magnetic elements magnetism causes a band splitting and thus a different occupation of the spin-up (n^\uparrow) and spin-down (n^\downarrow) bands while n^\uparrow and n^\downarrow are the same for non magnetic elements. If one assumes, for simplicity, that the spin-up d band is full with 5 electrons (like in strong ferromagnets) the remaining electrons occupying the spin-down band would be 2, 3 and 4 for Mn, Fe and Co respectively (see the gray shaded box in Fig. 1.8). From the chemical bond theory it is known that filled electron shells do not contribute to the bonding. This means that for Mn, Fe and Co the full (or almost full) spin-up band can be neglected and the electronic and structural properties are governed by the partially

n_{4s+3d}^{\uparrow}	1.5	2	2.5	3	5	5	5	5	5.5
n_{4s+3d}^{\downarrow}	1.5	2	2.5	3	2	3	4	5	5.5
3d	Sc ⊗	Ti ⊗	V □	Cr □	Mn ⊕	Fe □	Co ⊗	Ni ⊗	Cu ⊗
4d	Y ⊗	Zr ⊗	Nb □	Mo □	Tc ⊗	Ru ⊗	Rh ⊗	Pd ⊗	Ag ⊗
5d	La ⊗	Hf ⊗	Ta □	W □	Re ⊗	Os ⊗	Ir ⊗	Pt ⊗	Au ⊗
$n^{\uparrow}+n^{\downarrow}$	3	4	5	6	7	8	9	10	11

⊕ α -Mn □ bcc ⊗ fcc ⊗ hcp

Figure 1.8: The s - d transition metals series in the periodic table follow the hcp \rightarrow bcc \rightarrow hcp \rightarrow fcc structural sequence as a function of the number of valence electrons, with the exception of the magnetic Mn, Fe and Co. This representation is from [25].

filled spin-down band. Therefore Mn, Fe and Co behave as if they had 2,3 and 4 valence electrons responsible for the chemical bonding and thus for the crystal structure. Fe thus falls in the Cr, Mo, W group and adopts the bcc structure; Co falls in the Ru, Os and becomes hcp (see Fig. 1.9) [30]. Mn, as mentioned above, is rather a case in itself. The fact that for the magnetic elements the spin-up electrons do not contribute to the bonding also leads to a significant reduction of the bulk modulus [30].

This simple model, proposed by Söderlind and co-workers [30] as a development of the previous work by Skriver [28] on non magnetic metals, presumes that all the $3d$ metals structures show saturated magnetism (equal exchange interaction) which is not strictly true for Fe which is a weak (unsaturated) ferromagnet. This model is therefore inadequate to describe certain systems in which the weak magnetism of Fe plays a crucial role, like in FeCo (see the *Iron-Cobalt alloys* chapter). It however furnishes an effective way to rationalize the real behavior of ferromagnetic metals pointing out the strong influence of magnetism in stabilizing the crystal structures.

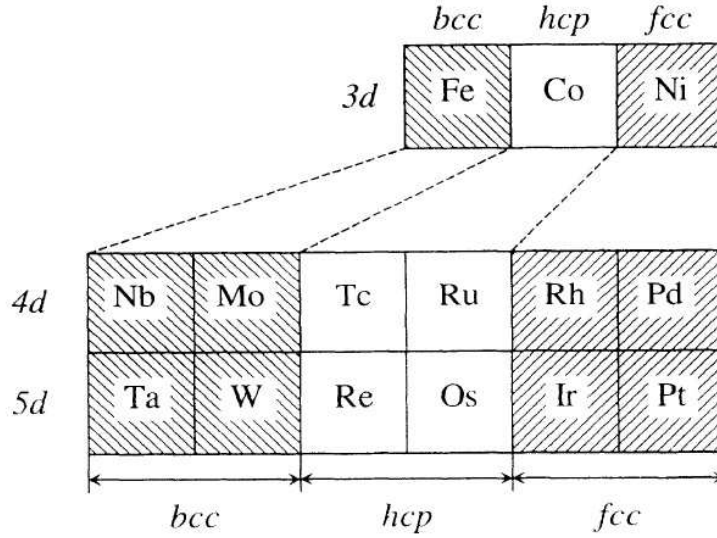


Figure 1.9: Schematical picture of the $s+d$ metals in the periodic table from [30]. The connection, as regards the valence number of electrons and crystal structure, between Fe, Co, Ni on one hand and the $4d$ and $5d$ elements on the other hand is shown.

1.4 High pressure studies

It is through pressure, which is a special case of generalized stress, that one can change the volume of a system or the average particle density. The changes may be brought about in a quasi-static way, typically nowadays by the use of Diamonds Anvil Cells (DACs), or dynamically, through the use of shock methods [31, 32]. In either case, the atoms in condensed forms of matter are driven closer together. As observed by Percy Williams Bridgman (Nobel Prize in Physics in 1946) of Harvard University in 1926, this compression offers a route to "breaking down" the electronic structure of the atoms themselves and to the possibility of creating entirely different bulk properties.

Pressure induces myriad changes in materials. First, compression typically causes a tendency towards closer packing of atoms, ions and molecules. Although this is often assumed to mean a corresponding tendency towards simpler structures, sometimes quite the opposite is true. Indeed, pressure may induce order, but it also can bring out disorder [33]. Generally, a compression is followed by an increase of local coordination number; this increase in turn is intimately linked to variations in the electron hybridization. Such changes in turn can be associated to major modifications in electronic and magnetic states, including the formation of conductors or superconductors from materials originally possessing substantial bandgaps [34, 35]. Finally, pressure can affect the chemical behavior: chemical reactions can be induced that do not occur under more familiar conditions [36]. Although many of these effects of pressure on condensed matter have been known for years, it is only recently that the full potential of the pressure variable in the condensed matter sciences has begun to be realized. This change is mainly due to the striking advances that

have occurred in parallel in both experimental high pressure techniques and in theoretical methods respectively.

1.4.1 Pressure effects on magnetism and structure in the *3d* metals

The compression of interatomic distances in the *3d* metals leads to variations in the elementary magnetic moment and in the Curie temperature [37].

The former effect is generally interpreted, in the framework of the Stoner model, as a consequence of the decreased DOS at the Fermi level which follows from the pressure-induced band broadening associated to the interatomic distance squeezing. In fact, the band-width (W) increases rapidly as the interatomic distances r are reduced ($W \approx r^{-5}$ according to the general result of Heine [39, 41]), whereas the Stoner parameter I_S is, to first approximation, independent of the volume ¹[4, 18, 38, 46]. Hence, the pressure-induced decay of the number of states at E_F weakens the ferromagnetism condition. This simple picture gives an intuitive understanding of the physics involved, however, in a more accurate analysis, the Stoner parameter should be allowed to vary with the volume [40, 46].

As an example, high pressure (zero temperature) DOS calculations for pure Ni are shown from Xie and co-workers up to 80 GPa [44] in Fig. 1.10. As the pressure is increased, both spin-up and spin-down DOS spread downwards and the height of the DOS at the Fermi level (in the spin-down bands) decreases while the splitting between spin-up spin-down bands remains substantially unchanged (as can be seen by looking at the highest DOS peak position). Meanwhile the difference in the number of spin-up and spin-down electrons - i.e the Ni elementary spin magnetic moment- decreases reaching 87% of its initial value at 100 GPa [43–45].

In the *3d* metals the loss of ferromagnetism is generally concomitant to a structural transition. Several zero temperature high pressure calculations have been carried out, and there is a general agreement on the expected pressure induced magnetic/structural transitions. Fe is predicted to undergo the bcc ferromagnetic to hpc non-magnetic phase around 10-15 GPa [43, 45–50]; ferromagnetic Co would transform into non magnetic fcc phase around 100 GPa [43, 50–52], while Ni is expected to remain in a stable fcc ferromagnetic structure up to the 10^2 GPa range [43–45]. In the *3d* metals compression thus favors closed packed arrangements and a higher resistance of magnetism can be associated to a stronger ferromagnetism, following from the progressive filling of the minority *d*-band when going from Fe to Ni. However, a large debate is still open on whether structural instabilities are driven by magnetic instabilities or viceversa.

The latter effect, the Curie temperature shift with pressure, is related to the variation in the exchange interactions [37]. Experimental observations of the Curie temperature shift with pressure only reach 2, 15 and 25 GPa for Fe [37], Ni [53] and Co [54] respectively. In this low pressure range, T_c is seen to remain constant (Fe) or to increase (Co and Ni).

¹In bcc iron, for a compression of 0.9 of the Wigner-seitz radius, the Stoner parameter I_S is found to increase by a 3% whereas $I_S \text{DOS}(E_F)$ decreases by 33% [40].

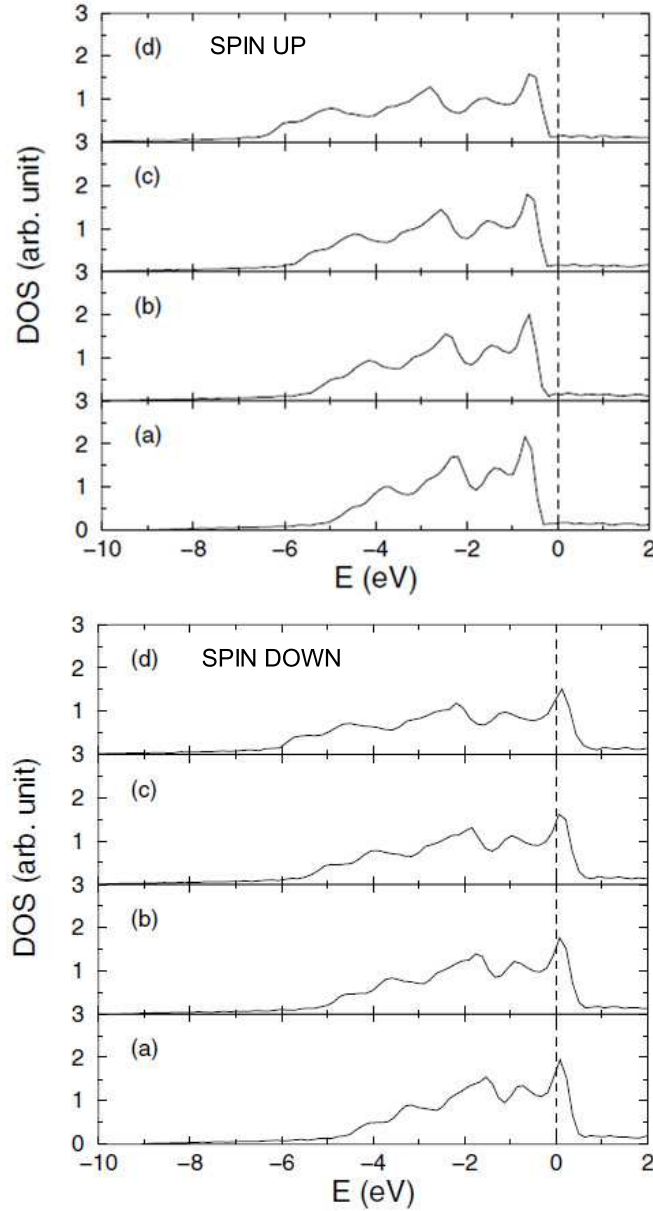


Figure 1.10: Pressure dependence of the spin-up (top panel) and spin-down (bottom panel) density of states in Ni. a) $P=0$ GPa, b) $P=20$ GPa, c) $P=40$ GPa, d) $P=80$ GPa.

The theoretical description of the T_c dependence on volume is nowadays still challenging. Despite the necessity to include collective fluctuation of the magnetization direction has been understood, the results remain controversial. In Fe and Co both a positive and a negative initial slope are reported [55–58]. In Ni, a general agreement is reached for the initial T_c increase with pressure but not on the definitive drop of T_c caused by the loss of correlation at very high pressures [35], which is predicted above 300 GPa by Tissen [59] and around 160 GPa by Shang and co-workers [60].

From the experimental point of view, thanks to the lower pressure range, the iron

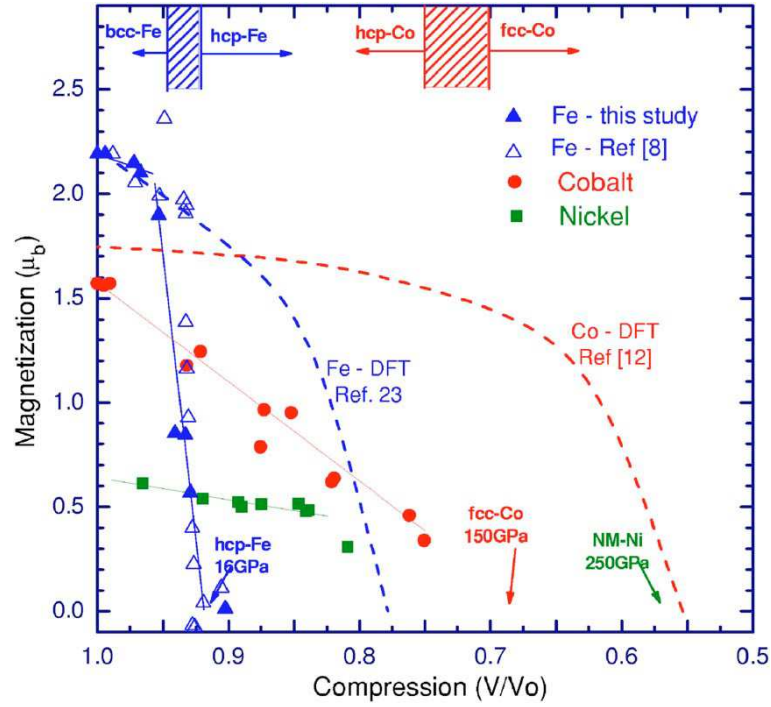


Figure 1.11: XMCD signals scaled to the standard moment for Fe (blue triangles), Co (red circles) and Ni (green squares) from [42]. The solid lines represent linear fits of the data and dotted lines represent DFT calculations from [46, 99] for Fe and Co respectively.

case has been widely investigated and the bcc-FM to hcp-NM phase transition, occurring around 13 GPa, rather settled (see next section). The high pressure hcp-fcc structural transition in Co has been observed by diffraction to occur in the 100-150 GPa range [61] whereas Ni is found to retain a stable fcc structure up to 150 GPa [62]. In 2007, two systematic high pressure studies on magnetism and structure in the *3d* metals by means of polarized absorption were carried out [42, 63]. The X-ray Magnetic circular Dichroism (XMCD) signal, assumed to be proportional to the magnetic moment, was observed to decrease linearly in Co and Ni, with a higher and a smaller rate respectively. These works thus confirmed that a higher resistance to compression relates to a stronger ferromagnetism. A non zero signal was recorded up to 100 GPa in cobalt and 70 GPa in nickel. Basing on these results, the limits for ferromagnetism were roughly estimated to be around 150 GPa for Co - i.e. at the end of the structural hcp-fcc transition - and above 250 GPa in Ni [42] (Fig. 1.11). In Co the HP limits for ferromagnetism have been established only recently with the results presented in this Thesis [64]. At the same time, Ishimatsu and co-workers [65] performed a similar investigation but did not observe the total extinction of the signal. This finding was interpreted as the occurrence of a paramagnetic phase in Co above 150 GPa. For Ni, the present results extend the pressure range of magnetic and structural observation up to 200 GPa.

A more detailed overview of the existing literature is presented in the next section

for iron and in the dedicated chapters for cobalt and nickel in comparison with our new results.

The advantage of high pressure studies with respect to high temperature ones, is that high pressure can bring to real non-magnetic states (characterized by zero local moment), to be distinguished from the T-induced paramagnetic states where the magnetic order has been disrupted but an elementary moment still exists [25]. However, as mentioned above, also the Curie temperature is expected to vary with pressure and the disentanglement of the two effects - i.e. suppression of elementary moment and thermal disorder - may not be trivial (see the *Experimental Methods Section*).

1.5 The iron case

The iron phase diagram has attracted considerable interest for a long time. At the beginning, the motivation was in its central role in the understanding of the behavior of alloys and steel and their production [66]. Later its geophysical importance was emphasized, because of its predominant abundance in the Earth's core [67, 68] which makes it crucial for the understanding of inaccessible regions of the planet.

The high pressure/high temperature phase diagram of iron is still not well established, with many conflicting experimental results. At room temperature and atmospheric pressure, pure iron is stable in the bcc (α) phase. This phase is ferromagnetic, apart from a small region above 1000 K, where the Curie transformation takes place [37] before the transition to the paramagnetic fcc (γ) phase. At higher temperatures (1700 K) and ambient pressure Fe transforms into a second bcc phase δ -Fe before melting ($T > 1800$ K). The α , γ and δ phases are believed to be stabilized by magnetism [69, 70]. Under the application of an external pressure at ambient T, iron undergoes a transition at 13 GPa from the bcc α -phase to the hcp ϵ -phase structure [71], with the loss of its ferromagnetic long range order [72]. In the pure hcp ϵ -phase, superconductivity appears close to the transition between 15 and 30 GPa, below 2K [73, 74]. A double-hcp structure is reported by laser-heated DAC experiments [75, 76] in a region around 40 GPa and 1500 K and two other high temperature phases have been suggested to be stable at high pressure: an α' -Fe phase above 200 GPa and 4000 K with a proposed bcc structure [77] and a β -Fe phase above 40 GPa and between 1500-3000 K with an unknown structure [78, 79]. Subsequent theoretical calculations [67, 80] have shown, however, that the bcc structure is mechanically instable at high pressures and unlikely to be the structure of α' -Fe. The high pressure melting of iron is also not well understood, with a resulting uncertainty of at least 3000 K in the melting temperature at the inner core - outer core (IC-OC) boundary (see Fig. 1.12 right panel).

Let's now focus on the RT pressure-induced transition from the ferromagnetic bcc phase to the non-magnetic hcp phase around 13 GPa, which is of major interest for comparison with the other systems analyzed in this Thesis. The evolution with pressure of

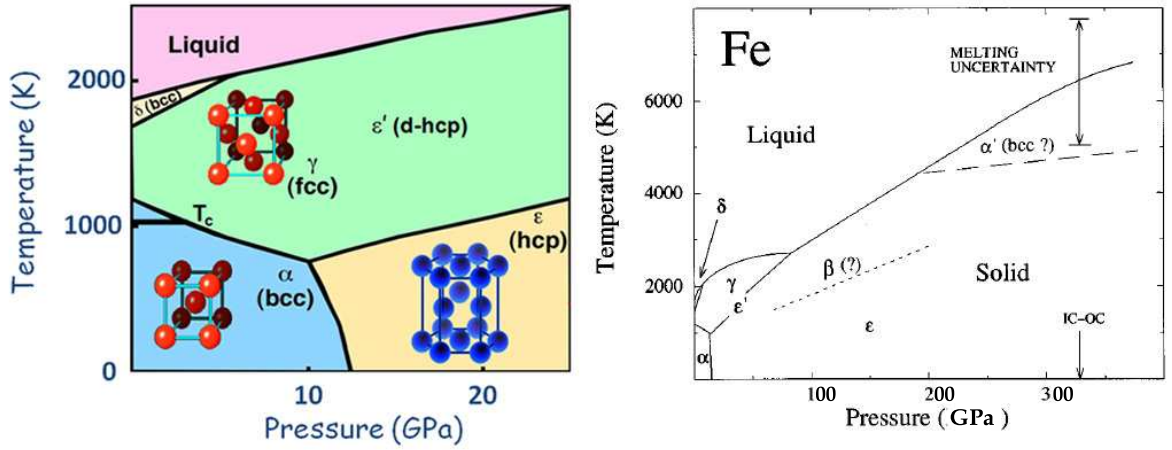


Figure 1.12: Right: (P,T) phase diagram for iron up to the IC-OC boundary and zoom of the diagram in the lower pressure and temperature range (left).

the magnetic and structural state across this transition is still a subject of active theoretical and experimental research. Moreover, a large debate is still open on which, between the structural and magnetic degrees of freedom, plays a driving role.

Considerable *ab initio* theoretical studies of this transition have been carried out [46, 67, 70, 74, 81–84]. The first order nature of the structural and magnetic transitions is well established as well as the non ferromagnetic state of the hcp phase. Some theoretical works support that the phase transition is primarily due to the effect of pressure on the magnetism [46, 81] rather than induced by phonon softening [70]. Recent calculations, based on a multiscale model containing a quantum-mechanics-based multi-well energy function, propose an initiation of the bcc-hcp phase transition due to shear [85]. During the transition a low-spin state is also suggested. At higher densities and below 70 K, an incommensurate spin-density-wave-ordered state is predicted [86] for a small pressure range starting with the onset of the hcp phase, as for superconductivity.

Structural investigations have been reported using x-ray diffraction [62, 63, 87] and extended x-ray absorption fine structure (EXAFS) [88]. The iron bcc-hcp phase transition is described as a martensitic transformation² with a slow variation of the relative bcc and hcp phases abundance. Distorted bcc and hcp phases with anomalously large lattice constant (bcc) and c/a ratio (hcp) when the relative amounts become small are reported and attributed to interfacial strain between the bcc and the hcp phases. A transition model based on lattice shearing movements is proposed with a possible intermediate fcc structure [88]. Magnetic measurements based on Mossbauer techniques [72, 89–91] and on inelastic x-ray scattering [92] showed that the magnetic moment of iron decreases over

²A martensitic transformation is a subclass of the diffusionless transformation. These phase transitions occur without long-range diffusion of atoms but rather by some form of cooperative, homogeneous movement of many atoms that results in a change in crystal structure. These movements are small, usually less than the interatomic distances, and the atoms maintain their relative relationships.

the same pressure range as the bcc to hcp transition, i.e., 8 GPa. Nevertheless, the lack of reproducibility of high-pressure conditions did not allow a precise correlation between the structural and the magnetic transition when measured separately.

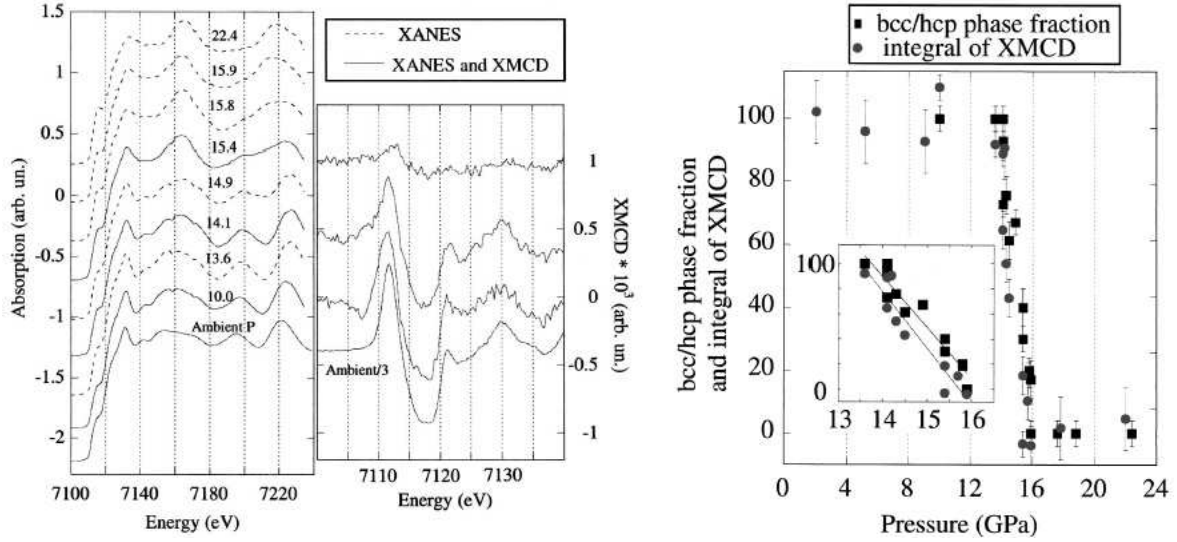


Figure 1.13: Left: Fe K-edge XAS (left panel) and some examples of XMCD (right panel) as a function of pressure between Continuous lines correspond to examples of data measured simultaneously; from [93]. Right: Percentage of bcc phase and integral of the XMCD signal as a function of pressure from [93].

In 2005 Mathon et al. [93–95] reported simultaneous X-ray absorption spectroscopy (XAS) and X-ray magnetic circular dichroism (XMCD) studies of the Fe bcc-hcp transition. Polarized X-ray absorption spectroscopy contains intrinsic structural, electronic, and magnetic probes through X-ray absorption near edge structure (XANES) and X-ray magnetic circular dichroism (XMCD). Thus, for each pressure point, simultaneous information on both the magnetic and the structural properties of the system can be provided without any relative pressure incertitude, which is very important in the high pressure domain where the reproducibility of high-pressure hydrostatic conditions is difficult to obtain (see the *Experimental Methods Chapter* for a more detailed description of the technique). The magnetic transition was seen to slightly anticipate the structural one supporting a magnetism driven process in agreement with phonon dispersion measurements [96].

This work demonstrated the efficiency of polarized XAS techniques to address pressure-induced structural(electronic)/magnetic transitions, laying the foundations for subsequent important systematic studies on the 3d metals by Iota and co-workers [42] and Ishimatsu and co-workers [63]. The results presented in this Thesis are a further extension and development of those studies.

Experimental methods

This chapter briefly surveys the apparatus for high-pressure studies used in this work. It describes the principle of the diamond anvil cell and the most common pressure measurements methods. In the second part, the polarized absorption technique is presented with special attention devoted to X-ray Magnetic Circular Dichroism from interpretational and experimental point of view. Finally, a description of the setup used at beamline ID24 (ESRF) is given.

2.1 High-pressure experimental methods

Numerous different types of devices are nowadays available to produce high pressure conditions (see [103] for an exhaustive review). They can mainly be divided into two broad families: those based on a piston-cylinder vessel and those in which the sample is compressed between anvils. The Diamond Anvil Cell (DAC) is the most largely diffused device for generating high static pressures. Compared to piston cylinder devices, the DAC is three or four orders of magnitude less massive (it can fit into the palm of the hand), and can generate much higher static pressures, up to the 10^2 range [104]. Moreover, the diamond transparency to the electromagnetic radiation over a wide frequency range makes this instrument a simple but powerful tool for the spectroscopic investigation of matter under extreme conditions.

2.1.1 Amagnetic diamond anvil cells

The first DAC was designed and constructed at the National Bureau of Standards [105]. The great number of results in the field of HP research is strictly related to the development of the DAC technique; see ref. [106] for a review of early developments. The DAC is very simple in principle. It consists of two gem-quality single crystal diamonds with flat surfaces to serve as anvil faces. The diamonds are mounted so that a sample can be squeezed between the anvil faces. The smaller the area A of the anvil faces, the higher the pressure P reached by the DAC for an equivalent value of applied force F , according

to the well known relationship $P = F/A$. To apply pressure to the sample, the anvil faces must have a high degree of parallelism and concentricity. One of the diamond anvils is usually mounted on the end of a sliding piston, while the other is stationary. A cylinder guides the piston so that the anvil faces meet very precisely. The piston is pushed by a mechanical device such as a screw or a small hydraulic ram, thus driving the two anvils together. A rocker or a tilting plate directly under the diamond anvils allows orientation of the diamonds to be adjusted so that the faces are concentric and parallel. Figure 2.1 shows the principle of DACs.

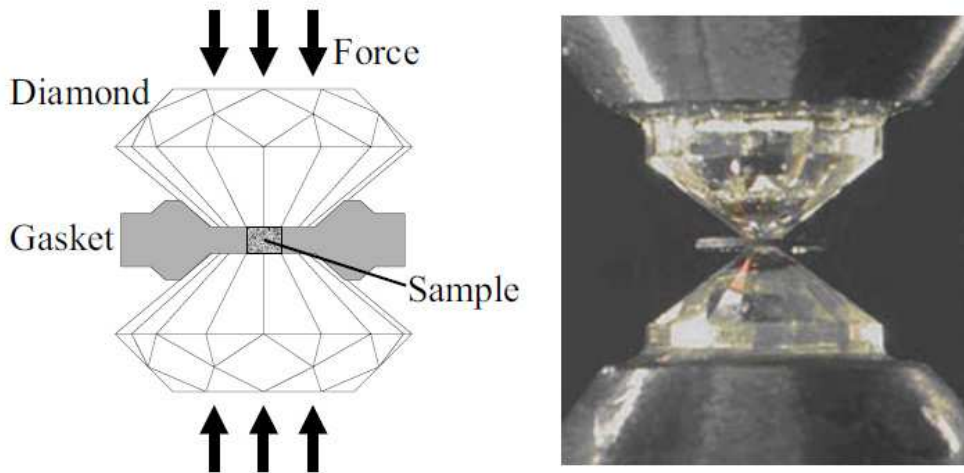


Figure 2.1: Left: schematic representation of a DAC; right: real view from a lateral window in a symmetric cell.

Membrane DACs with Chervin and Le Toullec design [107, 108] have been used for the experiments performed at ESRF (ID24 and ID27 beamlines) and SOLEIL (beamline ODE), while screw membranes with symmetric design have been used for the experiments at APS (beamlines 4ID-D and HPCAT). In the membrane cells the pressure on the sliding piston results from the deformation of a thin membrane by effect of a He pressure (Fig. 2.2 left panel). The screws cells are equipped with four external screws (two left hand and two right hand) which can be driven simultaneously by a motor system called gear-box [109] (Fig. 2.2 right panel). In both cases the force is applied homogeneously on the plates and allows a fine pressure control. Moreover, the possibility to change the pressure on-line without the need of moving the cell makes these types of DAC particularly suited for experiments using SR where the alignment of the sample is a delicate and sometimes long procedure.

Due to the presence of a magnetic field, X-ray Magnetic Circular Dichroism experiments require the use of amagnetic DAC made of CuBe or Titanium.

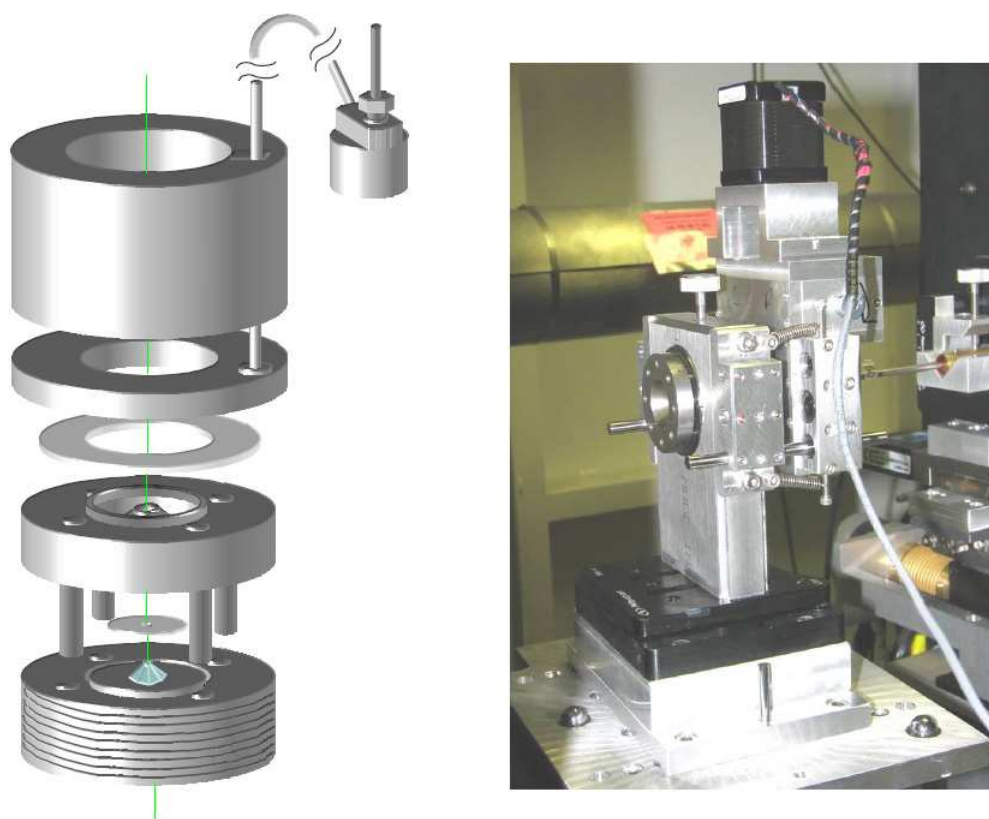


Figure 2.2: Left: schematic representation of a membrane DAC; right: Gear-box system at HPCAT (APS).

Diamonds

Diamonds are suitable anvils due to their hardness and transparency to electromagnetic radiation, which make the DAC well adapted for spectroscopic studies - such as Raman, infrared spectroscopy, X-ray absorption - and X-ray diffraction. The diamond anvils are cut from natural, gem quality stones to have an octagonal or hexadecagonal shape, which is preferred for the better withstanding of stress gradients. Great care must be taken in centering and aligning the two anvils to avoid premature failure of diamonds at high pressure. The adjustment procedure is made under the microscope: the concentricity is achieved moving the support of the piston diamond slightly to superimpose the two polygons corresponding to the faces of the anvils; the parallelism is checked by observing the interference fringes that appear when the two anvils are not parallel.

All spectroscopic studies, as well as XRD, are best carried out by transmitting radiation through a small conical hole drilled in the backing plate, passing through the upper anvil into the sample. The transmitted radiation from the sample area and much of the scattered photons passes through the lower anvil exiting via a similar conical hole in the lower backing plate into an appropriate detector (Fig. 2.3 left panel). Despite the relatively high transparency of diamonds to light and X rays, the usual thickness of a pair of 1/4-

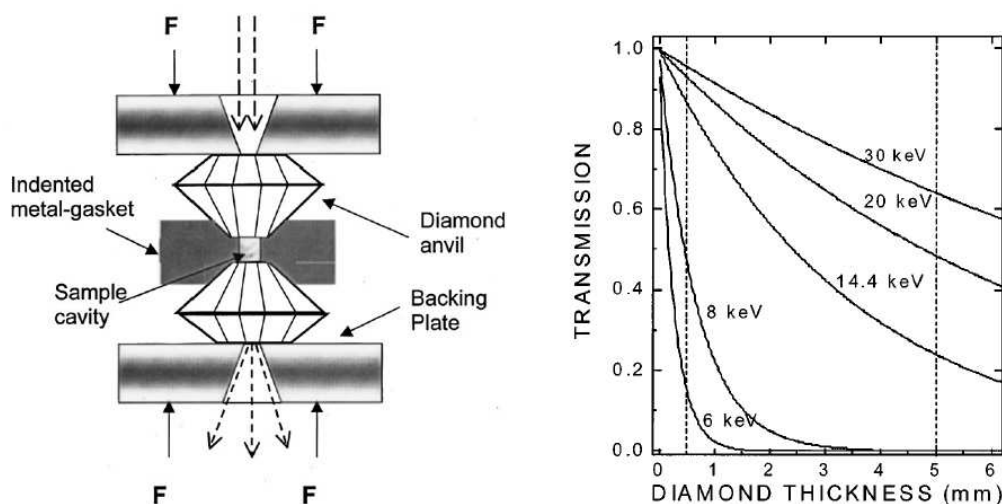


Figure 2.3: Left: transmission geometry in a DAC; right: relative transmission through the diamond for different photon radiation energies from [110].

1/3 carat anvils may create a significant impediment to radiation transmission. In the case of X rays, the 5 mm diamond thickness of a pair of 0.3 carat anvils will essentially block the transmission of photons for $E < 10$ keV (see Fig. 2.3 right panel). Alternative schemes have thus been developed to increase the transmission [110]. One possibility is to use a partially perforated anvil facing a totally perforated anvil with a mini-anvil glued on top as represented in Fig. 2.4. This kind of setup was used in the experiment at 4ID-D (APS) (see chapter *Iron-cobalt alloys*). This geometry of course increases the possibility of diamond failure and makes the anvils alignment more complex because the back surface of the partially perforated diamond is not optically transparent.

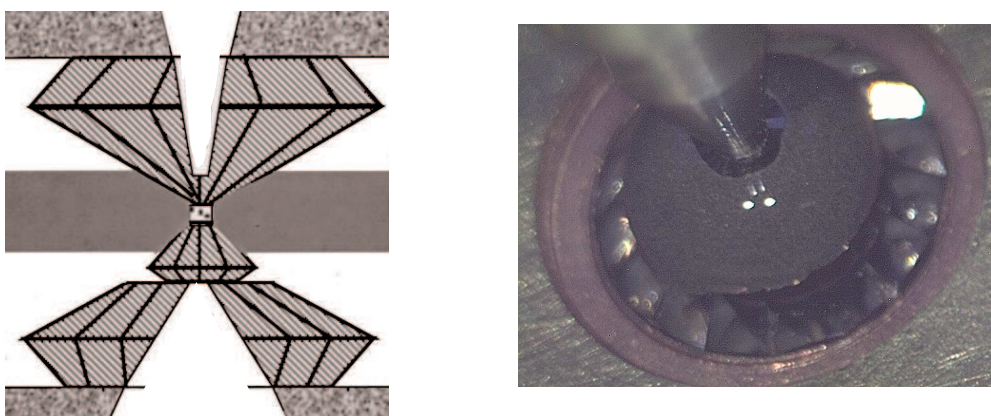


Figure 2.4: Left: DAC scheme using totally perforated and partially perforated diamonds; right: gluing of a top mini anvil.

Gaskets

As the anvils are forced together, the sample placed between them is trapped and develops a uniaxial pressure, whose distribution ranges from a maximum at the center to essentially zero pressure at the edge of the sample area [111, 112]. In order to have an isotropic pressure distribution the sample must be embedded and confined in a pressure transmitting medium softer than the sample. To encapsulate the sample and the hydrostatic medium, both are placed in a small hole drilled in a metallic gasket (Fig. 2.1) placed between the two diamonds. The gasket consists of a metallic foil of typically 200 μm of thickness. The capability of containing extremely high pressure originates from the anvil-gasket friction and the gasket small thickness [113]. To increase the hardness of the metal, thus avoiding large deformation and instability of the hole, the foil is pre-indented to a thickness slightly greater than the final thickness, which depends on the maximum pressure that is planned to be applied. The higher the pressure that has to be achieved during the experiment, the higher the pre-indentation pressure and the smaller the final gasket thickness (and sample volume). A hole in the pre-indented gasket is then drilled by electro-erosion or laser. The diameter of the hole depends critically on the diameter of the diamond flat, and it is typically one third of it. Table 2.1.1 shows typical values of anvils flats diameters, indentation thickness and corresponding maximum pressures reachable. A second purpose of the gasket is to provide support at the edges and sides of the anvils thus preventing failure of the anvils at very high pressures. The out flown gasket materials provides a massive support which assists the pressure containment. Moreover the diamonds imprint allows to set the gasket during the loading procedure in the same orientation as it had during indentation.

In this work stainless steel and Rhenium have been used as gasket materials for XRD measurements (for $P < 40$ GPa and $P > 40$ GPa respectively) and amagnetic Inconel and Rhenium gaskets for the XMCD experiments (for $P < 40$ GPa and $P > 40$ GPa respectively).

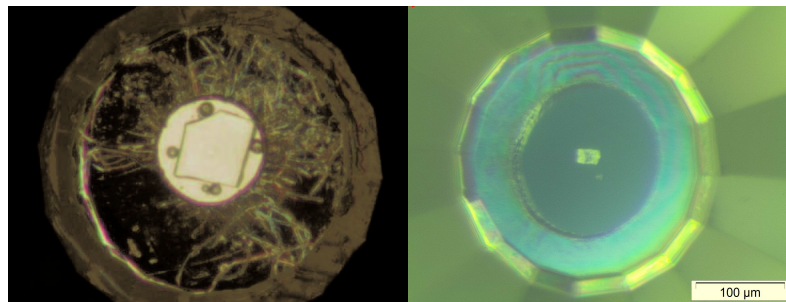


Figure 2.5: Typical loadings for high pressure experiments. During gas loading the hole may shrink to half of its initial size, therefore a bigger hole has to be drilled and the sample placed in the center far away from the gasket borders (right panel).

flat diameter (μ)	indentation thickness (μ)	P max (GPa)
>500	50-60	< 20
300	40-45	50-70
150	25-30	100-150
< 100	20-25	>150

Table 2.1: Typical values of anvils flats, indentation thickness and corresponding reachable pressures.

Hydrostaticity and pressure transmitting media

The uniaxial compression of diamonds acts directly on the media that transmit hydrostatic pressure to the sample. If the pressure transmitting medium solidifies, the hydrostatic conditions inside the cell volume are no longer achieved and the sample is subject to a pressure gradient: i.e. the stress is not uniform in all directions. The variation of stress conditions at different points in the sample depends upon the strength of the medium. The hydrostatic limits of several pressure transmitting media were determined [114] by using the ruby line broadening (see next section), or by measuring the pressure homogeneity with several ruby chips over the area of the gasket aperture. The transmitting medium must not chemically react with the sample and must not interfere with the measurement of the sample. For example, in a X-ray absorption experiment, it must not have an absorption edge in the energy range of interest.

Typical transmitting media can be liquids (alcohol, alcohol mixtures (Methanol-Ethanol 4:1), silicone oil), soft solids (alkali halides, NaCl, KBr, etc), hard solids (MgO, Al₂O₃, etc) and condensed gases (He, Ne, N₂, Ar, etc). Liquids are in general quite easy and fast to handle but have a quite low hydrostaticity limit (< 10 GPa); solids, also not hydrostatic up to high pressures, are generally chosen for laser heating experiments thanks to their insulating properties; gases, providing the highest hydrostaticity, are the best pressure media for room and low temperature experiments but they are difficult to load without gas-loading or cryogenic devices. X-ray diffraction (XRD) studies have proved that non-hydrostatic stress using He can be negligible up to around 100 GPa [115].

In the experiments presented in this Thesis two kinds of transmitting media have been used: Silicone oil for the XAFS (X-ray Absorption Fine Structure) experiments and gas (He or Ne) for the XRD experiments. In the case of cobalt the XAFS experiment was also performed using Ar. Let's briefly discuss the reasons for this choice.

Silicone oil is liquid up to 5 GPa and quasi-hydrostatic up to 13 GPa; its viscosity increases gradually with increasing pressure. Despite its low hydrostatic limit, this medium is widely used for XAFS experiments. This because hydrostatic conditions are less stringent than in XRD. In fact XAFS directly probes the very local environment around the absorber, limited to few Å, and this information is intrinsically less sensitive to pressure gradients. On the contrary XRD peaks are generated by long range order (i.e. they require

several unit cells) thus they are more affected by the pressure gradients within the sample. Gradient pressure may in principle induce anisotropic strain modifying the physics of the system. However it has been extensively demonstrated in the case of pure iron, that different shear strength of pressure transmitting media can influence the transition onset and width [90] but do not change the physics of the system as the same structural and magnetic transitions have been reported using very different media including silicone oil. The data presented in this Thesis furnish a further proof. In the case of cobalt two runs of XAFS measurements have been performed using Silicone oil and Argon as transmitting media up to around 100 GPa. The observed evolution of XANES and XMCD resulted the same within the error bar (see the *Cobalt* chapter). In the case of the FeCo alloys we have performed XAS and XRD experiments using Silicone oil and gas respectively for several samples (see the *Iron-cobalt alloys* chapter). In each case the same pressure induced structural transition has been observed with only a transition width enlargement of 3-4 GPa in the case of Silicone oil.

In Fig.2.5 we show examples of sample loading in the DAC. During gas loading the hole diameter typically reduces of 2/3 or even of half of its initial size. A bigger hole (half of the diamond flat) has to be drilled and the sample loaded in the center far from the gasket borders (see Fig.2.5 right panel).

2.1.2 Pressure measuring methods

Several methods for measuring pressure have been developed. They can substantially be divided into two classes: those in which an optical sensor (ruby, samarium doped yttrium-aluminum garnet (Sm:YAG), diamond, or cubic boron nitride) is used as pressure gauge due to the established pressure dependence of its luminescence or Raman spectra [103, 116], and those which rely on X-ray standards (like Au, Pt Cu, etc). In this second case the pressure is determined from the lattice parameters obtained from the diffraction pattern or from the absorption spectra [117] through an assumed equation of state.

The most common method for measuring the pressure is the ruby fluorescence technique. This method is particularly well adapted to DAC technology since it exploits the high transparency of diamonds to visible light. Forman and co-workers [118] first showed that the luminescence doublet of peaks R_1 and R_2 of Cr^{3+} -doped Al_2O_3 (ruby lines) shift linearly with hydrostatic pressure in the range of 1-22 kbar, and that the two lines broaden if the ruby experiences nonhydrostatic stresses. In this method [119] a tiny chip of ruby (5-10 μm in dimensions) is placed in the pressure medium along with the sample (Fig. 2.5), and its luminescence is excited by a laser (both He-Ne or argon ion lasers are proper to use) and analyzed by a monochromator. The shift in wavelength is followed as a function of pressure. The pressure calibration is typically performed by means of the more intense R_1 (Fig. 2.6) line whose pressure dependence was established and improved during the years by extrapolating state-equations and non hydrostatic data from shock-wave experiments [62, 120–122]. According to [122], the relationship between the pressure P (in

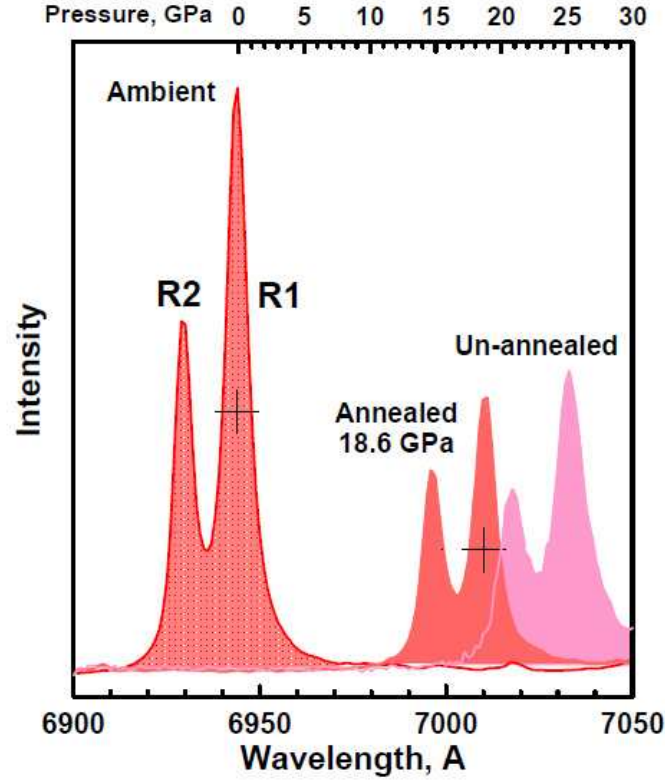


Figure 2.6: Example of pressure calibration using the ruby fluorescence technique.

GPa) and the ruby R_1 line wavelength shift $\delta\lambda$ (in nm) can be described by (at 20 °C):

$$P = \frac{1904}{B} \left[\left(\frac{\delta\lambda}{694,24} \right)^B - 1 \right] \quad (2.1)$$

where the parameter B is equal to 7.665 and 5 for quasi-hydrostatic and non-hydrostatic conditions respectively. In the 0-30 GPa range the linear extrapolation $P = \alpha\delta\lambda$ with $\alpha = 2,74$ GPa/nm can be adopted. A very recent comprehensive review by Syassen on the ruby method summarizes presently available literature and addresses the contemporary efforts aimed at the improving of the ruby pressure scale calibration [116].

The position of the ruby luminescence lines varies with temperature, with a slope of 0.068 Å/K, which means that a $\Delta T \approx 5$ K produces the same shift as the application of a pressure of 0.1 GPa. Therefore a variation of temperature from ambient conditions has to be taken into account for a precise determination of pressure. Temperature correction of the ruby pressure scale has been studied in the 1990s [123, 124] and more recently up to 95 GPa and 800 K [125]. In perfect hydrostatic conditions the ruby fluorescence technique gives a pressure indetermination of ± 0.1 GPa in the 0-10 GPa range and ± 0.5 GPa for pressure up to 30 GPa. However, pressure gradients on the sample may be larger,

depending on the pressure transmitting medium used. In the experiments of this Thesis we have estimated the pressure error due to gradients by measuring fluorescence from 2-3 ruby spheres places in different region of the pressure chamber.

2.2 X-ray Absorption Spectroscopy

When an X-ray beam hits an homogeneous sample of thickness d , its intensity I_0 is attenuated according to the law:

$$I = I_0 e^{-\mu d} \quad (2.2)$$

where I is the beam intensity after the sample and μ is the absorption coefficient which depends on the X-ray beam energy and on the sample density and atomic species. When the incident energy matches the energy needed to excite the electrons from a deep layer to the continuum, the absorption increases sharply, showing a peak (or absorption edge) at that value of the energy. The absorption edges are named following the principal quantum number of the electronic state excited. For example, the edges K, L₁, L₂ and L₃ correspond to excitations of electrons in the levels 1s, 2s, 2p_{1/2} and 2p_{3/2} respectively.

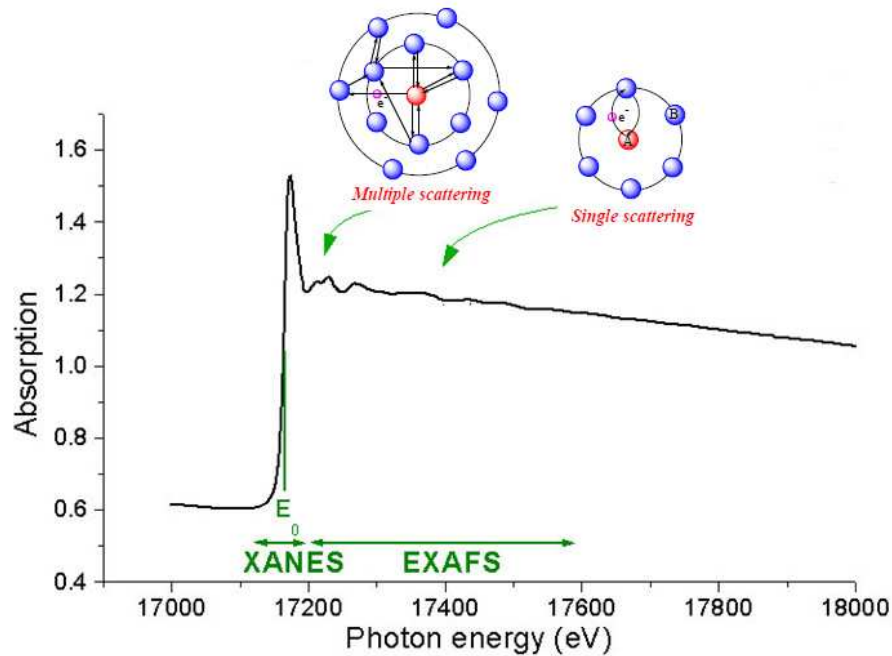


Figure 2.7: XAS spectrum for the L₃ edge of Uranium in the substance Calciumuranat(CaUO₄).

In the condensed matter, above the absorption edge, a fine structure extending to about 1000 eV appears. The reason why this fine structure is observed is the following: the photoelectron emitted in the absorption process propagates like a spherical wave from the absorbing atom. If other atoms surround the absorber, the wave is scattered back by them. Thus, outgoing and scattered waves interact constructively or destructively depending on the energy of the photoelectron and on the absorber-scatterer distance, increasing or decreasing the absorption intensity respectively. In this fine structure three regions can be distinguished:

- the edge region, up to 8-10 eV above the absorption edge.
- the X-ray Absorption Near Edge Structure (XANES) region, up to 50-60 eV after the absorption jump. In this area the photoelectron is able to interact with many neighbors atoms through multiple scattering processes. The XANES contains information about the electronic structure and geometrical symmetry around the absorber.
- the Extended X-ray Absorption Fine Structure (EXAFS) range, which extends up to about 1000 eV above the absorption threshold. This region is dominated by single scattering excitations, in which the photoelectron is scattered only once by each neighbor, and brings informations about the local structure around the absorber.

An example is shown in Fig. 2.7.

2.2.1 X-ray Magnetic Circular Dichroism

X-ray Magnetic Circular Dichroism (XMCD) measures the dependence of X-ray absorption on the helicity of the x-ray beam by a magnetic material. It is the X-ray equivalent of Faraday or Kerr effects which occur in the visible range. The XMCD signal is obtained by taking the difference between X-ray absorption spectra measured using parallel (μ^+) and antiparallel (μ^-) orientations of the sample magnetization relative to the incident photon helicity:

$$XMCD \equiv \mu^+ - \mu^- \quad (2.3)$$

The physical origin of the XMCD effect can be explained by a simple two step model originally proposed by Schütz [126] and revised later by Stohr and co-workers [127] as schematized in Fig. 2.8.

In the first step, right or left circularly polarized photons transfer their angular momentum, \hbar and $-\hbar$, respectively, to the excited photoelectron. Because the spin does not interact directly with the electric field, in the absence of spin-orbit coupling, one can only transfer the photon angular momentum to the orbital part. This is the case for the excitation from an atomic s core state. If the core-state is split by the spin-orbit interaction,

the substates are no longer pure spin states. As a result, the photon angular momentum is transferred to both the orbital and spin degrees of freedom of the excited photoelectron. This is known as the Fano effect [128]. In fact, a relatively large portion can be transferred to the spin resulting in spin polarized photoelectrons. For the $p_{3/2}$ initial state (L_3 edge), for example, \vec{l} and \vec{s} are parallel, therefore a transfer of the angular momentum \hbar by right circularly polarized light excites more spin up (62.5%) than spin-down electrons (37.5%). The reverse holds for left circularly-polarized light. For the $p_{1/2}$ initial state (L_2 edge) \vec{l} and \vec{s} are anti-parallel and right circularly polarized light preferentially couples to spin-down electrons (75% spin-down and 25% spin-up electrons). Again, left circularly polarized light does the opposite. Taking into account the two times higher population of the $p_{3/2}$ state, one finds that the spin polarizations of the photoelectron yield from the L_3 and L_2 edges are identical in magnitude and opposite in sign. In the first step, spin-up and spin-down are defined relative to the photon spin direction, and the discussed effects are therefore independent of the magnetic properties of the sample.

The magnetic properties enter in the second step. Here the valence shell acts as a "detector" for the spin and/or orbital momentum of the excited photoelectron. The quantization axis of the detector is given by the magnetization direction which, for maximum dichroism effect, needs to be aligned with the photon spin direction. If the metal is ferromagnetic, an imbalance in empty spin-up and spin-down states will exist and hence the valence shell can act as a "spin detector". Similarly, the valence shell will act as an "orbital momentum detector" if there is an imbalance of states with different magnetic quantum numbers m_l , i.e. in case of spin-orbit splitting in the valence shell. Therefore, for K-shell excitation or for summed L_3 and L_2 spectra, a dichroism effect exists only if the valence shell exhibits an orbital moment. By separating the L_3 and L_2 components one becomes sensitive to the spin.

In the above discussion we have assumed that the magnetization direction is fixed so that the XMCD intensity is the difference intensity, obtained for two X-ray helicities. It is easy to show that it is equivalent to fix the X-ray helicity and switch the magnetization direction [127]. The XMCD arises from directional spin alignment, as in a ferromagnet or ferrimagnet, and is not sensitive to paramagnetism or antiferromagnetism, which could be instead discriminated by means of X-ray Magnetic Linear Dichroism.

In the 1990s, concurrent to the XMCD experimental developments, important sum rules have been derived that link the polarization dependent X-ray absorption intensities to the ground state properties of the valence band, in particular the number of holes per atom [129], the spin magnetic moment per atom [130] and the orbital moment per atom [131]. Because of their significant implications, numerous experimental and theoretical studies aimed at testing their validity have been carried out but with widely different results (see [132] and references therein).

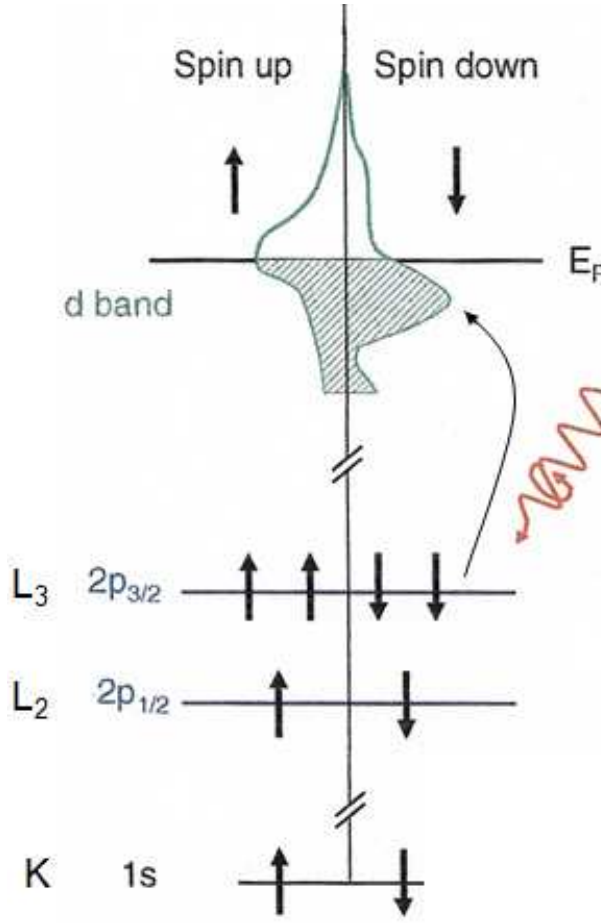


Figure 2.8: Two step model describing polarized X-ray absorption from the L edges.

2.2.2 XMCD on the 3d metals under high pressure

The investigation of magnetism in the 3d metals using XMCD is generally carried out at the L-edges, which directly probe the spin polarized d final states. However, these edges are not accessible at high pressure in a diamond anvil cell due to the opacity of the diamond anvil at such low energies ($E=700-900$ eV). It is necessary instead to probe the K-edges making the experiment complex both from an experimental and interpretational point of view.

As already mentioned, for K-edge excitations the $1s$ core shell has zero angular momentum and hence no spin-orbit coupling¹. The photon spin is thus transferred to the photoelectron as an orbital angular momentum which can be detected by the valence shell only if it possesses an orbital magnetic moment itself, that means if the valence band empty density of states has an unbalance of states with quantum numbers $+m_l$ and $-m_l$. Therefore, for K-shell excitations a dichroism effect exists only if the p valence shell possesses an orbital moment [133], and sensitivity to the spin moment of the p shell arises

¹It may however exhibit a small splitting into $m_s=\pm 1/2$ states due to the exchange field or an external magnetic field [16].

only indirectly through the spin-orbit interaction.

In the 3d metals the orbital angular moment is largely quenched by the crystal field and the spin-orbit interaction is rather weak, therefore the K-XMCD signal is generally very small ($\sim 10^{-3}$ or weaker) and hard to detect.

2.2.3 Interpretation of the K-edge XMCD signal

The interpretation of the K-edge XMCD signal is nowadays still controversial and it is quite difficult to extract absolute quantitative information on the magnetic moments. On the other hand it can be successfully applied to investigate the relative magnetic response of a material to the application of external agent like pressure or temperature.

K-edge XMCD is due to many contributions but mainly arises from the spin-orbit (SO) coupling of the photoelectron in the final state. The Thole orbital sum rule [131, 133, 134] directly relates the integrated K-edge XMCD to the expectation value of the p -projected orbital moment.

$$\frac{\int_{E_f}^{E_c} d\omega (\mu^+(\omega) - \mu^-(\omega))}{\int_{E_f}^{E_c} d\omega \mu^0(\omega)} = \frac{3\langle L_z \rangle_p}{n_p^h} \quad (2.4)$$

Based on an atomic approach and the dipolar approximation, its application to the K-edge of the 3d metals is limited by the assumption of energy independent radial matrix elements $R = \langle 1s|r|4p \rangle$ which does not apply to the broad and delocalized p final states [133, 135]. Nevertheless, it was first pointed out by Gotsis and Strange [136] and Brooks and Johansson [137] that, as the energy dependence of the matrix elements is smooth, the K-edge XMCD reflects the p orbital polarization in differential form $d\langle L_z \rangle_p/dE$. More recently this has been verified by Antonov and co-workers for the Fe_3O_4 system [138].

Other theoretical approaches for the interpretation of K-edge XMCD signals based on multiple-scattering calculations [135, 139–141], claim that an important contribution to the K-edge signal in the 3d metals comes from the spin-polarization of the d -states and arises from the scattering of the photoelectron from the spin-orbit potential of the neighbors and of the absorber. In particular according to [141] the dichroic cross section is equal to the sum of three terms:

$$\sigma_{XMCD} = \text{Im} \left[\sum_s (-1)^{s-1/2} [\sigma_{1a}^s(E + i\Gamma) + \sigma_{1l}^s(E + i\Gamma) + \sigma_{1n}^s(E + i\Gamma)] \right] \quad (2.5)$$

where σ_{1a}^s describes the purely atomic contribution to XMCD (related to the Fano effect), σ_{1l}^s provides the local contribution due to the spin polarization of the p -states on the absorbing site, and σ_{1n}^s is the contribution due to the scattering of the photoelectron by the spin-orbit potential of the neighbors and the absorber itself. The p, d, f, \dots orbitals of each atom of the cluster give a specific contribution to σ_{1n}^s . The expansion of σ_{1n}^s

into orbitals and sites is thus used to determine the physical origin of some peaks of the XMCD spectra. In the case of Co K-edge XMCD, the main peak at 5 eV results from the sum of all the three contributions, which have comparable amplitudes; nevertheless as σ_{1a}^s and σ_{1l}^s have roughly the same intensity and opposite sign the main XMCD valley is mainly due to the p and d components of the σ_{1n}^s term [141].

The role of the spin-orbit interaction of the $3d$ states on the neighboring sites was also reported by Igarashi and Hirai [134, 142] using tight-binding calculations, and by Guo [133] within an itinerant electronic model. These authors showed that the XMCD at the K edge in the $3d$ metals is determined by the orbital moment on the $3d$ states through the p - d hybridization and that the spin-orbit interaction of the $4p$ (ξ_p) or $3d$ (ξ_d) states can be artificially "turned off", revealing a dominant role of ξ_d . An example is shown in Fig. 2.9 for the nickel case.

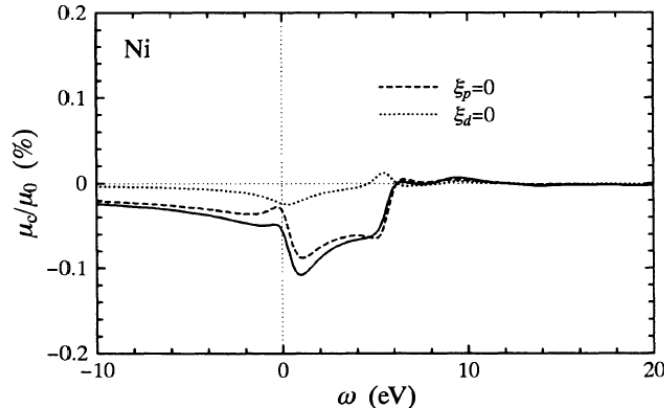


Figure 2.9: Tight binding calculation of the K-edge XMCD of Ni by changing the spin-orbit coupling from [134].

These studies had led to the conclusion that the K-edge XMCD signal should be somehow proportional to the $3d$ spin magnetic moment [95], and its pressure evolution has been often compared to that of the total spin magnetization [42, 63].

One of the aims of this Thesis has been to get a deeper insight into the K-edge XMCD interpretation by analyzing the K-edge XMCD response under pressure and exploiting the fruitful collaboration with the ESRF Theory group. Total spin magnetization calculations by Jarlborg [45] and Mohamed [43] describe quite well the behavior of the K-edge XMCD under pressure in iron, but this is not the case for cobalt and nickel, as discussed in the dedicated chapters. The nickel case has been chosen as a first step because of its simplicity, not presenting structural transitions in the investigated pressure range. Our results (extensively presented in the *Nickel* chapter) indicate that the pressure induced decrease of the Ni K-edge XMCD closely resembles that of the p -projected orbital moment rather than that of the total spin moment. At very high compression all components (p and d orbital and spin moments) are suppressed simultaneously. This is not surprising

since in the *3d* metals the orbital moment, quenched by the crystal field, only arises from the spin-orbit interaction. Therefore, the observation of a non-zero K-edge XMCD signal clearly indicates the presence of a non-zero spin moment and, as well, the observation of a zero signal indicates the loss of ferromagnetism.

As a last remark it is important to underline that XMCD (in general, not only from the K-edge) arises from directional moment alignment and is thus sensible to the net magnetic moment. Hence, when the signal goes to zero, under the effect of pressure, we cannot distinguish whether the sample has become really non-magnetic (with zero elementary moment), paramagnetic or antiferromagnetic since all these configurations correspond to a zero net moment.

2.3 Polarized XAS under high pressure: experimental details

Polarized X-ray absorption spectroscopy contains intrinsic structural, electronic, and magnetic probes. These are, respectively, EXAFS, XANES and XMCD. The first two are able to clearly differentiate the signature of the local symmetry, while the third is very sensitive to polarized magnetic moments variation (as discussed in the previous section). Thus, for each pressure point, simultaneous information on both the magnetic and the structural properties of the system can be obtained - i.e. exactly on the same region of the sample and in the same thermodynamic conditions - without any relative pressure incertitude. This is very important in the high pressure domain where the reproducibility of high-pressure hydrostatic conditions is difficult to obtain.

With respect of other magnetic probes which can be performed at high pressure - such as susceptibility measurements by the inductance method [143], neutron diffraction [144], Mössbauer spectroscopy [145] and inelastic X-ray scattering [92]- XMCD takes advantage of its element and orbital selectivity, its sensitivity in the detection of very small magnetic moments ($0.01\mu_B$) and its above mentioned intrinsic information content on local structural and electronic properties through the XAS signal. Nowadays XMCD is the only magnetic probe able to reach the 10^2 GPa range, with the exception of Mössbauer techniques [98] whose application is anyway limited by the small number of Mössbauer isotopes, which excludes a large number of magnetic materials.

Measuring XMCD at the K edges of 3d transition metal elements on samples subjected to high pressure is however a very challenging experiment due to the following reasons:

- **A very small signal**

As explained in the previous section, K-edge XMCD signals originate from the weak spin-orbit coupling in the final state and are typically of the order of 10^{-3} or less under saturation conditions.

- **Low X-ray transmission**

Best results for high-pressure XAS are obtained in the transmission geometry, where the X-ray beam passes through the highly absorbing diamonds of the high pressure cell. The transmission of the X-ray beam at the Fe K edge (7100 eV) through a pair of 1.2 mm-thick diamonds is lower than 0.4% and falls below 0.07% at 6.5 keV. Moreover, in order to generate circularly polarized X-rays a phase retarder (quarter wave plate) has to be used introducing additional absorption at low energies.

- **A very small sample**

As discussed in sec. 2.1.1, in order to reach the 10^2 GPa range, the diamonds flat diameter must not exceed $100\ \mu\text{m}$ and the gasket hole diameter will be approximately one-third of this value. Therefore required sample sizes can be smaller than $20\ \mu\text{m}$.

Hence the collection of good quality high pressure XMCD data requires: i) **spectral and spatial beam stability**, as the required signal-to-noise ratio is obtained by averaging a large number of spectra; ii) **high flux**, to compensate for the high level of absorption in the diamond cell and in the quarter-wave plate and to reach the required signal-to-noise level; iii) and a **small focal spot** to avoid renormalization problems due to incident X-ray leaking around the sample or hitting the gasket.

As will be shown in the next section the energy dispersive geometry in conjunction with the high brilliance X-ray beams of third generation synchrotron sources are particularly suited for HP studies using DACs, and fulfill all the technical prerequisites described here.

2.3.1 The dispersive beamline ID24

Beamline ID24 is the ESRF XAS beamline with parallel detection of the whole spectrum made possible by energy dispersive (ED) highly focusing X-ray optics [146, 147]. This beamline has been the first of its kind to be installed on a third generation synchrotron radiation (SR) source.

The dispersive XAS concept is illustrated in Figure 2.10. A polychromatic beam, supplied by a SR source, is dispersed and focused by an elliptically curved crystal [148, 149]. Because the incident X-rays strike the crystal at slightly different angles along its length, the bent crystal acts as a polychromator diffracting a different energy at each point. This energy-dispersed beam converges to a focal point at the sample position. The beam, transmitted through the sample, then diverges towards a Position Sensitive Detector (PSD). The position of the beam, incident in the detector, can be directly correlated to energy. The X-ray absorption spectrum is obtained by taking the logarithm of the ratio of I_0 data and I_1 data, where I_0 and I_1 are spatial X-ray intensity distribution in the absence and presence of the sample, respectively. Harmonic rejection, which is crucial for samples in highly absorbing environments, is achieved using a system of mirrors placed before and after the polychromator. In order to produce reliable, accurate structural data, the EDXAS optics must be capable of delivering a wide bandpass (ΔE) of radiation maintaining an adequate energy resolution $\delta E/E$.

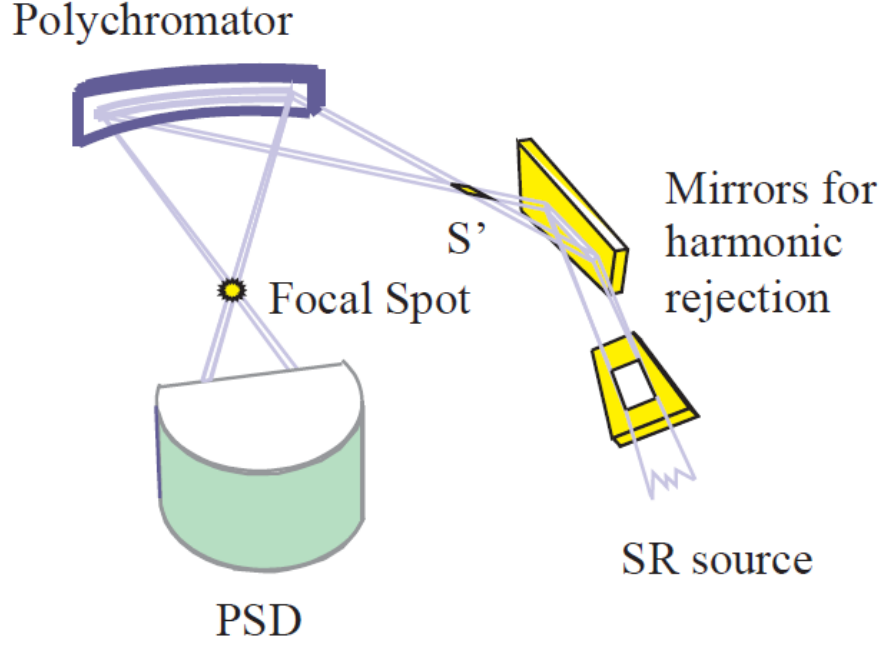


Figure 2.10: Scheme of the dispersive XAS concept.

In beamline ID24 the radiation source consists of three low K tapered undulators in a high β section of the ring. The choice of an undulator is unusual taking into account that all other operating dispersive XAS beamlines worldwide are installed on bending magnet or wiggler sources. The latter sources naturally yield the large horizontal divergence (typically a few mrad) necessary to obtain, with reasonable radii of curvature of the polychromator crystal, an energy dispersion that covers a whole XANES or EXAFS spectrum. However, the choice of an undulator has clear advantages [150]: 1. the possibility to match the bandwidth of emission of the undulators and the acceptance of the polychromator by optimizing the gap, the taper and the radius of curvature of the polychromator crystal. This results in a reduction of heat load on the optics; 2. a substantial reduction of unwanted harmonics; 3. higher brightness and lower vertical divergence; and 4. low monochromatic divergences (horizontal and vertical), which allows the optimal exploitation of the properties of quarter wave plates to tune the helicity of incoming photons.

The absence of mechanical movements of the energy-dispersive spectrometer during the acquisition of spectra and the strongly focusing polychromator crystal yield the required spot stability and dimensions respectively for HP studies using DACs. Instabilities of the energy scale and misalignment of the beam with respect to the aperture of the gasket are therefore strongly reduced. Moreover, in the dispersive setup the transmitted spectrum in the whole energy range is visualized in real time on the PSD. This allows the detection of the energy position of diffraction peaks from the anvils, and to shift them until they

disappear from the energy region of interest by changing the orientation of the diamonds.

2.3.2 The HP XMCD setup

Fig.2.11 illustrates the present optical scheme for XMCD measurements. It consists of a pair of mirrors in a Kirkpatrick-Baez (KB) geometry, a Si polychromator, a diamond quarter-wave plate (QWP), a third vertically refocusing mirror, a sample environment (the diamond anvil cell, a spectrometer for pressure calibration and the electromagnet) and a position-sensitive detector that transforms the energy-direction correlation into an energy-position correlation [151].

The horizontal divergence necessary to obtain the requested energy bandwidth (ΔE) after diffraction from the polychromator is produced by the second KB mirror. Placed at 32.5 m from the source, this strongly focusing mirror creates a horizontally-demagnified image of the source that becomes the effective source S' for the polychromator crystal (Fig. 2.10), 1.8 m downstream (34.3 m from the source), and leads to a horizontal divergence of 1 mrad.

The polychromator vessel is located 64 m from the undulator source. The distance to the effective source S' amounts to 29.7 m. The polychromator consists in a curved Si crystal in a Bragg [152] or Laue [153] geometry. The beam is focused at 1.5 m from the polychromator crystal at the sample position leading to a horizontal divergence of ≈ 30 mrad. Si(111) and Si(311) crystals are used to match the energy resolution/energy bandwidth requirements for the specific applications. In the Bragg geometry, X-ray penetration depth effects at high energies introduce extended asymmetric tails in the reflectivity curve and in the focal spot distribution, which limit the use of this geometry to the energy range ≈ 5 -13 keV. Above these energies, a curved asymmetric ($\alpha = -6^\circ$) Laue crystal is used.

At the energies corresponding to the K edges of $3d$ transition metals, the full dimensions of the focal spot are below 20 μm in both directions (it can reach 5 μm full width at half maximum). The total energy range ΔE diffracted by the polychromator is of the order of 300-400 eV, allowing access to the edge region (XANES) and to the first few EXAFS oscillations (up to a photoelectron wavevector $k \approx 8$ -10 \AA^{-1}).

The QWP is located 750 μm downstream of the polychromator. It consists, for the energy range of the K edge of the $3d$ transition metals, of a thin (740 nm) perfect diamond crystal in the Laue geometry. Its birefringence properties close to a Bragg reflection transform the linearly polarized incident X-ray beam into a transmitted (non-deviated) beam with circular polarization very close to unity [154]. The very small source divergence and the non-dispersivity condition allow circular polarization close to unity to be obtained on the whole polychromatic and divergent fan [155]. XMCD applications on ID24 currently cover a wide energy range that extends from the L edges of rare earths (down to the L_3 edge of Ce at 5.7 keV) up to the L edges of $5d$ metals (up to the L_2 edge of Pt at 13.3 keV).

The third mirror is installed on the polychromatic beam after the QWP, 0.6 m upstream

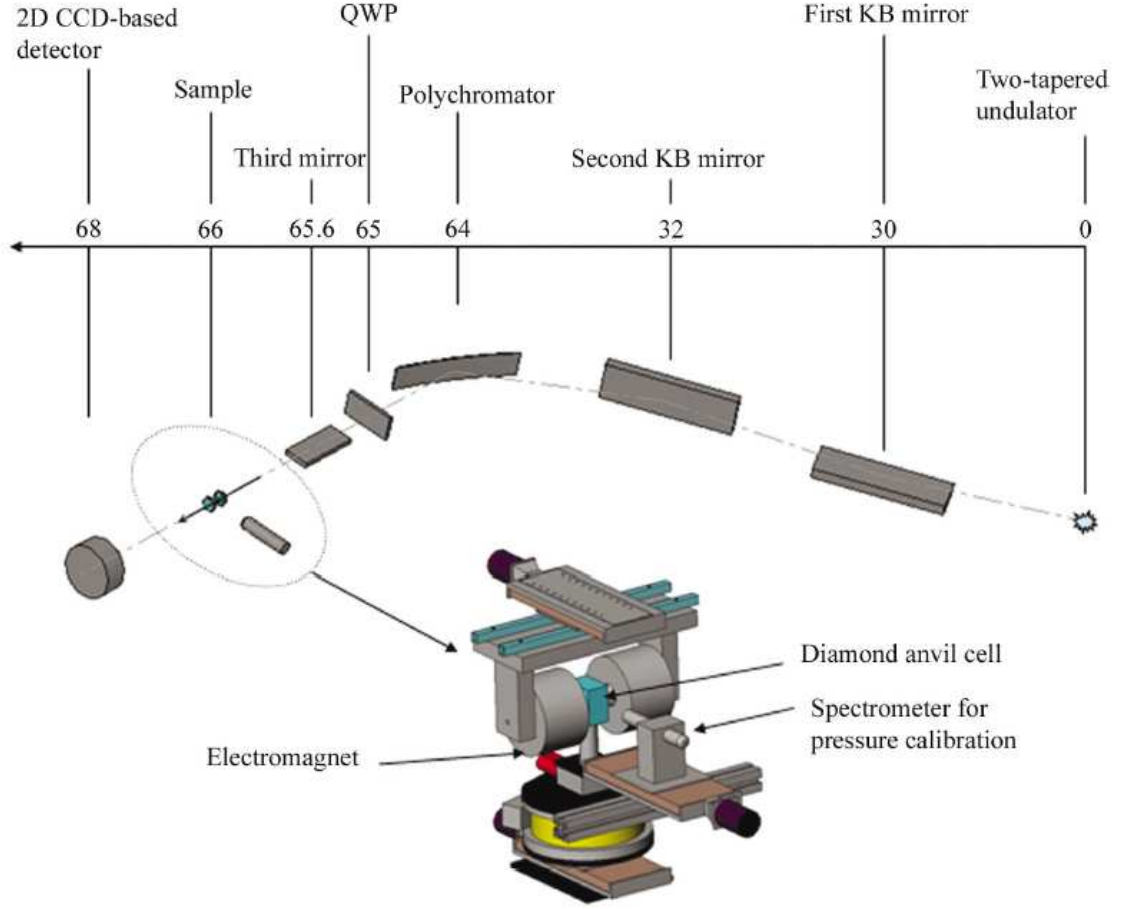


Figure 2.11: ID24 optical scheme and sample environment for XMCD at high pressure (not in scale).

of the focal point to refocus the beam in the vertical direction at the sample position [156, 157].

The sample environment has been specifically developed for high-pressure XMCD applications in order to concentrate in a compact volume the high-pressure cell, the laser spectrometer for the pressure measurement (Pressure Ruby Luminescence (PRL) system) and the magnetic field. The high-pressure cell is made of non-magnetic CuBe, manufactured by the *Physique des Milieux Condensés* laboratory at the University of Paris VI. Its design derives from the Chervin type membrane cell [107]. The HP-DAC is located on a stack of motorization stages that allows its alignment to the beam: vertical Z and horizontal X (transverse to the beam direction) translation stages, rotation around the vertical Z axis and around the horizontal X axis and rotation around the X-ray beam direction. The last three stages are used to remove diffraction peaks originating from the diamonds that fall in the energy range of interest.

The XMCD signal is obtained by taking the difference between X-ray absorption spec-

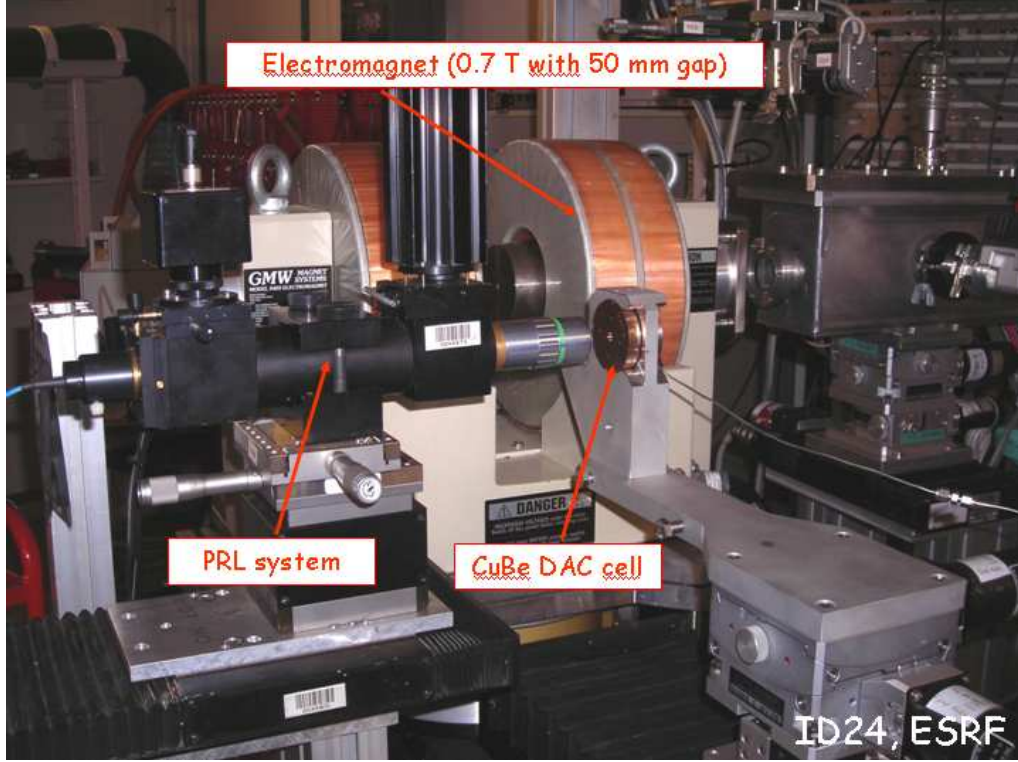


Figure 2.12: Sample environment for XMCD at high pressure at beamline ID24 (ESRF).

tra measured using parallel (μ^+) and antiparallel (μ^-) orientations of the sample magnetization relative to the incident photon helicity:

$$XMCD \equiv \mu^+ - \mu^- = \ln(I_0^+/I_1^+) - \ln(I_0^-/I_1^-). \quad (2.6)$$

In order to reduce systematic errors, at each pressure, the four symmetry cases of the XMCD signal, obtained by flipping the helicity of the incoming photons (R/L) and the magnetic field (\uparrow/\downarrow), are recorded. The XMCD signals are then calculated independently for the two polarization cases and averaged.

If the incident intensity does not change in time, then $I_0^+ = I_0^-$ and

$$XMCD \equiv \mu^+ - \mu^- = \ln(I_1^-/I_1^+) \quad (2.7)$$

However at ESRF the incident intensity decreases with time with electron beam current. This can be taken into account by considering the sequence for the measurement of the transmitted intensity I_1 :

$$I_1^{0-}, I_1^{1+}, I_1^{2-}, I_1^{3+} \dots I_1^{(2n-1)+}, I_1^{(2n)-}$$

where n is the number of the $I_1^- I_1^+$ pairs of acquisitions and adopting the following algorithm for the calculation of the XMCD signal:

$$XMCD = \frac{1}{2n} \ln \left[\frac{I_1^{0-} (I_1^{2-})^2 \dots (I_1^{2n-})^2}{(I_1^{1+})^2 (I_1^{3+})^2 \dots (I_1^{(2n-1)+})^2} \right] \quad (2.8)$$

In this way we effectively suppress linear and exponential drifts of different origins and work exclusively with the transmitted intensities. This is an advantage of energy-dispersive XAS, where it is not yet possible to measure simultaneously the incident and transmitted intensities.

Cobalt

In this chapter we present new high pressure XMCD and XANES measurements on pure Cobalt providing the first experimental evidence of the pressure induced collapse of its ferromagnetism occurring across the hcp-fcc structural transition. In the first part of the chapter a survey of the previous most significative literature, concerning the cobalt high pressure magnetic and structural phase diagram, is given. Then experimental details are presented. Finally our new results are discussed in comparison with previous findings and novel FEFF and DTF calculation. The coupling of combined magnetic (XMCD) and local structure (XANES) measurements to theoretical calculations allows to give a complete description of the high pressure structural and magnetic transitions, highlighting major differences with the iron case.

3.1 Introduction

Cobalt, situated at the center of the magnetic 3d transition metal series, plays a crucial role in the systematic understanding of magnetic 3d elements. It is the thirtieth most abundant element on earth and comprises approximately 0.0025% of the earth's crust. Following iron in the periodic table, is potentially important for the properties of the earth's core, which is believed to be composed of iron-dominated alloys with perhaps Co or Ni as minor components.

Cobalt is used in high temperature alloys of the superalloy type because of its resistance when heated up to fairly high temperatures. It also has good work-hardening characteristics, which contribute to the interest in its use in wear alloys. Cobalt based materials are attractive for their chemical, magnetic, and electronic properties with potential applications as magnetic data storage and catalysis among others [159–161].

The iron phase diagram has been widely investigated. Being one of the most abundant elements of the Earth's mantle and core, its properties are thought to be relevant for various geophysical processes. Upon compression, its ferromagnetic order vanishes around 10-16 GPa [42, 63, 93, 95] in correspondence to the bcc to hcp structural transition and the

onset of superconductivity [73, 162] (see section 1.5). Similar investigations in the case of cobalt are much more challenging due to the higher pressures involved.

Because of the very similar electronic structure and atomic volumes, the magnetic and structural behavior of Co at high pressure and temperature may shed light on the phase diagram of iron. In particular hcp cobalt is considered an analogous element to understand elasticity properties of the high pressure hcp phase of iron. In this sense, the study of cobalt provides some advantages with respect to iron: 1) cobalt crystallizes in the hcp phase at ambient conditions, while the hexagonal phase of iron cannot be quenched to low pressure; 2) it is possible to study single crystal elastic properties of cobalt, while, to date, no single crystal of hcp iron has been grown, even at high pressure. However, a major drawback in using cobalt as an analogous material for hcp iron is the fact that cobalt is ferromagnetic, while hcp iron is nonmagnetic. Thus, in order to properly interpret the experiments on elasticity in cobalt, its high pressure magnetic state must be well understood.

3.2 Extreme conditions structure and magnetism in cobalt

3.2.1 The HP/HT phase diagram

Under ambient conditions cobalt crystallizes into a ferromagnetic hcp structure [163, 231], often coexisting with a metastable cubic close-packed fcc phase [165, 166].

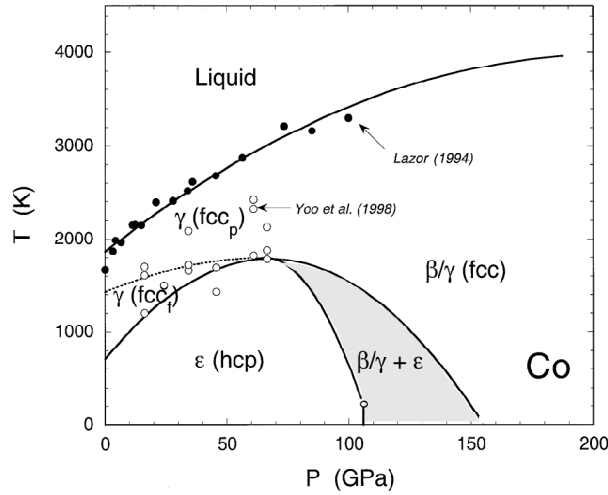


Figure 3.1: The phase diagram of cobalt from ref [61]

This is in contrast to the $4d$ and $5d$ counterparts Rh and Ir, which show nonmagnetic fcc structure. The fact that the hcp structure is more stable than the fcc structure in Co is due to the presence of magnetism, and this has been explained in detail [30]. Among all the elements or ordered compounds, cobalt exhibits a nonzero magnetic moment over the largest P-T domain.

The hcp (ϵ) phase of Co transforms martensitically¹ to the fcc γ -Co structure at high temperatures near 700 K; the mechanism of this transformation has been well described [167–175]. The HT γ -Co structure is ferromagnetic and stable up to the melting temperature which is near 1770 K [231] and results to be quenchable at ambient temperature in a wide pressure range [175]. Fcc Co becomes paramagnetic above the Curie temperature $T_c=1400$ K at ambient pressure and a slight increase of T_c with pressure was reported up to 25 GPa [54].

Under pressure at room temperature, another martensitic hcp-fcc structural phase transition occurs over an extended pressure range, from around 100 GPa to around 150 GPa [61]. The high-pressure fcc phase of cobalt is generally thought to be non magnetic, according to the filling factor of the 3d electronic band [28] (see section 5.37), and favored with respect to the hcp-ferromagnetic phase starting from 80-100 GPa [42, 45, 50–52, 61, 99] (see sections 3.2.2 and 5.2.2).

A new metastable ϵ' d(double)hcp-Co phase was also reported occurring during the quenching of the HT γ -Co below 60 GPa [175]; a similar dhcp structure had previously been observed for Fe at high pressures [75, 76, 176]. This structure is likely stabilized due to the decrease in magnetism and strong spin fluctuations at high temperatures [175].

In the following sections the room temperature-high pressure magnetic and structural properties will be reviewed in more detail as they are more relevant for comparison with the results presented in this Thesis.

3.2.2 High pressure structure

As mentioned above, the hcp structure in Co is retained over a large pressure range ($P \leq 100$ GPa). The equation of state (EOS) of hcp Co has been widely investigated both experimentally [61, 62, 165, 166, 202, 275] and theoretically [43, 49–52, 99].

In 2000 Yoo and co-workers [61] reported the first evidence of a pressure induced hcp-fcc transition in cobalt (Fig. 3.2), characterized by no change in volume and a broad coexistence range (about 100-150 GPa). Such a big interval of co-existence was attributed to the small energy difference between the two phases [175] and to a possible non hydrostaticity of the sample.

Theoretical calculations predict the HP fcc structure, named β -fcc, to become energetically favorite with respect to the hcp around 100 GPa [50–52, 175] in agreement with the observed experimental onset; however also lower values of 70–80 GPa [45] and higher values of 145 GPa [52] have been reported. The calculated volume change is 1-3% [50, 51] and the hcp-fcc structural transition is classified as a first order one [51].

The hcp and fcc structures differ only in their stacking sequence of the planes (Fig. 3.3), so the transition requires relatively small atomic displacements and thus occurs martensit-

¹Cf. 2 at pag.17.

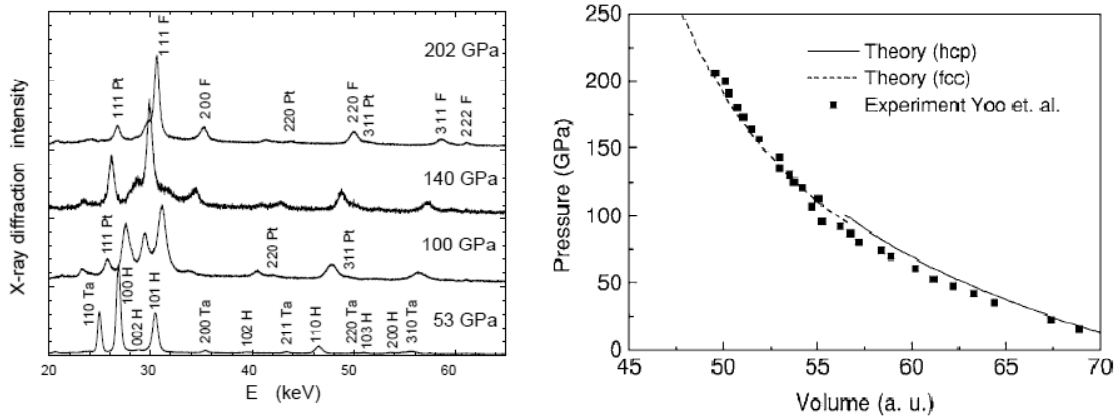


Figure 3.2: left: Energy dispersive x-ray diffraction patterns of cobalt at high pressures from [61], showing a phase transition from hcp Co to fcc Co above 100 GPa. right: experimental [61] and theoretical [50] EOS of hcp and fcc Co.

ically [8,18]. The calculated energy difference between the fcc and hcp phases is less than 4 mRy/atm between 100 and 150 GPa and the bulk modulus and density of the P-induced fcc structure result to be higher compared to hcp-Co.

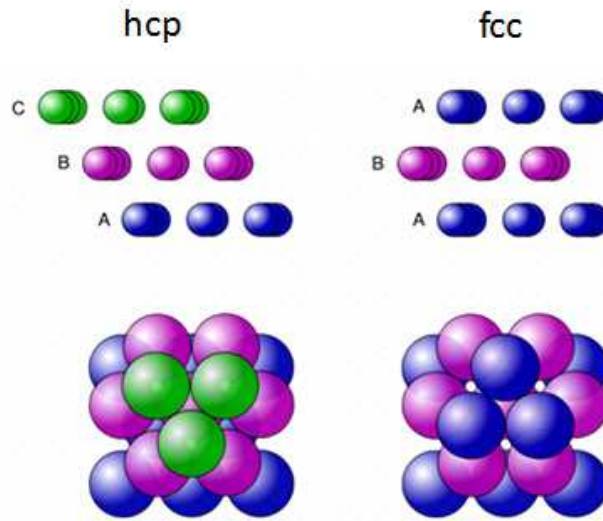


Figure 3.3: hcp and fcc structures.

In the XRD experiment by Yoo and co-workers the c/a ratio of the hcp phase is equal to 1.615 up to 80 GPa; at higher pressure it increases rather continuously, reaching the ideal value 1.63 at 110 GPa and 1.65 at 150 GPa, clearly suggesting a deviation from a close packed structure. This is in contrast to theory which predicts the c/a ratio to remain close to 1.62 up to 200 GPa [99, 175]. Interestingly another XRD work by Antonangeli and co-workers reports an inversion in the pressure evolution of the axial c/a ratio of the

hcp phase around 75 GPa [166] (Fig. 3.4), at the same pressure at which anomalies in the elastic and vibrational properties occur (see section 3.2.3). Calculations suggest a magneto-elastic effect as a possible driving factor: compression induces a slow reduction of the magnetic moment up to 70–80 GPa, above which the magnetism is rapidly lost and the axial ratio c/a of ferromagnetic cobalt changes its pressure derivative, coming up to match the c/a values of nonmagnetic cobalt (inset in Fig. 3.4). Similar arguments are invoked to explain elastic anomalies reported in the same pressure range (see section 3.2.3).

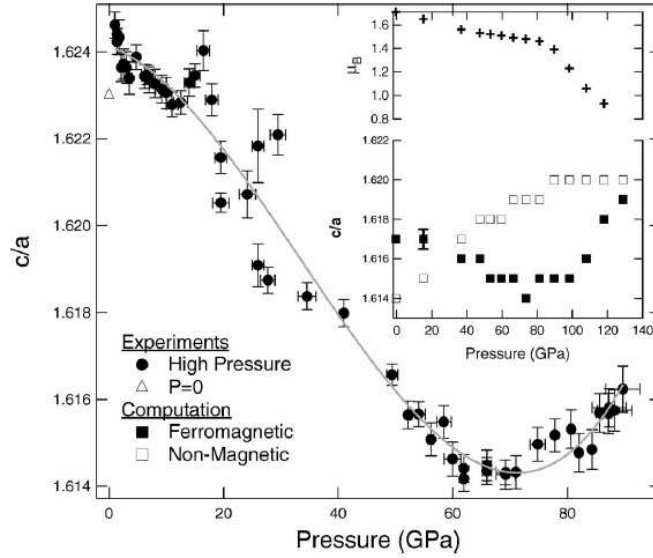


Figure 3.4: Pressure evolution of the axial ratio from [166]. Inset: theoretically predicted pressure evolution of the magnetic moment (crosses) and computed values of magnetic (full squares) and non-magnetic (empty squares) c/a .

3.2.3 Elastic anomalies

The high-pressure phase transition is preceded by an anomalous elastic behavior in the hcp phase. Measurements of the Raman active transverse optical TO phonon mode, which can be related to the shear elastic constant [179, 180], show a change in slope of the E_{2g} mode Gruneisen parameter near 60 GPa [181] (Fig. 3.5 panel b). The measurements of aggregate elastic constants by both impulsive stimulated light scattering (ISLS)[181] and inelastic x-ray scattering [182] show an even more anomalous behavior, with the shear modulus softening in the range of 70–100 GPa. This is best seen in deviations from an expected linear density dependence of longitudinal (v_L) and transverse (v_T) acoustic velocities with a sublinear relation and even softening in v_L and v_T (Fig. 3.5 panel a).

Calculations [50, 52] demonstrate that all these elastic anomalies coincide with the onset of the loss of ferromagnetism in the hcp Co phase (see next section), thus suggesting a magneto-elastic coupling between acoustic phonons and spin wave branches (magnons)

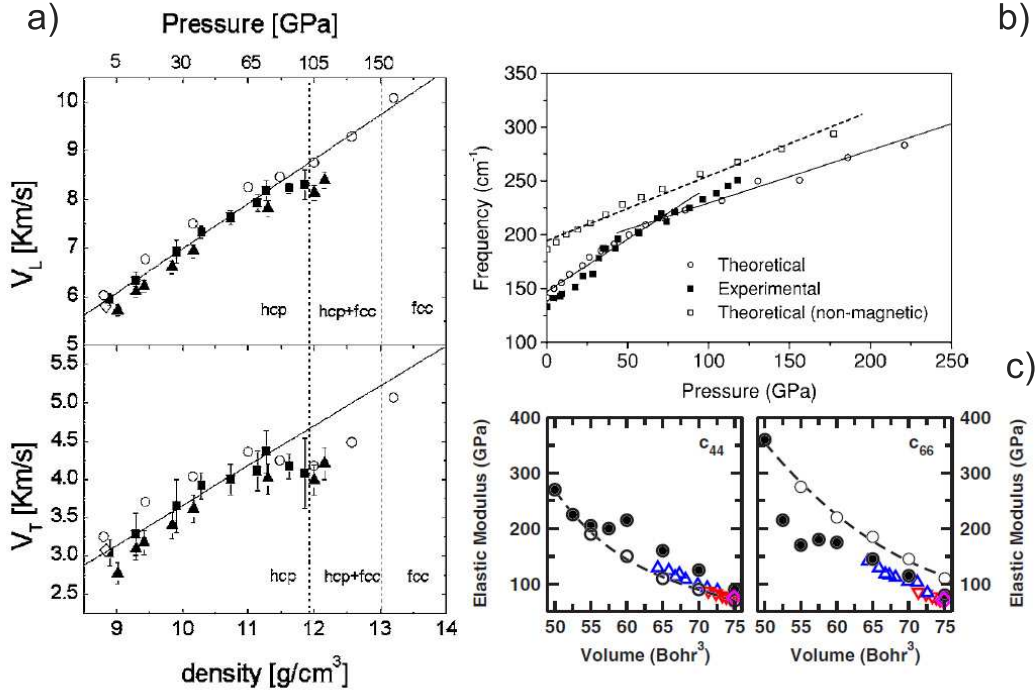


Figure 3.5: Co elastic anomalies. a) Aggregate compressional (upper panel) and shear (lower panel) sound velocity of polycrystalline hcp cobalt as a function of density from [182]. IXS results (full squares) [182]; ambient pressure ultrasonic results [183] (open diamond); ab initio calculations [52] (open circles); ISLS measurements [181] (solid triangles). The limits of the phase stability [61] are indicated by dashed lines. b) E_{2g} phonon frequency as a function of pressure: theory and experiment [50, 181]. Open squares are for nonmagnetic hcp-Co. c) Single crystal elastic constants of hcp cobalt. Filled circles show the results from the magnetic computations and open circles from the nonmagnetic computations. Experimental results for single crystal elasticity are included for ultrasonic measurements at ambient pressure (purple diamonds) [183]; inelastic x-ray scattering (blue up triangles) [182]; and impulsive stimulated light scattering (red down triangles) [181].

[184, 185] as the driving factor.

3.2.4 High pressure magnetism

Several calculations in the literature, mainly based on the density functional theory (DFT), describe the magnetic behavior of both compressed hcp and fcc Co phases [43, 45, 50–52, 99, 175]. The calculated magnetic moment of both the hcp and fcc phases decreases with increasing pressure. This is qualitatively understood in the framework of the Stoner–Wolffahrt model: compression leads to the broadening of the bands contributing to a lower density of states at the Fermi level such that the magnetic state stability condition given by the Stoner criterion is no longer met.

There is a general agreement on the qualitative trend of the moments suppression and

on the fact that the fcc structure should loose its magnetic moment at lower compression respect to the hcp, although there is some incertitude in the values of the critical pressure for magnetization extinction for both phases. The initial slow and virtually linear decay in both phases up to 60–80 GPa is followed by a more rapid decrease until total suppression at 80–120 and 140–180 GPa for the fcc and hcp phase respectively, as sketched in Fig. 3.6. Only two theoretical studies in the literature report very different results: in Yoo et al. (1998) [175] the situation for the two phases is reversed as hcp-Co loses its magnetism at 60–110 GPa before fcc-Co (60–160 GPa); GGA+U² calculations by Mohamed and co-workers [43] show both hcp and fcc phases to be still ferromagnetic at 200 GPa. However, this kind of calculations are likely unreliable as the pressure evolution of the U parameter is unknown; in fact other important discrepancies were reported by the authors with respect to experiments when the GGA+U approach was used.

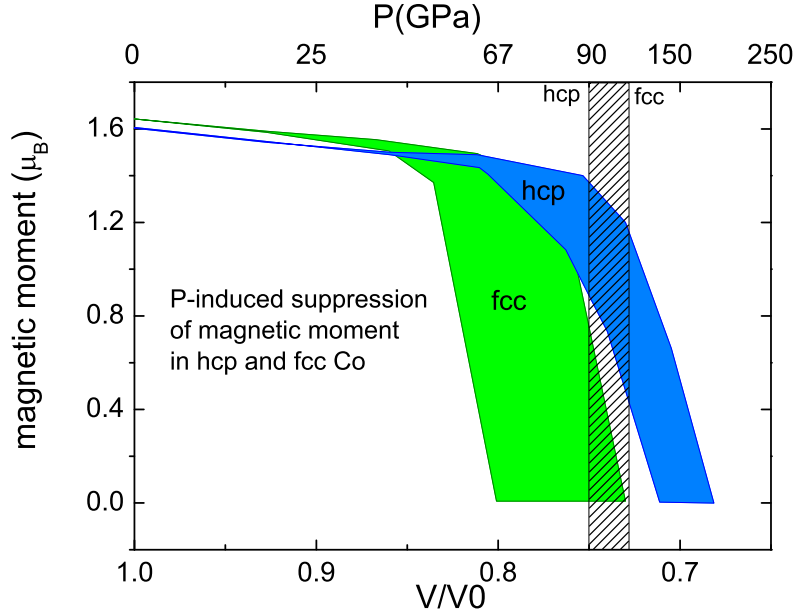


Figure 3.6: Pressure evolution of the magnetic moment for fcc-Co (green) and hcp-Co (blu) taken for refs. [43, 45, 50–52, 166] and pressure interval where the hcp-fcc transition is commonly reported [50, 51, 175](dashed area).

In the calculations, the hcp-fcc structural transition is placed in correspondence with the loss of magnetic moment of the fcc phase [45, 51] or around 20 GPa afterwards [50, 52]. In both cases the pressure-induced fcc structure in cobalt is expected to be non-magnetic. It should be noted that all the above mentioned DFT calculations do not include thermal contributions to the free energy, therefore the resulting predictions represent the 0K phase stability of Co.

Experimentally, the high pressure magnetism of cobalt was firstly probed by two K-

²Ab initio calculations based on the density functional theory (DFT) in which the generalized gradient approximation (GGA) is used with an additional Hubbard-U term for the treatment of strong on-site 3d electron-electron interactions.

edge XMCD systematic studies on the 3d metals by Ishimatsu and co-workers [63] and Iota and co-workers [42] in 2007 respectively reaching 39 and 100 GPa. In these studies a continuous linear decrease of the XMCD signal was observed but the total suppression of ferromagnetic order was not reached. Basing on the measured reduction of the XMCD signal, the total disappearance of the magnetic moment in Co was estimated to occur around 150 GPa, i.e. at the end of the structural hcp-fcc transition. During the time of this Thesis, Ishimatsu and co-workers have extended the pressure range of investigation up to 170 GPa [65] (Fig. 3.7). From the observed spectral changes in both XANES and XMCD they are able to distinguish three pressure regions: an hcp phase stability range (0-80 GPa), the hcp-fcc coexistence interval (80-130 GPa) and the fcc phase region after the transition is completed (130-170 GPa). The difference in the onset and width of the structural transition is attributed to the non-hydrostatic conditions. The K-edge XMCD signal is again seen to decrease linearly from its ambient value, presenting a small discontinuity in correspondence with the onset of the hcp-fcc transition at 80 GPa but a residual non-zero signal (around 10% of the initial value) remains after 130 GPa up to the maximum pressure of 170 GPa (Fig. 3.7 panel b). This is in contrast with all the above mentioned theoretical prediction of a non-magnetic HP fcc structure. Basing on field depended measurement (Fig. 3.7 panel c), the authors suggest the existence of an HP paramagnetic fcc phase with anomalously large susceptibility.

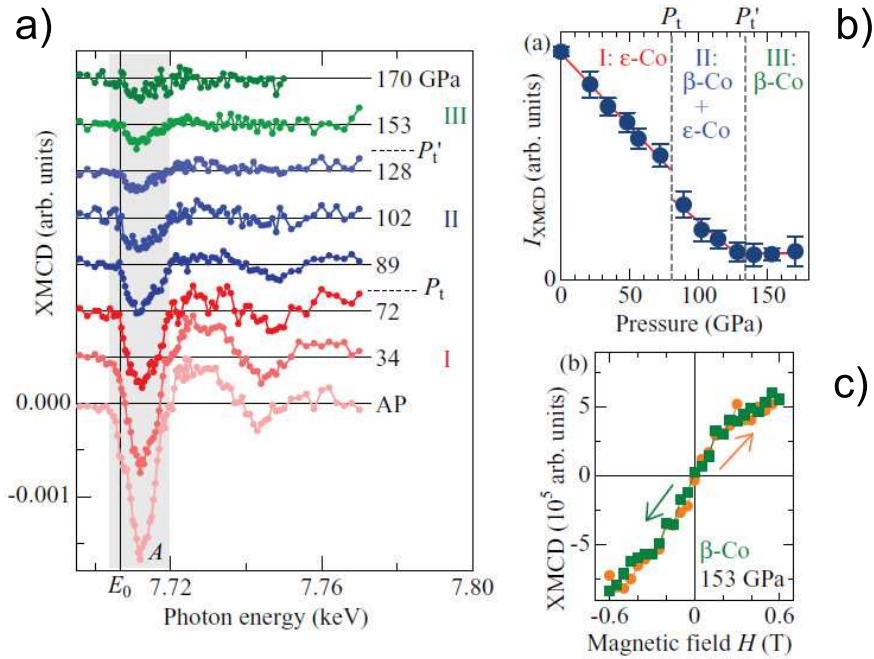


Figure 3.7: a) K-edge XMCD measurements in cobalt up to 170 GPa from [65]; b) XMCD integral as a function of pressure [65], c) magnetic field dependence of the XMCD amplitude at 152 GPa [65]

The trend reported for the K-edge XMCD signal under pressure in the three exper-

iments is in contrast with spin magnetization theoretical predictions as the calculations show an initial small pressure dependence of the moment followed by a more rapid decrease (for both phases), whereas XMCD data show a linear decrease over the whole pressure range. The behavior of the XMCD signal is also in disagreement with observed increase in the Curie temperature at low pressure [54]. We have found an analogous trend in our data; the possible reasons for this discrepancy are given in the results and discussion section.

3.3 Experiment

We have performed two high-pressure room-temperature XANES/XMCD experiments at the Co K-edge ($E_0=7709$ eV) on the beamlines ODE (Soleil) and ID24 (ESRF) [94, 186]. Beam focus sizes were 25×35 and $5 \times 5 \mu\text{m}^2$ FWHM respectively at the sample position. The pressure range covered was up to 94 GPa on ODE and up to 120 GPa on ID24. Non-magnetic Be-Cu membrane diamond anvil cells (DAC) of the Chervin design [107] were used with single bevel diamond anvils with $100 \mu\text{m}$ culets. A rhenium gasket (preindented from $200 \mu\text{m}$ to around $15 \mu\text{m}$ thickness) was loaded with the Co sample ($4 \mu\text{m}$ thick high-purity foil 99.9998% from Goodfellow Ltd) and a ruby chip. Argon and silicone oil were used as pressure-transmitting media for the ODE and ID24 experiments respectively. Consistent XANES and XMCD results have been obtained in the two experiments, suggesting that the different degree of hydrostaticity did not significantly affect our measurements. The pressure was measured by the ruby fluorescence technique [187], but as the ruby signal was lost above 80 GPa on ID24 the pressure was also determined by the change in interatomic distances measured by EXAFS (Extended X-ray Absorption Fine Structure)[88]. Pressure values obtained using the two methods (EXAFS and ruby) for $P < 80$ GPa were found to be consistent. The co-existence of hcp and fcc Co above 80 GPa (see section 3.4) is responsible for larger errors in the pressure determination. Compressibility values of the two phases, taken from [61, 62], were used to correlate changes in interatomic distance with changes in pressure. Our XMCD measurements were performed using a 0.7 T magnet on ID24 and a 1.3 T magnet on ODE. Both fields gave rise to the same normalized intensity of the XMCD signal on Co foil at ambient conditions (-0.002), directly proving that a magnetic field of 0.7 T is sufficient to saturate the sample. Moreover the measured XMCD signal intensity is the same as that reported in the literature for similar foils reaching saturation [42, 188].

3.4 Results and discussion

Fig. 4.5 shows the combined XANES and XMCD data recorded on ID24. The absorption energy range is limited to the XANES and first EXAFS oscillation. Three features (labeled A, B-B', and C) can be identified. Upon compression, we observe a continuous increase in the intensity of feature A at $E=4$ eV from the edge (energy of the "dipole forbidden"

$1s$ - $3d$ quadrupole transition). This phenomenon has been reported [42, 63, 193] for all the 3d metals at high pressure and has been ascribed to an increase in the p -character of the d-bands, which adds "dipole allowed" intensity to this transition. Pressure indeed favors $3d$ - $4p$ overlap (hybridization), as the 3d bands widen and the $3d$ electrons become more delocalized.

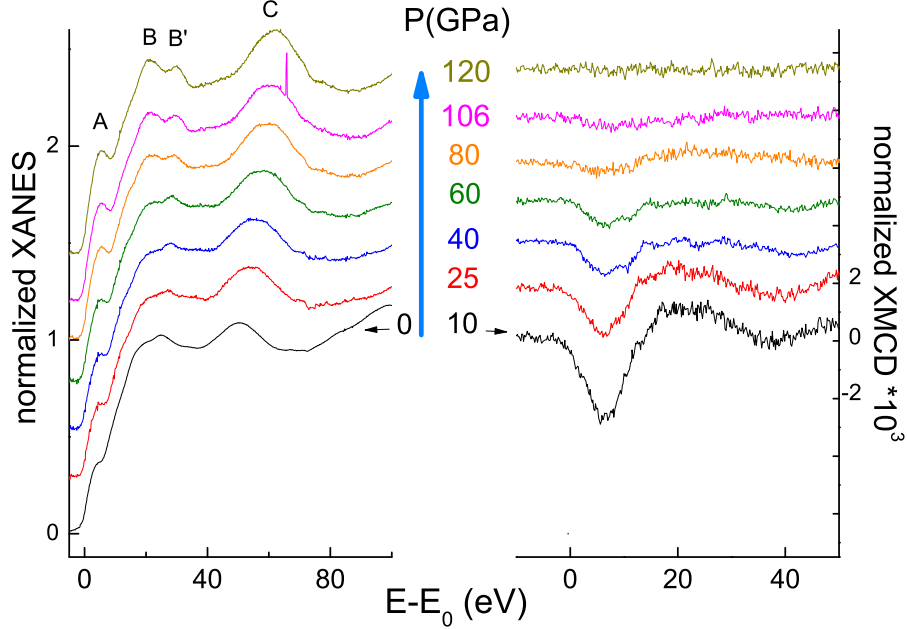


Figure 3.8: Normalized K-edge XANES (left) and XMCD (right) spectra of cobalt as a function of pressure (ID24).

The double peak feature B B' (19 and 24 eV from the edge) changes shape under compression: the two peaks (B and B') become more defined and their relative height is inverted above 80 GPa. A similar profile of the B' and B features is observed in fcc Fe-Ni alloys and pure fcc nickel XANES. Finally the intense peak C, at $E = 50$ eV after the edge, becomes sharper and more pronounced and shifts to higher energies with pressure. The overall shift of the spectra towards higher energies is a typical effect of compression [42, 63, 193] and is proportional to energy, i.e. the higher the energy position (with respect to the edge E_0) the bigger the energy shift due to pressure (see next section) [65].

XANES Data treatment

The raw absorption spectra were corrected subtracting a pre-edge linear background and normalized to the jump edge discontinuity using the program *Athena* (IFEFFIT package [190, 191]). The above mentioned P-induced energy shift of the spectra results to be approximately linear with energy: $\Delta E \approx c \cdot E$ (see the Nickel chapter for an accurate discussion and [65]). Therefore re-plotting the spectra at each pressure as a function of the abscissa $(E - E_0)/E_C$ (where E_C is the energy position of feature C whose energy

shift movement can be clearly detected) allows to minimize the influence of the lattice contraction and consequently to better detect subtle changes in the XANES due to pressure application. This is represented in Fig. 3.9. From the zooms of features A, B B' and C (insets of figure 3.9) the pressure variation of the XANES spectra can be divided in (at least) two regions: $P < 80$ and $P > 80$ GPa suggesting $P \approx 80$ as the pressure onset of a local structural transition. This is also seen in the pressure evolution of the XANES integrals (integration up to half of peak C): the integrals show a constant value within the error up to 40 GPa followed by a jump of 4% at 80 GPa. Above 80 GPa, the XANES integrals increase continuously, a hint that the transition is not complete at 120 GPa.

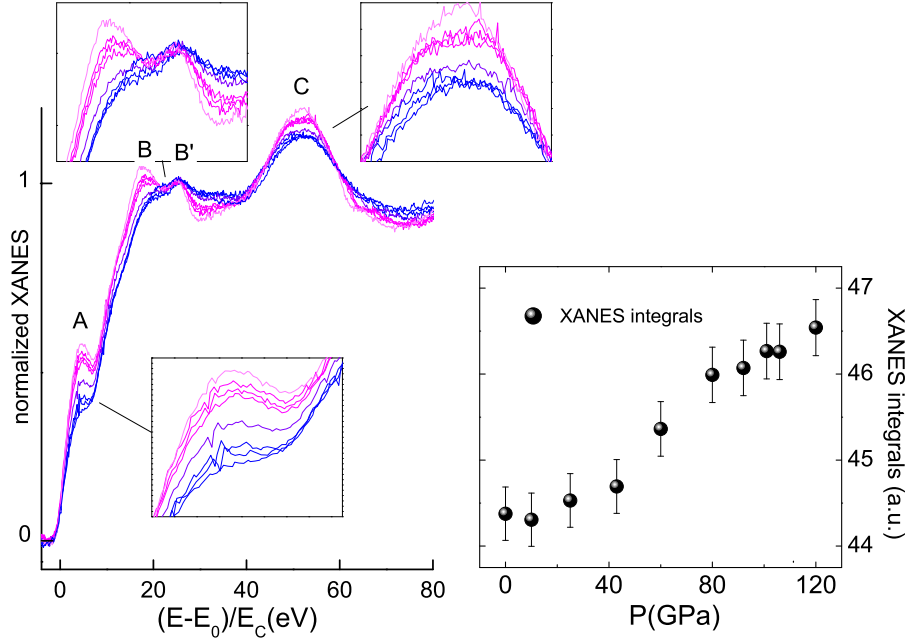


Figure 3.9: left: normalized K-edge XANES spectra of cobalt plotted as functions of $(E - E_0)/E_C$. right: XANES integrals evolution under pressure

A very similar behavior is reported in an analogous work by Ishimatsu and co-workers [65]. In that work the authors are also able to detect another variation in the XANES spectra occurring at 130 GPa, after which pressure the XANES feature remains stable up to 170 GPa. The authors interpret the three pressure regions as corresponding to the hcp-Co structure stability range, the hcp-fcc coexistence region and the fcc structure stability range after the transition is completed. In our data a second variation is observed in the zooms of features B B' and C at the pressure of 120 GPa but less significantly in feature A and in the XANES integral evolution.

FEFF simulations

In order to interpret the evolution of the data with pressure, XANES simulations using the FEFF8 package [194] were performed (Fig. 4.9). The atomic Co clusters were built

using the crystallographic parameters of compressed hcp and fcc phases found in [61, 166]. Simulations show that main differences in the XANES corresponding to the two phases are visible close to the edge (peaks B and B') and arise mainly from the changes in the atomic arrangement within the first 5 Å from the absorber (i.e. within the first four shells in the fcc phase).

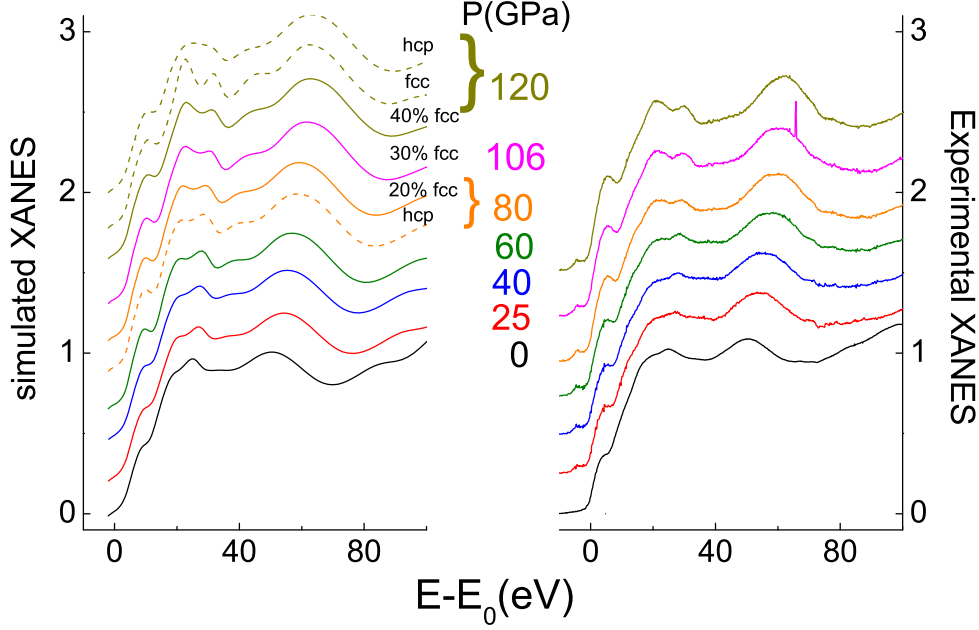
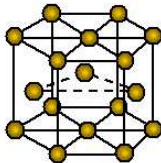
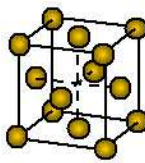
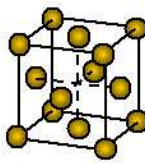


Figure 3.10: Simulations of XANES spectra using the FEFF code [194] (left) and comparison with experimental XANES spectra (right). The atomic clusters for Co are built using the crystallographic parameters of the structurally distorted hcp and fcc phases found in [61, 166]. The solid lines are models of our XANES data while the dashed lines show the spectra expected for pure hcp or fcc phases. Above 80 GPa some combined hcp and fcc character is observed in our data.

The trend in the experimental XANES data (Fig. 4.5) can be well reproduced using a pure hcp phase up to about 60 GPa. In this region better profiles are obtained using a and c parameters from Antonangeli *et al.* [166]. Our data thus confirm the initial decreasing behavior of the c/a ratio which was not detected in the XRD work by Yoo *et al.* [61]. Starting from 80 GPa the XANES data are better reproduced assuming the presence of a small fraction of fcc atomic configurations. We estimate that at 120 GPa the fcc phase fraction is at least 40%. This is in agreement with the hcp-fcc coexistence pressure range found in XRD measurements [61]. As illustrated by the top spectrum in Fig. 4.9, attempts to reproduce the 120 GPa spectrum with a pure hcp structure are definitively unsatisfactory. Nonetheless, a precise evaluation of the fcc/hcp phase fraction cannot be performed as the intensities of the simulated XANES features depend on the simulation parameters. The pressure onset for the detection of this phase transition is slightly lower compared to the X-ray diffraction (XRD) investigation of [61], where the onset of the

transition was found to occur near 92 GPa ([61]-inset of Fig. 2). This difference is not surprising because the presence of randomly distributed small ($<10\text{\AA}$) fcc-like Co clusters would be invisible to XRD.

These local transformations can be at least qualitatively related to the observed variations of the c/a axial ratio [61, 166] and to the anomalies in the elastic moduli [52, 182] reported in literature around 80 GPa and the hcp-fcc phase transition can be schematized, from the local structure point of view, as a progressive symmetrization process. In the following discussion, for sake of simplicity, we will refer to ambient local structure configurations. Ambient hcp-Co is generally characterized by a "non-ideal" axial ratio value $c/a \approx 1.62$ [61, 165, 166]. In this configuration an atom placed in the origin is surrounded by 6 shells of atoms within the first 5 Å as reported in Table 3.4 first column. As soon as the c/a ratio increases up to the ideal value 1.63, as reported after 80 GPa [61, 166], a symmetrization of the 1st and 4th shells occurs (Table 3.4 second column). The transition to fcc results into a further symmetrization of the local structure i.e. a reduction to 4 shells in the first 5 Å (Table 3.4, third column). This last step implies the slipping of the basal plane, favored by the softening of the elastic shear modulus C_{44} ([52, 182], see section 3.2.3), which controls the shear strain in the basal plane. This is analogous to the temperature-driven martensitic hcp-to-fcc transition which is triggered by 27% softening of C_{44} [174].

	non ideal-hcp $c/a \approx 1.62$			ideal hcp $c/a = 1.63$			fcc		
shell	distance (Å)	N	distance (Å)	N	distance (Å)	N			
1	2.49	6	2.5	12	2.50	12			
	2.50	6							
2	3.54	6	3.54	6	3.54	6			
3	4.07	2	4.07	2	4.34	24			
4	4.34	12	4.33	18	5.1	12			
	4.35	6							
5	4.79	12	4.78	12					
6	5.02	6	5.0	6					

Table 3.1: Ambient local structure configurations for ideal-hcp, hcp and fcc symmetries within the first 5 Å.

XMCD measurements

The rough XMCD data were normalized to the absorption edge step and the instrumental background was subtracted using a second or third order spline. For the XMCD data it is

not strictly necessary to re-plot the data versus the abscissa $(E - E_0)/E_C$ as compression does not affect the edge region in terms of energy shift. The right panel of Fig. 4.5 presents the XMCD normalized spectra obtained on ID24. The XMCD spectrum consists of a main negative peak (7 eV) followed by a large positive structure (17-24 eV). According to multiple scattering calculations the main negative structure in the Co XMCD spectrum results from the photoelectron scattering by the spin-orbit potential in d and p shells of the neighboring Co atoms [141].

In Fig. 3.11, we represent the integral of the absolute value of the XMCD signal, calculated in the energy interval corresponding to the main negative peak, versus pressure. The error in the XMCD integral has been evaluated taking into account the area of noise and some possible errors coming from the background subtraction. Our data are in good agreement, within the error bars, with the linear decay observed in refs [42, 63, 65] even though our error bar does not allow to distinguish the small jump at 80 GPa pointed out by [65] in correspondence with the onset of the hcp-fcc local structural transformation and elastic anomalies. However a slight inflection of the data trend is observed after $P=80$ GPa. Most importantly, we report the total extinction of the signal at 120 ± 10 GPa. Indeed the collapse of ferromagnetism does not seem to coincide with the complete hcp-fcc structural transformation at 150 GPa [61], as previously suggested [42], but to occur at an earlier stage. However a precise determination of the high pressure phase in cobalt, corresponding to a zero XMCD signal, would require a combined XAS-XRD experiment.

On the basis of the present results we point out that the pressure evolution of magnetism and structure in Co reveals major differences with respect to the Fe case. In the latter, ferromagnetism is almost not affected by compression until its abrupt suppression at the bcc-hcp phase transition [42, 63, 93]. In the former, compression has an immediate effect on ferromagnetism, causing a continuous strong linear decay until total suppression at 120 GPa. Moreover, the structural changes observed at 80 GPa seem not to importantly affect the HP Co magnetism. In fact, even if the small jump detected by Ishimatsu and co-workers is considered, this represents a little variation compared to the intense and early decrease of the XMCD signal starting before the transition.

Our results do not agree with the latest from Ishimatsu and co-workers [65] in which a residual XMCD signal is reported up to 170 GPa (Fig. 3.11). On the basis of field dependent XMCD measurements (Fig. 3.7), the authors of ref. [65] support the existence of a paramagnetic state with an anomalously large susceptibility. The detection of a paramagnetic state is quite surprising as the maximum field applied was 0.6 Tesla, and the temperature of measurement was not reported (so we assume it was room temperature). Indeed the measurement of a paramagnetic phase by means of XMCD generally requires very high fields (≈ 7 Tesla) and low temperatures (≈ 20 K) [201].

However, such a different result stimulates further experimental work especially aimed at the coupling of high pressure - low temperature conditions allowing to disentangle the moment suppression from Curie temperature effects. We are currently working on the

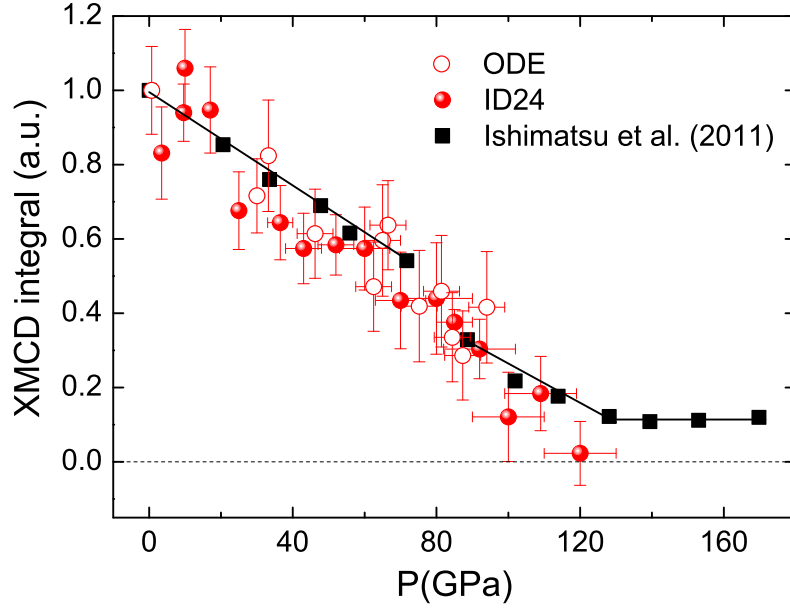


Figure 3.11: Integral of the K-edge XMCD signal of Co in arbitrary units (red full and empty circles) and comparison with data from [65] (full black squares).

improvement of our setup on beamline ID24 in order to realize this kind of experiments.

DTF Calculations

Density functional calculations (DFT) have been performed by our collaborator Dr. E. Pugh from the University of Cambridge to model the pressure dependence of the spin magnetic moment of hcp and fcc structures of Co. Self-consistent local spin-density approximation calculations were performed using the linear muffin tin orbital method [195–197]. The 4s and 3d electrons were treated as valence electrons and all others included in the core. The fcc and hcp calculations were performed on a mesh of 897 and 819 k-points respectively in the irreducible wedge of the Brillouin zone. Their pressure dependence has been modeled using a semi-empirical method utilizing the Birch equation [198] and the experimental data for both the hcp and fcc phases from reference [61]. The resulting pressure dependence of the spin magnetic moment is shown in Fig. 3.12. The ambient pressure spin magnetic moment from these calculations of $1.59\mu_b$ is in quite good agreement with the experimental value of $1.58\mu_b$ [199].

The calculated magnetic moment of both the hcp and fcc phases decreases with increasing pressure. The initial slow and linear decay in both phases is followed by a more rapid decrease until total suppression at 140 and 90 GPa for the hcp and fcc phase respectively. This predictions fall in the range indicated by previous calculations [45, 50–52, 99] (see Fig. 3.6).

In Fig. 3.12 we compare the DTF calculations to a linear fit of our XMCD data rescaled to the ambient Co spin moment. It is important to note that the DFT calculations

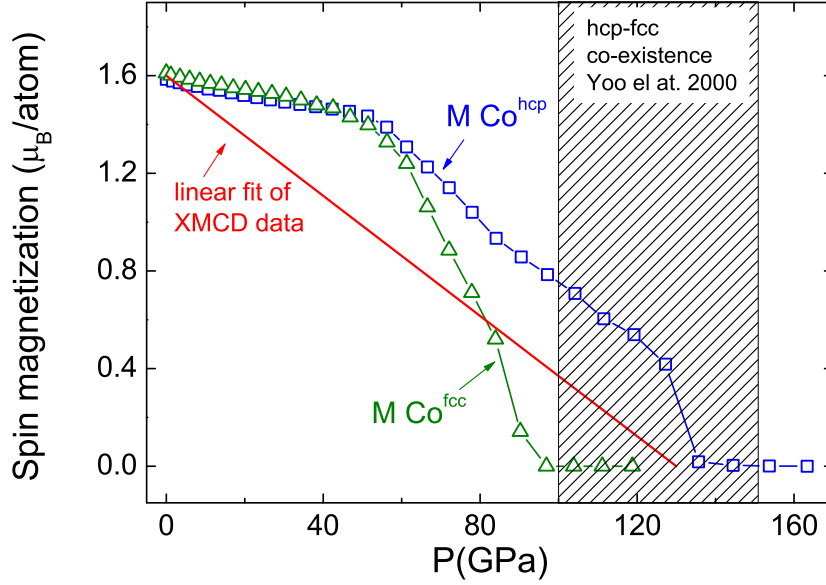


Figure 3.12: Theoretical calculations of the evolution of the spin magnetic moment of hcp and fcc cobalt with pressure. The red line represent a linear fit of the XMCD data rescaled to Co ambient pressure spin magnetic moment. In dashed the hcp-fcc co-existence region indicated by XRD [61].

compute the magnetic moment at 0K conditions whereas our XMCD experiments are performed at ambient temperature and probe ferromagnetism (ferromagnetic order). To the best of our knowledge no estimations of the Curie temperature pressure dependence in cobalt are available above 25 GPa [54]; therefore, Curie temperature effects, disrupting the ferromagnetic order, cannot in principle be excluded. Also, the calculations are for either pure hcp or pure fcc phases while our data show that above ≈ 80 GPa we enter a mixed hcp/fcc state which has not been modeled by DFT and may be complex in nature [200]. The total extinction of the XMCD signal occurs in a region (120 ± 10 GPa) where theory predicts that the fcc structure is non-magnetic and the hcp structure is about to loose its magnetic moment (135 GPa). If pressure errors are taken into account, this suggest that the HP mixed hcp-fcc phase after 120 GPa is actually non-magnetic. Again, we highlight important differences with respect to Fe. In the latter, the hcp phase into which Fe transforms is predicted to be non-magnetic long before the phase transition; in Co, the fcc phase into which Co transforms, loses its magnetic moment close to the phase transition pressure [42, 50, 51, 61, 99] (Fig. 3.12).

The main difference between the calculations and the XMCD measurements is that for both hcp and fcc states the calculations show an initial small pressure dependence of the moment followed by a more rapid decrease, whereas our XMCD data show a linear continuous decrease over the whole pressure range within the error bar until complete suppression. We can invoke two possible reasons to account for the observed disagreement between experiment and theory:

1. the occurrence of Curie temperature effects (T_c becoming comparable or lower to room temperature below 80 GPa);
2. an inadequacy of this type of calculations: the presumed proportionality of the K-XMCD signal integral with the total spin moment, as suggested by multiple scattering studies [135, 139, 140] (see sec. 2.2.3) may not apply and the proportionality to the orbital p -projected moment should be checked, as we showed in the nickel case. Indeed in Ni, the decay of the K-edge XMCD signal integral, induced by compression, closely follows that of the calculated p -projected orbital moment (see the Nickel chapter).

3.5 Conclusions

New XMCD and XANES measurements coupled to FEFF and DFT calculations give a complete description of the structural and magnetic Co phase transition which had not been done before, highlighting major differences with the Fe case. A continuous reduction of the XMCD intensity is observed until complete suppression at 120 ± 10 GPa, providing the first experimental evidence of pressure induced extinction of ferromagnetism in Co. In parallel we document a progressive change in the arrangement of the first atomic shells from an hcp- to an fcc-like local structure starting from $P \approx 80$ GPa, providing a coherent scenario which correlates well with elastic [52, 182] and structural [166] anomalies reported in the same pressure range. The magnetic response in Co seems to be uniquely affected by compression and not by structural modifications. Our combined experimental and theoretical results support the total disappearance of spin magnetization (local magnetic moment) in the mixed hcp/fcc phase around 120 ± 10 GPa. Nevertheless the different behaviors in the pressure evolution of the theoretical spin magnetization and XMCD signal decay, observed prior to the structural phase transition, stimulate further theoretical work. The present results thus represent a severe benchmark for theoretical models addressing the description of extreme condition physics in the 3d metals. Moreover the disagreement found with most recent analogous K-edge XMCD results [65], suggesting the existence of a HP paramagnetic state above 130 GPa, claims for further experimental work aimed at the coupling of HP and HT conditions.

The present results are published in PRB rapid communication [64].

Nickel

The structural stability of fcc Ni over a very large pressure range offers a unique opportunity to experimentally investigate how magnetism is modified by simple compression. In this chapter we present high pressure K-edge XANES-XMCD measurements coupled to XRD measurements on pure Nickel up to 200 GPa. Our data show that fcc Ni is structurally stable and ferromagnetic up to 200 GPa in contrast to the recent prediction of an abrupt transition to a paramagnetic state at 160 GPa. Moreover, novel DFT calculations allow to get an insight into the different behavior of orbital and spin moments in compressed Ni, pointing out that the pressure evolution of the Ni K-edge XMCD closely follows that of the p projected orbital moment rather than that of the total spin moment. The disappearance of magnetism in Ni is predicted to occur above 400 GPa.

4.1 Introduction

As cobalt, nickel plays an important role in understanding the physics and chemistry of Earth's interior, due to the analogies in properties with iron, which is assumed to be an essential constituent of the Earth's core. Beside this, nickel has its own geophysical importance as possible minor constituent of the Earth's core: according to Liu [202] nickel should be the third (4.68 w.%) and the second (5.14 w.%) most abundant element in the inner and outer core, respectively. Moreover nickel has great importance in many materials like Ni-based superalloys.

The fundamental interest in nickel stems from its simplicity. As discussed in the previous chapters, in iron and cobalt the collapse of ferromagnetism with pressure is related to a structural phase transition: the bcc-hcp around 13 GPa ([93] among others) and the hcp-fcc at ≈ 120 GPa [64] respectively. The pressure limit of ferromagnetism in Ni is still not established, and the fcc structure is stable in a very large P-T interval. In fact, neither pressure nor temperature induced structural transitions have been ever reported in the so far explored P-T range: up to 150 GPa at RT and up to melting temperatures in the 0-110 GPa range. Such a high structural stability offers a unique opportunity to

investigate how the simple compression of the interatomic distance influences the magnetic properties.

4.2 Extreme conditions structure and magnetism in nickel

4.2.1 The HP/HT phase diagram

At ambient conditions Nickel crystallizes into a ferromagnetic fcc structure. At room temperature the fcc symmetry is retained up to at least 150 GPa as seen by diffraction [62]. Theoretical calculations agree on the high pressure stability of the fcc phase in the 10^2 GPa range [43, 45] and according to McMahan and Alberts fcc Ni should be still stable at 34 TPa [35]. At high temperature the fcc phase is preserved up to the melting in the 0-110 GPa range [54, 203]. The Curie temperature (T_c) of Ni is 631 K at ambient pressure [37, 53]. Permeability measurements show that T_c increases up to 15 GPa with some tendency to saturation [37, 53].

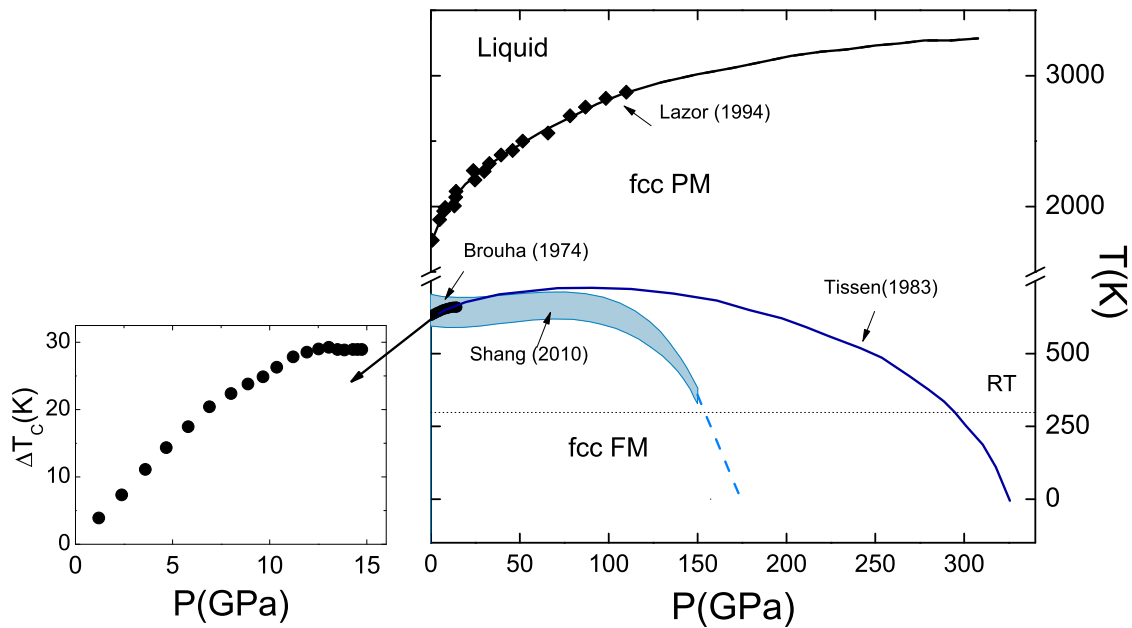


Figure 4.1: Right: the phase diagram of Nickel from refs [37, 53, 54, 60]. Left: zoom of permeability data from [53].

A very recent work based on first-principles calculations and partition function approach [60] predicts T_c to start decreasing sharply around 120 GPa and reaching ambient temperature around 160 GPa, in disagreement with previous estimations by Tissen who calculated that T_c reaches the ambient value around 300 GPa [59].

4.2.2 High pressure magnetism

All the available calculations agree in predicting a stable ferromagnetic fcc phase in nickel up to the 10^2 GPa range [43–45] with the spin magnetic moment slowly decreasing from the ambient value $0.6 \mu_B/\text{atom}$ to $0.48 \mu_B/\text{atom}$ around 300 GPa [45]. When strong correlations are included, within the GGA+U¹ method, the Ni ambient spin magnetic moment increases [43] ($0.65 \mu_B/\text{atom}$), but the rate of pressure induced magnetization decay remains the same. The recent calculations from [43] show that, even though the fcc ferromagnetic phase remains favorite, its total energy becomes very close to that of the non-magnetic fcc phase starting from 170-180 GPa.

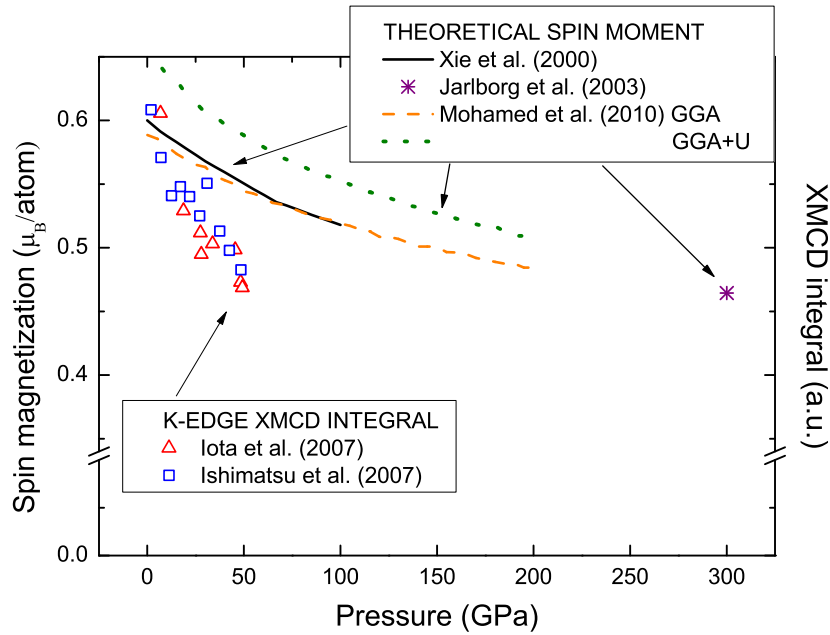


Figure 4.2: Theoretical spin magnetization in nickel as a function of pressure: continuous line is from [44], dash and dot line are from [43] referring to GGA and GGA+U methods respectively, stars are from [45]. In scatter K-edge XMCD data from [42] (red triangles) and [63] (blue squares) rescaled to the nickel ambient spin moment value.

K-edge XMCD has been measured for pure nickel up to 48 [63] and 52 [42] GPa.² Both works show a linear decrease of the K-edge XMCD signal, just like in the case of cobalt but with a smaller rate.

In Fig. 4.2 the evolution of the XMCD integral under compression is compared to that of the calculated spin magnetization. As in the cobalt case, the K-edge XMCD signal decreases much faster than the computed spin moment.

One of the aims of our study has been to shed light on this different behavior and to

¹cf. note 2 in page. 47.

²Actually the work from [42] reports a last point at 70 GPa, but as the XMCD shape is very distorted, this point is likely unreliable. In fact the XMCD integral at 70 GPa results to be very small (0.3 in scale of μ_B/atom) and out of trend with respect to the lower pressure data.

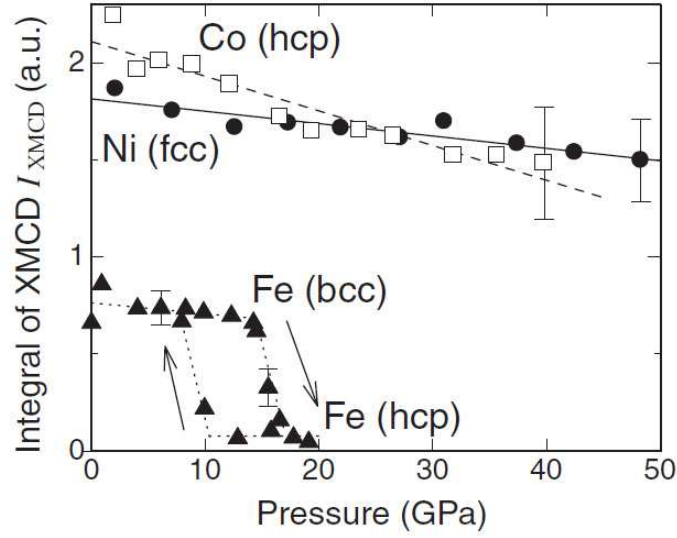


Figure 4.3: Pressure dependence of the K-edge XMCD integral in Fe, Co and Ni from [63]. The rate of XMCD integral linear decrease is lower in Ni (full circles) than in Co (empty squares).

extend the measurements to much higher pressures. Our analysis, based on the comparison with both spin and orbital calculations, points out a proportionality of the K-edge XMCD to the p -projected orbital moment, instead of the spin moment. This will be discussed in the following sections.

4.3 Experiment

High purity polycrystalline Ni powder was charged in an amagnetic Diamond Anvil Cell (DAC) equipped with beveled 75×300 culets diamonds [204]. No pressure transmitting medium was used.

In order to gain stability a slightly modified setup was conceived made up of only essential motors. In particular we eliminated the tilting motors which allowed to rotate the diamond anvil cell with respect to the z and y axis. These rotations are generally used to remove diamonds glitches when present; in this experiment, when necessary, these movements have been performed by hand. This simplified setup allowed us to improve the signal to noise ratio by more than a factor 2 and get rid of instrumental background.

For each pressure the volume compression was measured on beamline ID27 at the European Synchrotron Radiation Facility (ESRF) [205].

As shown in Fig.4.4, the X-ray diffraction measurements showed a stable fcc structure in the whole pressure range studied. The pressure value was then calculated using the compression curve found in Dewaele et al. [62]. XANES and XMCD signals were recorded at the energy dispersive XAS beam line ID24 (ESRF) [93, 186] at the nickel K-edge ($E_0 = 8333$ eV). The XMCD signal is obtained by taking the difference between X-ray

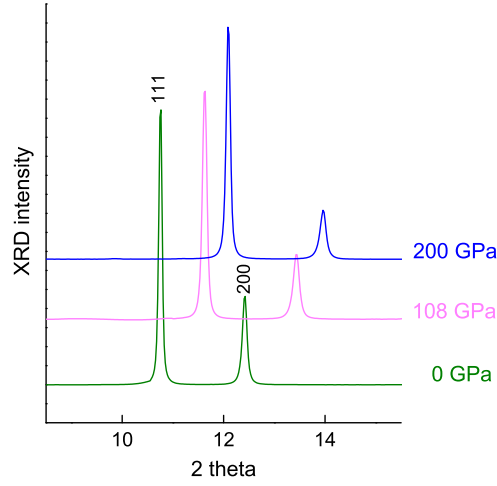


Figure 4.4: Selected XRD patterns of pure Ni up to 200 GPa.

absorption spectra measured using parallel (μ^+) and antiparallel (μ^-) orientations of the sample magnetization relative to the incident photon helicity.

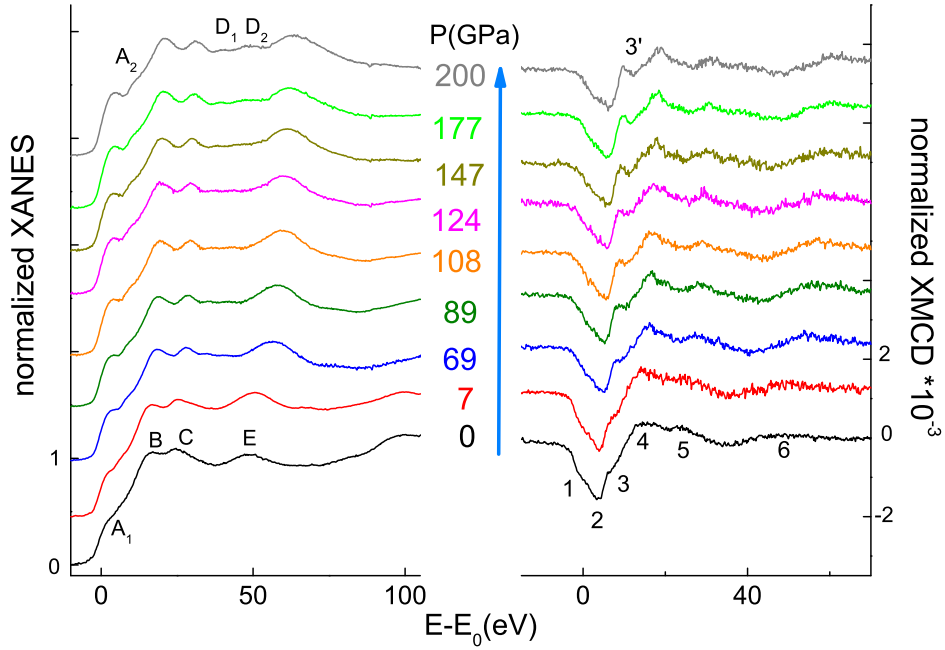


Figure 4.5: Combined XANES (left panel) - XMCD (right panel) spectra in pure Ni up to 200 GPa.

The applied magnetic field was 0.6 Tesla and proved to be sufficient to saturate the sample. The highly focused beam ($5\mu\text{m}$ FWHM) enabled to reach a pressure range so far unexplored by x-ray absorption spectroscopy: ≈ 200 GPa, corresponding to a volume compression of $V/V_0=0.66$, where V_0 is the equilibrium atomic volume. Such a high pressure actually represents a record for magnetic measurements with the exception of Mössbauer techniques [98] whose application is anyway limited to few elements (mainly

Fe compounds). Fig.4.5 reports the normalized XANES (left) and XMCD (right) signals between ambient and 200 GPa.

4.4 Results and discussion

Signal analysis: XANES

Preliminary pre-edge linear background subtraction and edge jump normalization were performed on the raw absorption spectra using the program *Athena* (IFEFFIT package [190, 191]).

In the XANES, the effect of compression reveals mainly in: i) an increase of the pre-peak feature A1, ii) the appearance of a shoulder in the pre-edge region (A2), iii) an inversion of the relative height of peaks B and C and iv) the appearance of two additional peaks (D1, D2) in the post-edge region.

It is well known that the A1 feature in the 3d metals originate from the quadrupolar transitions 1s-3d [207], favored by the 4p mixing into the 3d orbitals which provides some electric dipole allowed 1s-4p character to the transition, adding intensity to the electric quadrupole mechanism [208]. The A1 intensity enhancement under pressure has been already observed [42, 63, 193] in all the 3d metals and interpreted as an increase of 3d-4p band overlap under compression.

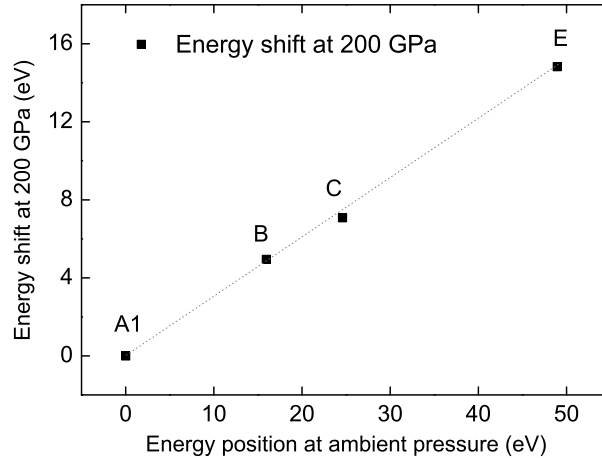


Figure 4.6: Energy shift of features A1, B, C, E at 200 GPa

The energy shift of the whole spectra to higher energies is also commonly observed in Fe, Co, and Ni and can be regarded as a pressure induced effect in the local structure [193].

At each pressure, this shift results to be linearly proportional to the ambient energy position with respect to the edge, i.e. features which are further from the edge are more shifted in energy. In fig 4.6 we plot as an example the energy shift of the features A1, B, C, E at 200 GPa, as a function of their energy position at room pressure. For this

reason re-plotting the spectra, at each pressure, as a function of the abscissa $(E - E_0)/E_i$ (where E_i is the energy position of feature i , generally chosen as the furthest from the edge so that its energy shift can be clearly detected) allows to minimize the influence of the lattice contraction and consequently to better detect subtle changes in the XANES due to pressure application, as we did in the case of cobalt.

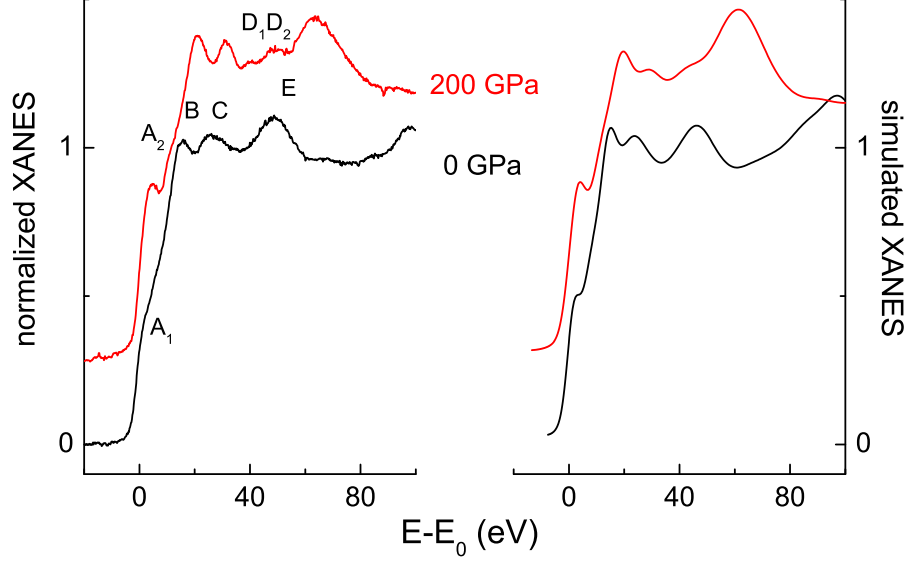


Figure 4.7: left: XANES data at 0 and 200 GPa; right: XANES simulations using the FDMNES code at the same pressures.

Because the XRD measurement proved that the fcc structure is stable in the whole pressure range of our study, the observed XANES modifications must be due the compression of the fcc structure or to the development of local distortions. In order to clarify this, simulations using the FDMNES code [223] were performed using a cluster of 134 atoms, corresponding to a full multiple scattering radius of 7 Å. Simulated spectra were then convoluted with a gaussian function of 3 eV width to reproduce the experimental resolution. To simulate the effect of compression the cell parameter was modified according to the XRD data. The simulations reproduce most of the changes observed in the XANES spectra (Fig.4.7): the enhancement of the A1 feature, the appearance of a new hump around 47 eV corresponding to the D1 and D2 peaks, and the general energy shift. The shape of the double peak B C is not perfectly reproduced even at ambient pressure, however the enhanced intensity of feature B reflects the data trend. This finding support the conclusion that the XANES changes are the effect of the simple compression.

Signal analysis: XMCD

The XMCD spectra, shown in Fig.4.5 right panel, where normalized to the absorption edge step. Thanks to the improved setup no instrumental background subtraction was necessary.

The most remarkable modification in the XMCD evolution with applied pressure is the movement of the inflection point 3 which finally gives rise to a new feature 3'. Meanwhile the main valley 2 loses intensity (-34%) and the post edge peaks (4,5 and 6) becomes sharper.

No sharp signal decay is observed between 120 and 160 GPa. Our results are thus in disagreement with the prediction of an abrupt pressure induced transition to paramagnetic state at 160 GPa [60].

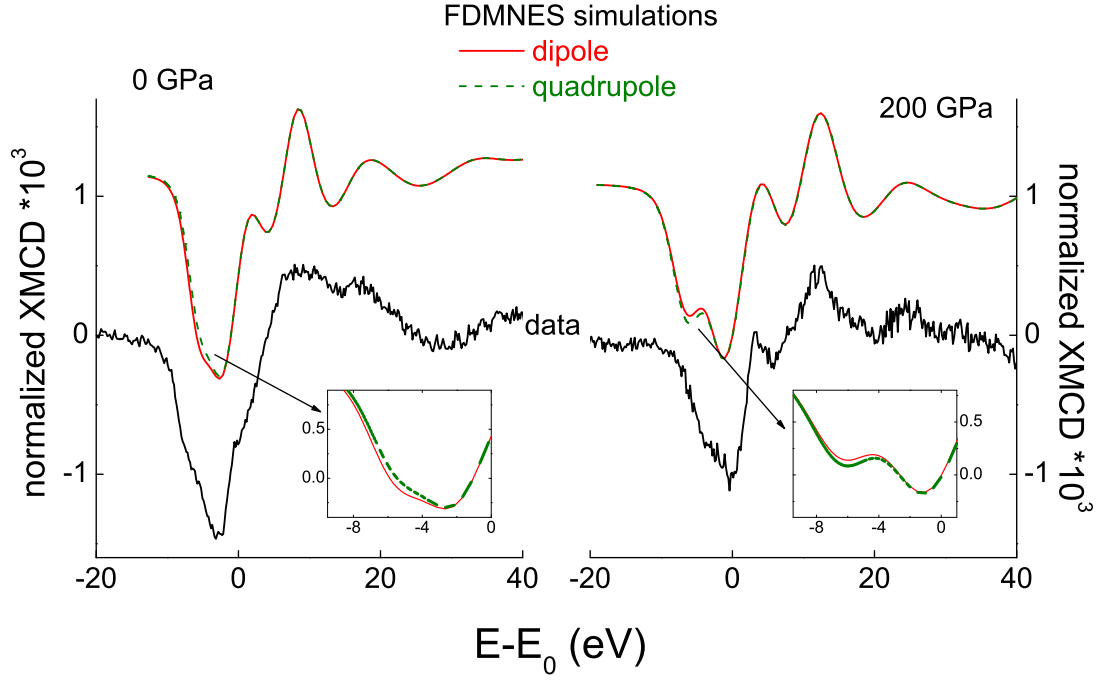


Figure 4.8: left: XMCD data at 0 GPa and FDMNES simulations using dipolar and quadrupolar approximations (full and dashed lines respectively); right: the same at 200 GPa.

XMCD spectra were also simulated using the FDMNES code [223] using the same parameters as for the XANES simulations. A configuration $3d^8 2s^2$ was used with 4.5 $3d$ electrons with spin up and 3.5 $3d$ electrons with spin down. The simulations reproduce fairly well the change of shape and the attenuated intensity of the nickel K-edge XMCD signal under pressure, confirming that the observed modifications origin from the reduced interatomic distances leading to bands broadening and a decrease of the density of states at the Fermi level. Moreover our simulations indicate that quadrupolar terms mainly affect the pre-edge region between -4 and -8 eV from the edge and give rise to a deviation of 3-4% for the main peak integral in the whole pressure range; simulations using the tight binding approach [63] had previously brought to similar conclusions.

If we compare the XMCD and XANES spectra (magnetic and non magnetic absorption) it is clear that they show important differences close to the absorption edge (up to A2 and 3) where the XMCD exhibit a much more complex structure. For higher energies

(from B and 4) the magnetic and non magnetic oscillations show more similar features and move in phase with each other under compression. This distinct behavior allows to roughly identify two energy regions in the XMCD spectra: the first region corresponding to a few eV around the absorption onset, mainly sensitive to the electronic density of empty states close to the Fermi level and containing the magnetic information; the second energy region beyond a few eV, more directly linked to the local structure through single and multiple scattering of the photoelectron (magnetic EXAFS).

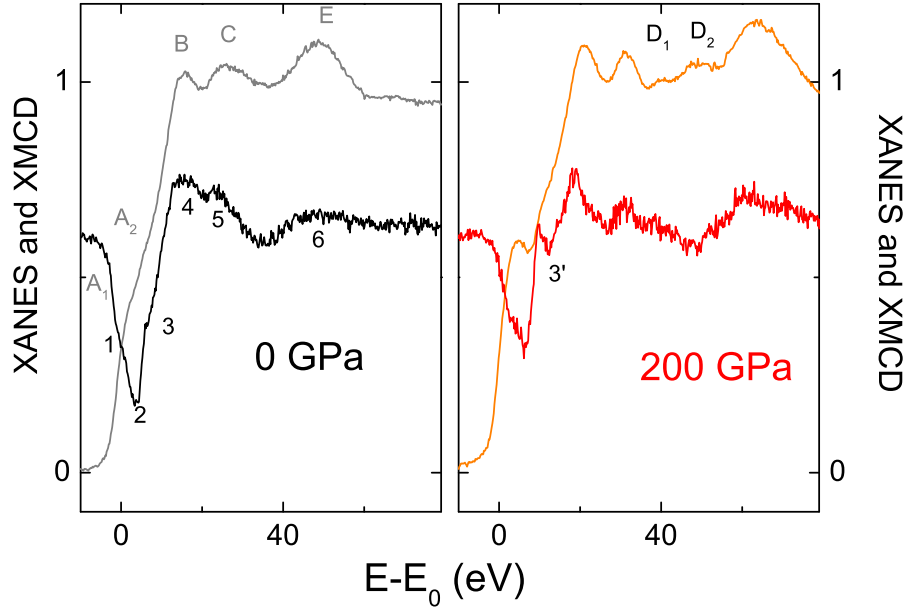


Figure 4.9: left: XANES and XMCD data at 0 GPa; right: XANES and XMCD data at 200 GPa. The XMCD data have been multiplied by a factor 300.

DFT calculations

Exploiting the fruitful collaboration with the ESRF Theory group (Y.O. Kvashnin, L. Genovese, P. Bruno), our results could be compared to novel DTF calculations briefly reported in this section.

As it was discussed in section 2.2.3, the interpretation of the K-edge XMCD signal for the $3d$ metals is still controversial.

The XMCD signal at the K edge of $3d$ metals mainly arises from the spin-orbit coupling of the photoelectron in the final state. Theoretical approaches for the interpretation of K-edge XMCD signals based on multiple-scattering [135, 139–141], and band structure calculations using a tight binding approximation [134] claim that the main contribution to the signal comes from the spin-polarization of the d -states and arises from the scattering of the photoelectron from the spin-orbit potential of the neighbors and of the absorber. Such a view has led to the conclusion that the K-edge XMCD signal should be some-

how proportional to the 3d magnetic moment, and its pressure evolution has been often compared to that of the total spin magnetization [42, 63].

The orbital sum rule (4.3) [131, 133, 134] directly relates the integrated K-edge XMCD to the expectation value of the p -projected orbital moment. Its application to the K-edge of the 3d metals is limited by the assumption of energy independent radial matrix elements $R = \langle 1s|r|4p \rangle$ which does not apply to the broad and delocalized p final states [133, 135]. For this reason, it is quite difficult to extract absolute quantitative information on the magnetic moment from K-edge XMCD spectra.

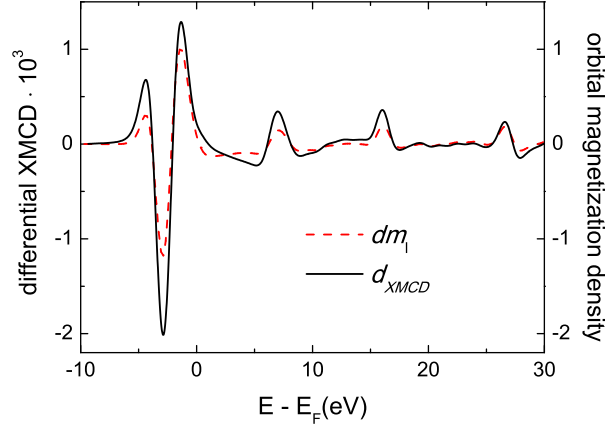


Figure 4.10: Calculated orbital magnetization density of $4p$ -states (right axis) and K-edge differential XMCD for bulk Ni (left axis). The calculations are performed for a zero pressure unit cell using the PY-LMTO code. The curves are broadened with a Lorentzian function of 0.8 eV width.

Nevertheless, as the energy dependence of the matrix elements is smooth, the K-edge XMCD reflects the p orbital polarization in differential form $d\langle L_z \rangle_p / dE$ [136–138]. As a first step, this has been checked for the Ni case by comparing the orbital magnetization density of p -states:

$$dm_l(E) \equiv \sum_{n\mathbf{k}} \left\langle \Psi_l^{n\mathbf{k}} | \hat{l}_z | \Psi_l^{n\mathbf{k}} \right\rangle \delta(E - E_{n\mathbf{k}}) \quad (4.1)$$

to the differential XMCD, defined as:

$$d_{XMCD}(E) \equiv \sum_{n\mathbf{k}} [|\langle \Psi_{n\mathbf{k}} | \Pi^+ | \Psi_{1s} \rangle|^2 - |\langle \Psi_{n\mathbf{k}} | \Pi^- | \Psi_{1s} \rangle|^2] \delta(E - E_{n\mathbf{k}}) \quad (4.2)$$

where Π^\pm is dipole interaction operator of electron with photon of right(left) helicity [138, 210], using the PY-LMTO code [211, 212]. The results, shown in Fig. 4.10 demonstrate that in fcc Ni the differential K-edge XMCD and the $dm_l(E)$ function are indeed closely related. Hence, the relative behavior of the integrated XMCD signal under pressure can be expected to be approximately proportional to that of the p orbital moment.

In order to shed light on the role of the different contributions and interpret the

measured compression evolution of the K-edge XMCD signal, a series of DFT + SO (spin-orbit) calculations have been performed over a wide range of compression (between $V_0^{exp}=10.95 \text{ \AA}$ and 5.04 \AA corresponding to V/V_0 ranging from 1 to 0.46), using Wien2K [215] and PY-LMTO [211, 212] codes. A stable fcc structure up to the TPa range has been assumed, as suggested in [35]. Different treatments of correlation effects have been probed using Local Density Approximation [218, 220] and Generalized Gradient Approximation [221] for the exchange correlation functionals in Wien2K. The Brillouin zone integration was performed on the $28^3(22^3)$ k-point grid.

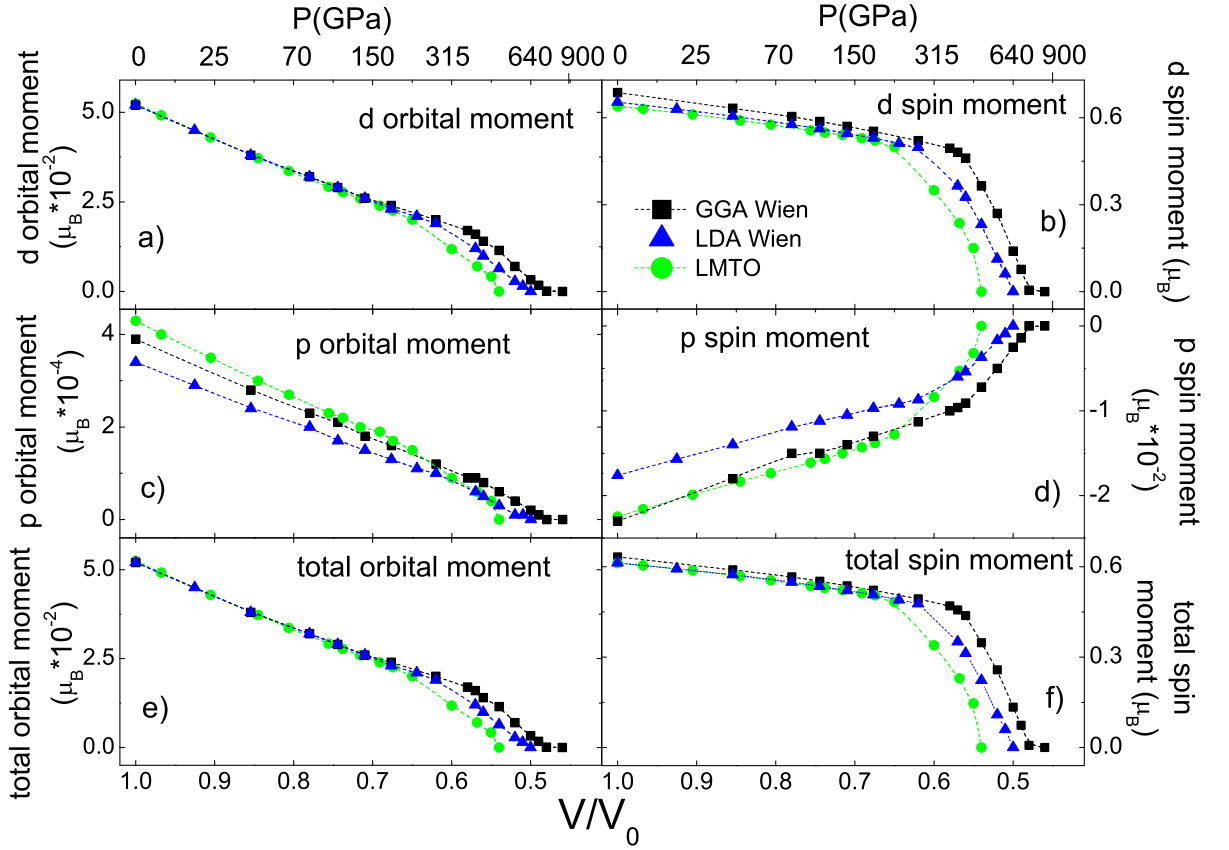


Figure 4.11: panels a), b), c), d), e), f): volume evolution of d orbital, d spin, p orbital, p spin, total orbital and total spin moments respectively by first-principles GGA, LDA and LMTO calculations.

The calculations confirm that the spin polarization of the p states mainly originates from the polarization of the d states through p - d bands hybridization. Once the p -band is polarized, the p orbital moment arises from the SO coupling in both $4p$ and $3d$ states and their relative contribution is 35% and 65% respectively at ambient pressure and 50% at 0.66 relative compression. This was checked performing constrained calculations where the SO constants $4p$ and $3d$ states were alternatively fixed to zero. This result differs from that of ref. [134] where SO coupling in the $4p$ state was found to give a negligible contribution (see Fig. 2.9 in Cap.2).

The ambient values obtained for the spin and orbital d moments, and for the pressure evolution of the total spin moment are in good agreement with previous calculations and experiments [21, 43–45]. The difference found in the ambient moments using different methods results to be quite small for the d spin and orbital moments (1– 6%) but quite significant for the p spin and orbital moments ($\approx 20\%$). However, the slope of the linear compression-induced decay - the physical quantity we are interested in - is similar for each moment component using different methods.

These results indicate that orbital and spin magnetization terms keep decreasing continuously, but with different rates, up to a compression of $V/V_0 \approx 0.6$ where a sharper decay brings to total and simultaneous extinction. The coinciding suppression of spin and orbital moments is not surprising since the orbital moment, quenched by the crystal field, only originates from the spin orbit interaction. Interestingly, the p and d orbital moments behave very similarly with compression whereas this is not the case for the p and d spin moments. The different methods applied are in qualitative good agreement but indicate different critical zero moment volume ranging from $0.48V_0$ to $0.54V_0$. A similar variation in the calculated pressure of moment extinction is found in the case of cobalt [64] (see the *Cobalt* chapter). In fact, the quantitative reliability of these methods at such high compression is limited as the computed quantities are very small and vary very quickly; this fact underlines the importance of high pressure experiments.

XMCD data treatment and normalization

As discussed above, the compression-induced energy shift of the features close to the edge is generally small; however for applied pressures of $P > 100$ GPa the movement of the features 3 and 4 in the XMCD data resulted not negligible. For this reason, the rough XMCD data were re-plotted at each pressure as a function of the abscissa $(E - E_0)/E_E$ (where E_E is the energy position of feature E) so to minimize the influence of the lattice contraction.

To compare the computed quantities to the experimental outputs, the XMCD signal has been integrated from the signal onset ($E_1 = -7$ eV) to four different upper limits: $E_2 = 4$; 6.5; 10.5; 15.5 eV, so to take into account the broad character of the final p states (i.e. the absence of a white line) and normalized to analogous integrals of the unpolarized absorption (XANES) $\mu_0 = (\mu^+ + \mu^-)/2$:

$$A_{XMCD} \equiv \frac{\int_{E_1}^{E_2} dE (\mu^+ - \mu^-)}{\int_{E_1}^{E_2} dE \mu^0}. \quad (4.3)$$

This energy range for the upper limit fully spans the transition zone between the energy region mainly sensitive to the electronic structure and that mainly sensitive to the local structure (magnetic EXAFS) as shown in Fig. 4.12 left panel. Then, the pressure evolutions of (4.3), obtained in the 4 cases, were rescaled to their ambient values and

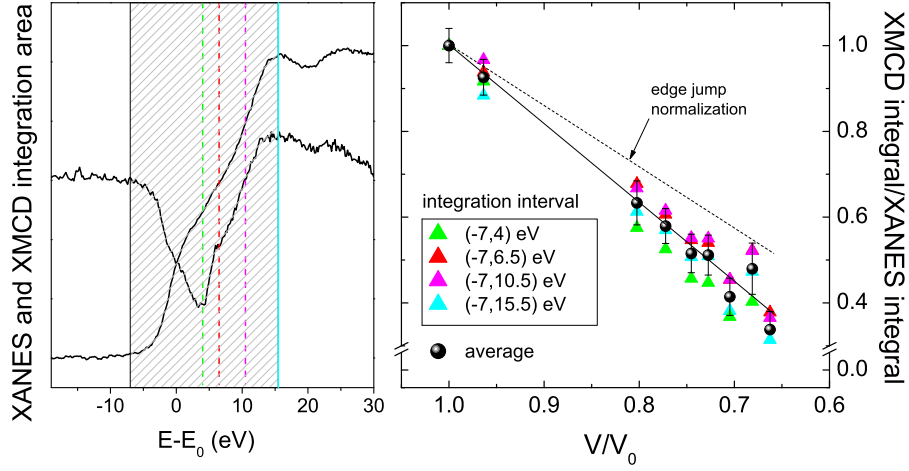


Figure 4.12: left: Sketch of the chosen intervals for the integrals in (4.3). Right: pressure evolution of the XMCD signal normalized as in (4.3) as a function of the upper integral limit; the dashed line shows the trend obtained for XMCD signal normalized to the absorption edge step.

compared (Fig. 4.12 right panel). We found that the error due to the upper limit choice amounts to 4-12% , indicating that the pressure-induced decrease of the so normalized XMCD signal, doesn't change significantly with the energy interval.

This kind of XMCD signal normalization differs from the commonly used normalization to the absorption edge step (normalization by a constant). We believe that (4.3) should be more precise as the main valley of the magnetic absorption (XMCD) is located in the energy interval from few eV before to few eV after the un-polarized absorption (XANES) edge, i.e. in the energy range where the XANES is varying more rapidly (see Fig. 4.12 left panel). Moreover this kind of normalization is the one that appears in the sum rules [131, 133, 134]. Checking the pressure evolution of XMCD signal normalized to a constant edge step shows a smaller decrease but the deviation from the trend obtained with the normalization (4.3) is 14% at maximum, as shown in dashed line in Fig. 4.12 right panel.

In Fig. 4.13 panel c) we plot the average between the pressure evolutions of (4.3) obtained using the four intervals; the error is chosen at each pressure point as the maximum value between the error due to the integral upper limit choice and the error due to the signal noise ($\approx 5\%$). Comparison with theoretical calculations for the total spin moment (Fig.4.13 panel a)) and p -orbital moment (Fig.4.13 panel b)) reveals that the integral of the measured XMCD signal reduces of $\approx 60\%$ in the 0-200 GPa range just like the p orbital moment, while the total spin moment shows a different behaviour decreasing by a 20%.

These results thus indicate that the pressure induced decay of the K-edge XMCD should be compared to that of the p -projected orbital moment rather than to that of the spin moment. Indeed, spin magnetization calculations have proved to reproduce fairly well

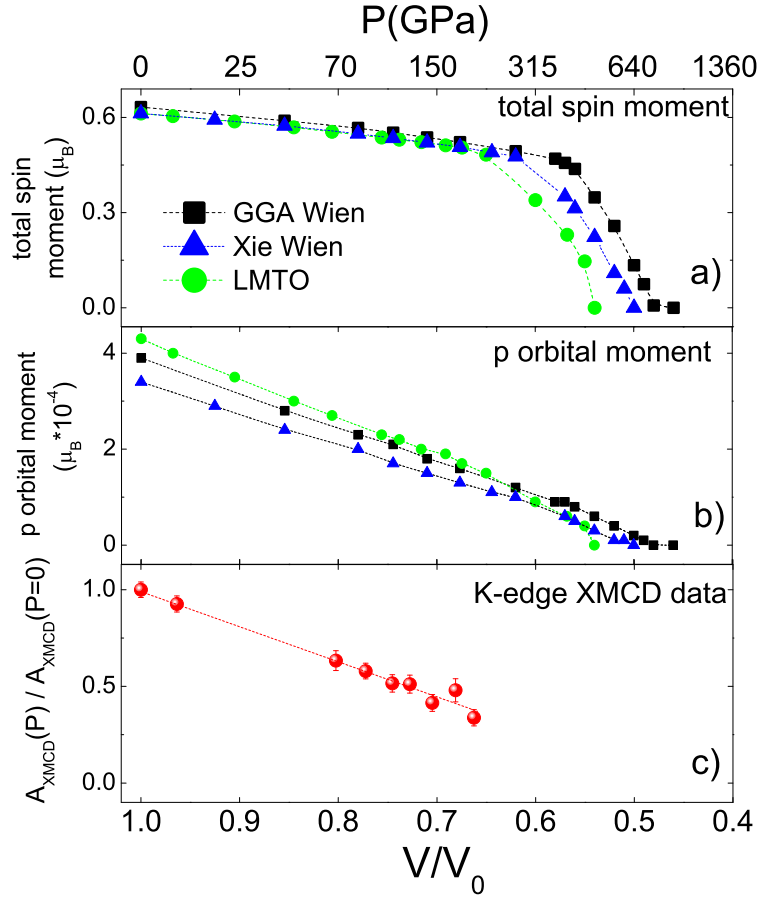


Figure 4.13: Volume evolution of calculated total spin moment (a) and p -orbital moment (b), and of the normalized XMCD integral (A_{XMCD})(c). The unlinear pressure scale in the top axis is calculated with the EOS given in [62].

the high pressure magnetic behavior of the K-edge XMCD in Fe ([43, 45] among others) while they fail in the case of cobalt, as we showed in the *Cobalt* chapter. These differences stimulates further theoretical work. Orbital moments calculations for compressed Fe and Co are still missing in the literature, and a detailed comparison, like we did in the nickel case, is not yet possible.

We are currently working in cooperation with the ESRF Theory group to compare high pressure K-edge XMCD measurements to high pressure orbital and spin moments calculations for all the 3d metals in order to shed light on the observed differences.

4.5 Conclusions

In summary, we have extended up to 200 GPa the pressure range for combined magnetic and structural measurements, by measuring K-edge XMCD-XANES and XRD on pure Ni. The relevance of this study lies not only in the high pressure record reached but also in the coupling of an absorption experiment to a diffraction one, allowing to directly measure

the volume compression and to compare the long range structure to local structure and magnetism evolution under pressure. XRD measurements show a stable fcc pattern up to 200 GPa while the K-XMCD signal decreases continuously under compression and remains non-zero at 200 GPa indicating the persistence of ferromagnetic order. DFT calculations were also performed to compute spin and orbital moment components in compressed Ni, so far missing in the literature, allowing to get a deep insight into their different behavior versus density.

This study can lead to the following conclusions: i) in fcc ferromagnetic Nickel neither structural nor magnetic transitions are observed up to 200 GPa, and the disappearance of magnetism in fcc Ni is predicted to occur at pressures higher than 400 GPa; ii) the spin polarization of the p states mainly originates from the spin polarized d band through p - d bands hybridization and the p -projected orbital moment comes from the spin-orbit interaction in the $4p$ and $3d$ states; iii) the pressure evolution of the nickel K-edge XMCD closely follows that of the p projected orbital moment and not that of the total spin magnetization; iv) in nickel, spin and orbital magnetization do not scale together under compression as was previously assumed in literature [63]; v) quadrupolar transitions give a negligible contribution to the magnetic absorption.

The disappearance of magnetism in Ni is predicted to occur in $V/V_0=0.54-0.48$ (480-740 GPa). However, one cannot rule out a possible crystallographic phase transition, or a transition to a paramagnetic state at ambient temperature after 200 GPa. Hence, further experimental investigations of the magnetic response of Ni under more extreme compressions appear necessary. The present approach is currently under upgrade and the extension of magnetic measurements in the 300-400 GPa range and at low temperature - which would allow to disentangle the moment suppression from Curie temperature effects - looks promising.

These results are published in *Physical Review Letters* [224].

Iron-Cobalt Alloys

The structural and magnetic phase diagram of FeCo under high pressure is particularly fascinating because of the very different behavior of the pure components: iron loosing its ferromagnetism across the bcc-hcp structural transition around 13 GPa and cobalt retaining an hcp ferromagnetic phase up much higher pressures (above 100 GPa). In this chapter we present a detailed study on the P -induced structural and magnetic transitions in $\text{Fe}_{1-x}\text{Co}_x$ in a so far unexplored concentration ($0.5 \leq x \leq 0.9$) and pressure ($P \leq 70$ GPa) range by means of XRD and combined XANES-XMCD measurements. Our results enlighten the close relationship between structure, magnetism and chemical order in this system and allow to draw a first FeCo (x, P) phase diagram.

5.1 Introduction

Alloys of iron and cobalt constitute an important class of soft magnetic materials with a wide and important range of technological applications where high magnetic flux densities are required. Fe-Co alloys find application in data storage, high performance transformers, and pole tips for high field magnets [225, 226]. Thanks to their unique combination of high saturation magnetization, high Curie temperatures, good permeability, good strengths, and excellent performance-to-weight ratio, they have recently been considered for applications in a new generation of aircrafts [227].

From a fundamental point of view, iron-cobalt alloys pose interesting questions because of their structural, magnetic and chemical properties (see [226] for a general review), also because they fall in the interesting category of ordered alloys.

In the transition metals, the magnetic properties mainly arise from the partially filled spin-polarized $3d$ band which in turn is strongly related to the crystal structure and to the local environment. The presence of a dissimilar neighbor, as found in an alloy, may cause an atom to exhibit a wide variety of behaviors due to the different correlations and bands filling [228]. Therefore the investigation of the magnetic/structural behavior of $3d$ alloys as a function of composition and chemical order can bring important issues for a

deeper understanding of magnetic and structural properties in the pure 3d metals.

The structural and magnetic phase diagram of FeCo under high pressure is particularly fascinating because of the very different behavior of the pure components: compressed iron undergoes a transition at 13 GPa from the bcc α -phase to the hcp ϵ -phase structure, losing its ferromagnetism [71, 95]; on the other hand Co remains ferromagnetic up to around 120 GPa [64] and undergoes a transition from the hcp to the fcc structure in the 100-150 GPa range [61, 64, 65] (see the *Cobalt* chapter). In the $\text{Fe}_{1-x}\text{Co}_x$ alloy, Co addition to Fe up to 50% stabilizes the bcc phase to higher pressures whereas the high pressure structural behavior at higher Co content is still unexplored. Moreover, to the best of our knowledge, no studies on the FeCo magnetic properties under high pressure have been ever reported.

The aim of this study is thus to investigate the HP magnetic and structural diagram of the FeCo alloy in the $x \geq 0.5$ region.

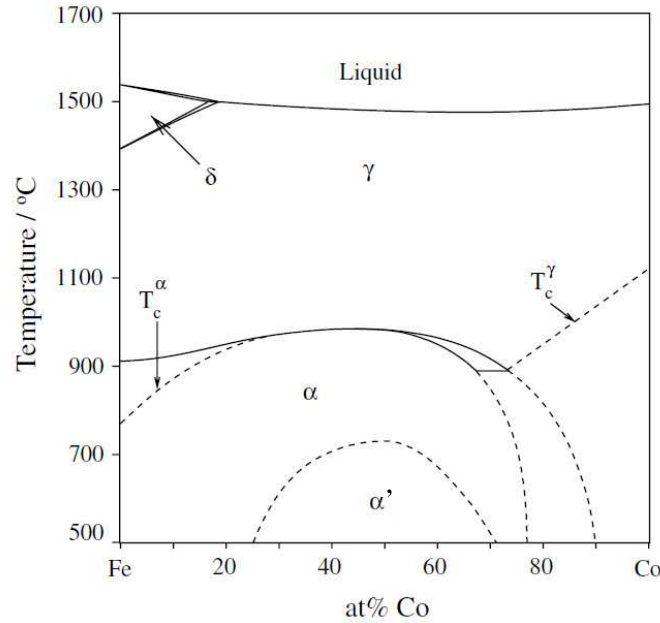


Figure 5.1: (x,T) phase diagram of the Fe-Co system after [231].

5.2 Overview of structural, magnetic and chemical properties in FeCo

5.2.1 The $\text{Fe}_{1-x}\text{Co}_x$ (x,T) phase diagram

Because of their similar electronic structure and atomic volumes, Fe and Co mix with each other over a wide range of concentrations to form alloys. The ambient structure is bcc up to around 75% of cobalt where a transition to the hcp phase occurs [229]. In the $x=0.9-1$ range, fcc ($x=0.9-0.95$), double hcp ($x=0.95-0.99$) and hcp ($x=0.99-1$) structures are reported [230].

The phase diagram of the $\text{Fe}_{1-x}\text{Co}_x$ system as a function of composition and temperature has been extensively investigated [231–239]. The $x=0-0.75$ alloys undergo the bcc (α) to fcc (γ) transition around 900 °C. For Co content less than about 17%, the Curie temperature is reached before the α to γ phase transition while for greater Co% the phase transition to the nonmagnetic γ phase occurs from a ferromagnetic α phase. In nearly equiatomic alloys ($x= 0.3-0.75$) the bcc phase orders to a α' CsCl-type structure at the maximum temperature of 730 °C for $x=0.5$ of composition. In the CsCl structure each atom is coordinated by eight atoms of the other type (see Fig. 5.2 left panel).

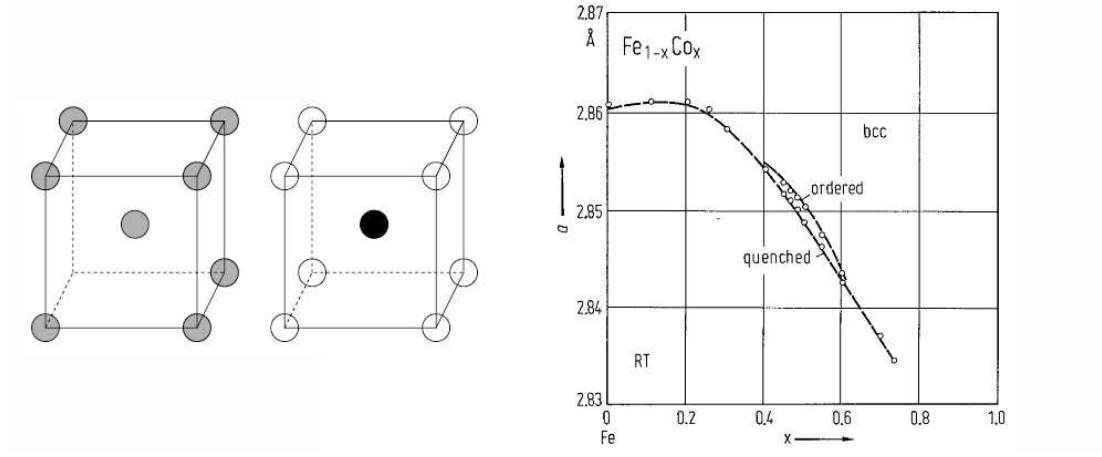


Figure 5.2: Left: bcc (α) and ordered CsCl (α') structures. Right: lattice constant of bcc FeCo as a function of Co %; scatters are from [229], dashed lines are calculated values from [240].

A large attention has been devoted to the ordering transition in the literature (see [226] for a detailed review). Upon ordering, the lattice type changes to simple cubic and the intensity for lines otherwise forbidden in bcc symmetry becomes non-zero. However, this intensity remains extremely small if conventional X-ray methods are used, because of the similar atomic factors of Fe and Co [226]. An increase in the lattice parameter [97, 229, 241] (Fig. 5.2 right panel) and in the magnetic moment [241–244] (Fig. 5.4 right panel) has been observed with ordering. The ordering reaction is very fast and fully disordered samples can only be obtained using quenching rates greater than 4000 °C/s [241].

It has been suggested that the peculiar shape of the α/γ and α/α' boundaries is mainly due to the magnetic contribution, indicating the presence of an interaction between the magnetic and structural/chemical ordering. [233–239].

5.2.2 Ambient magnetic properties

Iron-cobalt alloys have the highest magnetization saturation of all known magnetic alloys (see Fig 5.3). The saturation magnetization of FeCo alloys, measured by Weiss and Forrer [245] and later by Bardos [246] has a non linear behavior as a function of Co concentration

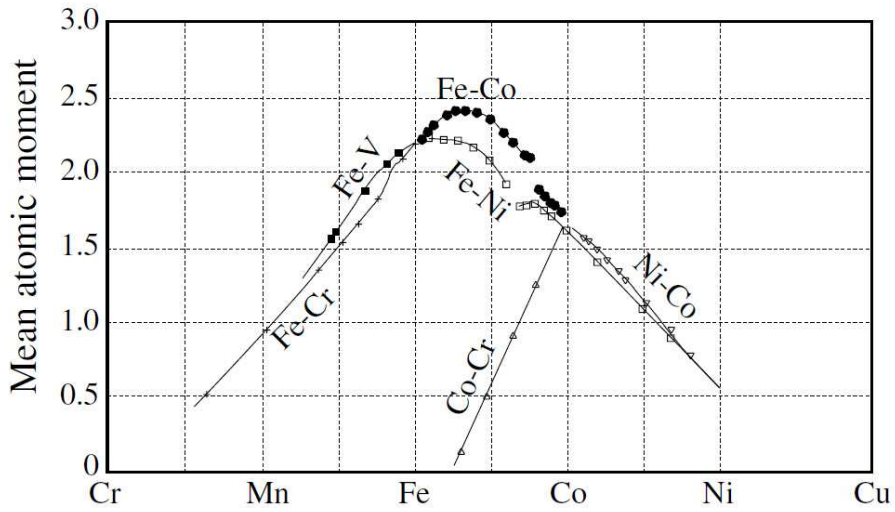


Figure 5.3: The Slater-Pauling curve showing the mean atomic moment for a variety of binary alloys as a function of their composition, after [242].

with a maximum for around 30% Co. Polarized neutron diffraction studies indicate that this nonlinearity is due the increase of the Fe moment from 2.2 for pure bcc Fe to approximately $3\mu_B$ beyond $x=0.5$, whereas the local magnetic moment on Co remains nearly constant around $1.7\mu_B$ [255].

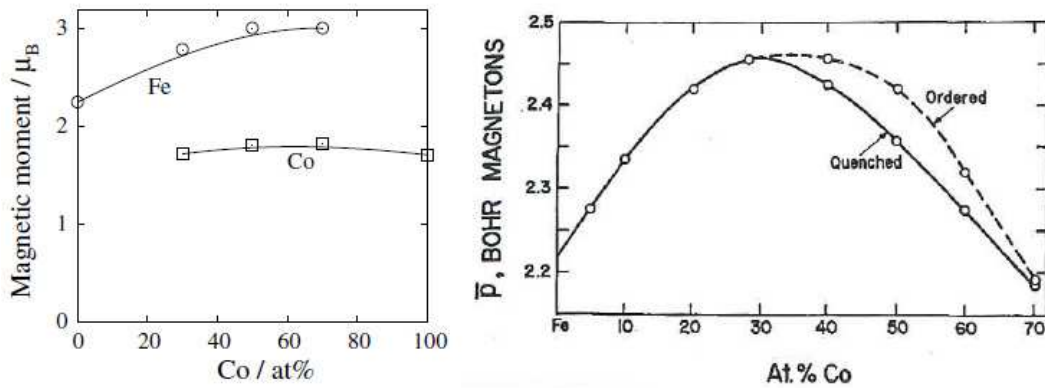


Figure 5.4: Left: the magnetic moments of Fe and Co on binary alloys of different compositions, after [255]. Right: the saturation magnetization of bcc FeCo ordered and disordered alloys as a function of composition from [246].

The dependence of the Fe moment ($\mu_B(\text{Fe})$) on the number of Co nearest neighbors in the α -FeCo has been studied extensively both experimentally [242, 255–257] and theoretically [23, 24]. $\mu_B(\text{Fe})$ is seen to increase with the number of Co neighbors. In an equiatomic Fe-Co alloy with the CsCl type structure, each iron atom is surrounded by cobalt nearest neighbors only; between 50% and 70% Co alloys with the ordered structure contain excess Co atoms, however, this does not change the nearest neighbor configuration

of iron atoms, therefore, the iron moment in this concentration range remains constant. Off-stoichiometric ordered alloys between 30% and 50% Co contain excess iron atoms, which results in a lowering of the iron moment.

Several theoretical works have been dedicated to the understanding of the peculiar behavior of the α -FeCo saturation magnetization as a function of composition [23, 24, 228, 248–254]. The main aspects can be explained in terms of bands filling arguments [23, 228, 253]. As already mentioned, the Co magnetic moment changes slightly with composition while major modifications occur at the Fe site. This is related to the fact that Co is a strong ferromagnet having the majority (spin up) band filled.

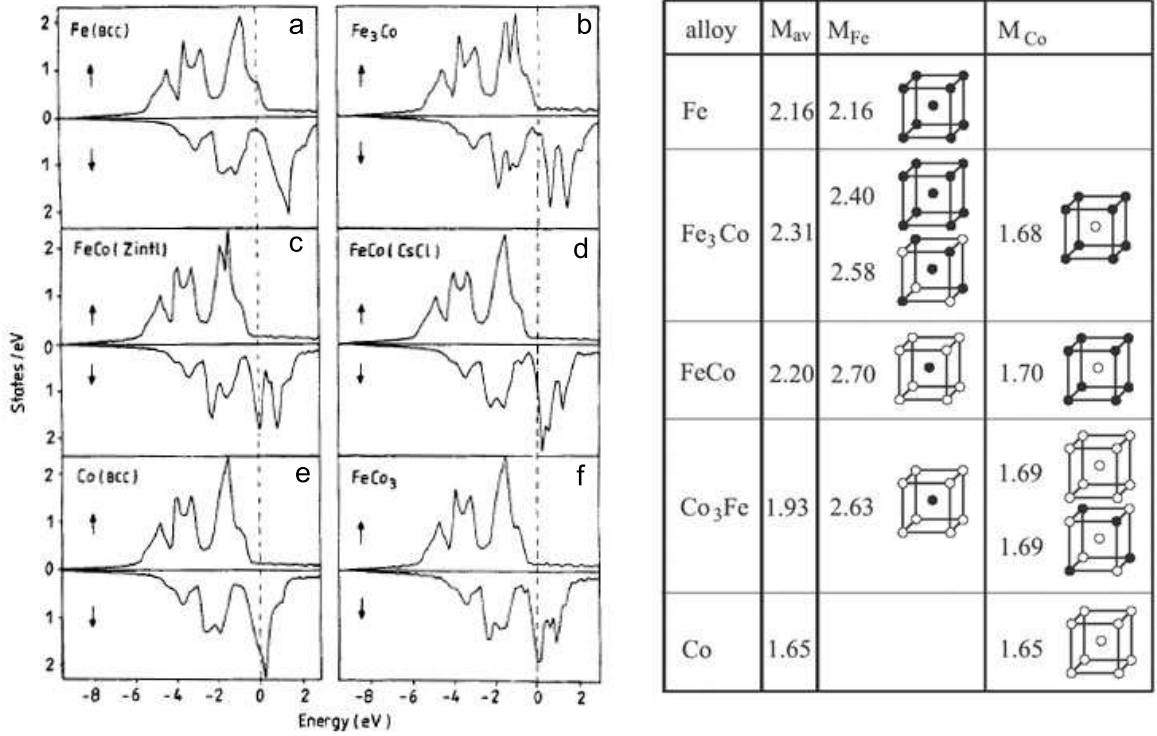


Figure 5.5: Left: spin-projected density of states in FeCo (in states of one spin per atom per eV) from [23]. The energy is with respect to Fermi energy. The calculations are based on the local spin-density treatment of exchange and correlation and employ the augmented spherical-wave method for the required self-consistent energy-band calculation at the theoretical equilibrium volume. Right: local and average magnetic moments of the various ordered structures representing the Fe-Co alloy. For both Fe and Co the first nearest neighbors in each structure are shown [23, 25].

In Fe, both majority and minority spin bands are partially empty and the Fermi energy is pinned at the valley of the minority density of states (Fig. 5.5 left, panel a), hence Fe is classified as a weak ferromagnet. Co addition to Fe leads to the filling of the majority band so that Fe_{1-x}Co_x becomes a strong ferromagnet starting from $x \geq 0.3$ (Fig. 5.5 left, panel b). For Co contents higher than 30%, the additional valence Co electron is accommodated in the minority spin states resulting in a nearly constant value for the average number of

majority electrons (N^\uparrow) (Fig. 5.5 left, panels d and f); the alloy thus remains a strong ferromagnet, and the moment falls primarily due to the filling of Fe d minority states (N^\downarrow) as expected from a rigid band model. The variation of the Fe moment on the Fe rich side is more complex since there is a change in the occupancy of both majority and minority states. In both ordered and disordered alloys, the number of Fe majority states increases with the Co content. Meanwhile the number of Fe minority states decreases and this appears to be due to hybridization changes on the occupied states near the Fermi energy [23, 228, 249, 250, 253, 254]. As a result, a rapid increase in the Fe moment, which is proportional to the difference in majority and minority states $\mu \approx N^\uparrow - N^\downarrow$, is observed. Thus, it is the combination of the roughly constant Co moment and varying Fe moment that accounts for the maximum in the Slater-Pauling curve occurring at around 30 at % Co [24]. The bands modifications occurring because of the Fe-Co alloying are extensively illustrated by Schwarz and co-workers [23] and reported in Fig. 5.5. In this work the authors consider - besides the above mentioned ordered CsCl structure - the disordered Zintl structure for $x=0.5$ in which each atom is coordinated with four atoms of the same type and four of the other type (Fig. 5.26).

According to Victoria and co-workers [228] the enhancement of the magnetization in FeCo following Co addition would be driven by the strong electron-electron interactions of Co, which are sufficient to increase the exchange splitting of the Fe atom, consequently saturating the magnetization without substantially diminishing the Co moment [228].

In the very high Co concentration range ($x > 0.9$) the FeCo magnetization keep decreasing up to pure Co showing discontinuities in correspondence to the structural changes (fcc \rightarrow dhcp \rightarrow hcp) present in this range [230] as shown in Fig. 5.6.

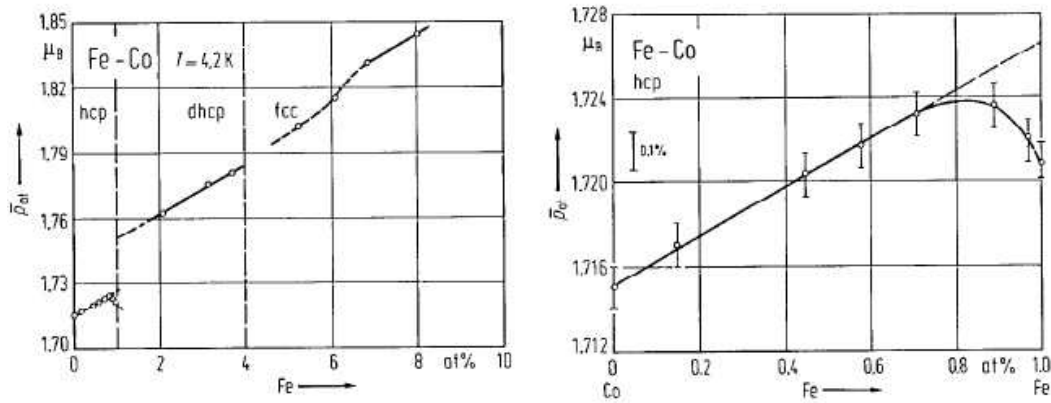


Figure 5.6: Left: mean magnetic moment in hcp, dhcp and fcc FeCo alloys as derived from the saturation magnetization of polycrystalline samples at 4.2 K. from [258] Right: zoom of the hcp region.

In 1994 Pizzini and co-workers analyzed the specific features of K-edge magnetic circu-

lar X-ray-dichroism spectra of Fe and Co in bcc Fe-Co alloys and Fe/Co multilayers [188] as a function of composition (see Fig. 5.7). They found important differences between the Co K-edge and Fe K-edge spectra of the same alloy showing that the signal is central atom dependent. At the Fe K-edge a positive pre-edge peak (named A1 in Fig. 5.7) is observed in both alloys and multilayers and related to the presence of Fe atoms in the neighbors of the absorbing Fe atom. According to multiple scattering calculations [189], this positive pre-peak originates from the scattering of d component of the photoelectron on neighboring sites, and is never encountered at the Co K-edge likely because of the Co d bands different polarization [188]. Moreover in the alloys, some systematic variations of shape and amplitude of the XMCD signals as a function of concentration could be individuated and correlated to the changes in local atomic environment. In particular the Fe K edge signal amplitudes showed a behavior similar to that of the Fe magnetic moment: an increasing trend up to 50% of Co and saturation afterwards. Well above the absorption edge ($E-E_0 > 80$ eV) the extended X-ray-absorption fine structure (EXAFS) oscillations (magnetic EXAFS) reflect the local bcc structure and appear not to depend on the absorbing atom. In both alloys and multilayers, the magnetic EXAFS intensity could be correlated to the average magnetization in the neighborhood of the absorbing atom.

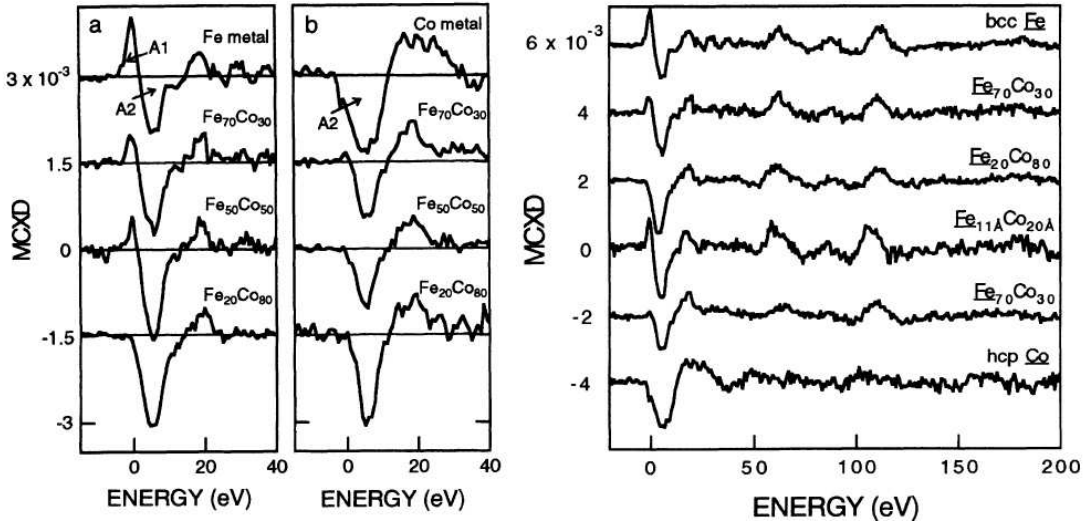


Figure 5.7: Left: Fe K and Co K near-edge XMCD spectra for FeCo alloys. panel (a) Fe K edge, panel (b) Co K edge. from [188] Right: high-energy XMCD spectra (magnetic EXAFS) of FeCo alloys and multilayers. Fe: Fe K edge, Co: Co K edge from [188].

5.2.3 High pressure studies

Co addition to Fe stabilizes the bcc phase to higher pressures in the $x=0-0.5$ range. The existing data, produced using different techniques: XRD [259], shock wave techniques [263] and electric resistance measurements [260, 261], report a consistent curve of the bcc-hcp transition pressure versus concentration. Such a good agreement, between different

techniques, had supported the idea of using FeCo as a pressure calibrant.

The CsCl long range order, characteristic of the (nearly) equiatomic samples, seems not to affect the structural transition. Some disagreement is found in the compressibility data between [263] and [259], as two opposite trend are reported with increasing Co%.

Compression data and high pressure structural data from Papantonis and co-workers [259] will be discussed and compared to our XRD data for the higher Co % range in the *Results and discussion section*.

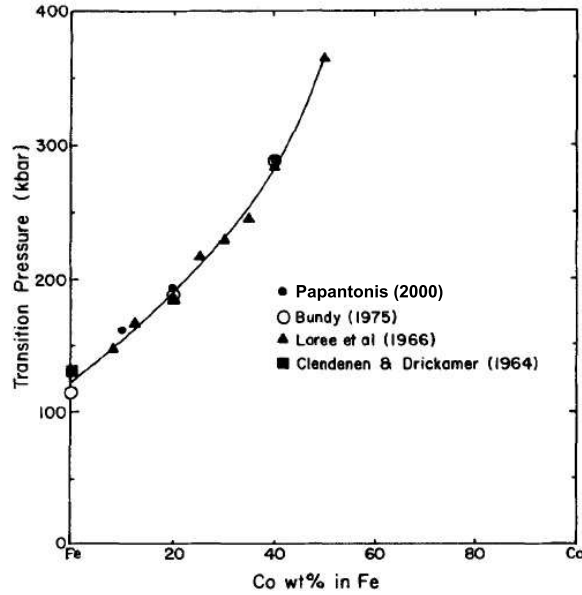


Figure 5.8: The bcc-hcp structural transition in FeCo as a function of Co content. Full circles: [259], open circles: [260], full triangles: [263], and full squares: [262].

5.3 Experiment

The samples

Homogeneous films (thickness ≈ 5 microns) of polycrystalline $\text{Fe}_{1-x}\text{Co}_x$ have been produced using RF magnetron sputter deposition [265] by the group of Prof. M. Gibbs in the University of Sheffield.

The synthesis apparatus is made up of a non rotating target and a stationary substrate; a sketch is shown in Fig. 5.9. When the dimensions of the target, that of the substrate and the distance (D) between them are all comparable and the mean free path of the sputtered atoms is small compared to D , then, from geometrical considerations and basic diffusion theory, a uniform gradient is expected. In the case of FeCo, characterized by similar sputtering yield coefficients and atomic sizes of the constituents, this produces an equiatomic composition at the center of the sample. The target material was a $\text{Fe}_{0.5}\text{Co}_{0.5}$ with 150 mm of diameter (produced by Testbourne Ltd) with additional sheets of pure Co

(from Goodfellows) on top, cut to proper segment sizes to give the required composition. The films were grown on glass substrates with a very thin Al underlayer (less than 20 nm). Sputtering power was between 100 and 250 W, with a target-substrate separation of $D=60\text{mm}$, and deposition time was 6 and 24 hours for equiatomic and non-equiatomic samples respectively. The samples were removed from the substrate after growth and characterized by hysteresis loops and energy dispersive X-ray analysis (EDX) measurements to check magnetism and composition.

One of the samples ($x=0.5$) has been annealed up to 350° for 24h to check differences in the ambient and high pressure properties with respect to the not annealed samples.

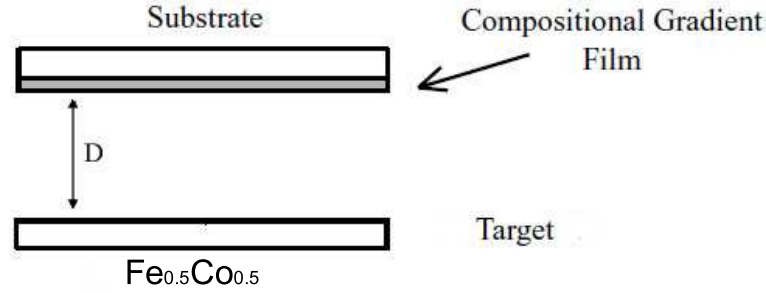


Figure 5.9: Experimental schematic of bicomposite target to produce a film of varying composition.

XANES and XMCD measurements

The XANES-XMCD measurements reported in this chapter have been performed in three different synchrotron beamline stations: at the dispersive beamline ID24 at ESRF (European Synchrotron Radiation Facility, Grenoble, France), at the dispersive beamline ODE in SOLEIL (French National Synchrotron Facility, Saint Aubin, France) and at the scanning 4ID-D beamline at APS (Advanced Photon Source, Argonne National Laboratories, US).

$\text{Fe}_{1-x}\text{Co}_x$ alloys with $x=0.5, 0.6, 0.75$ have been measured at the Co ($E_0=7709\text{ eV}$) and Fe ($E_0=7112\text{ eV}$) edges; the $x=0.9$ sample has been measured at the Co K-edge only. Depending on the elemental content, 1-3 layers were charged into an amagnetic diamond anvil cell (DAC) with Silicone oil as a pressure transmitting medium; the pressure was measured with the ruby fluorescence technique. In order to evaluate the pressure error, 2-3 ruby spheres were placed in the DAC in different positions. The investigated pressure range was 0-45 GPa for the $x=0.5-0.75$ samples and 0-70 GPa for the $x=0.9$ sample. Amagnetic Cu-Be DAC of the Chervin type [107] were used at ID24 and ODE while an amagnetic symmetrical Cu-Be DAC model WCM-7B (manufactured by easyLab Technologies Ltd [264]) was used at 4ID-D. The applied field was 0.7, 1.3, 0.6 Tesla at ID24, ODE and 4ID-D respectively.

Of the three beamlines, ID24 offers the highest flux and smallest beam ($5 \times 5 \mu\text{m}$ full width at half maximum (FWHM)) allowing a better signal to noise ratio, faster measurements and the possibility to use smaller samples ($20 \times 20 \mu\text{m}$) thus accessing higher pressures and a higher degree of hydrostaticity. In fact in the ID24 setup samples sizes can be half or less the hole size, while in the ODE and 4ID-D setup the samples are nearly as big as the hole.

The XMCD signal is obtained by taking the difference between X-ray absorption spectra measured using parallel (μ^+) and antiparallel (μ^-) orientations of the sample magnetization relative to the incident photon helicity. In the XMCD setup of ID24 (ESRF) and 4ID-D (APS) this difference is obtained both by flipping the applied magnetic field and the photon helicity by means of a phase retarder (quarter wave plate). In the ODE setup only the magnetic field is flipped as no phase retarder is used.

In general, measurements at the Fe K-edge are more complex than at the Co K-edge because of the lower transmission which is less than 0.4% through a pair of 1.2 mm-thick diamonds. This can be improved by the use of a partially perforated diamond anvils facing a totally perforated anvil with a mini-anvil glued on top (see the *Experimental Methods* chapter), but this increases the possibility of diamonds breaking. This kind of setup was used in the experiment at 4ID-D (APS) [158]. Moreover, absorption at the Fe K-edge is more frequently disturbed by the presence of diamonds glitches.

XRD measurements

Angle dispersive XRD measurements were performed on the FeCo alloys to check the long range order. All the samples were measured at beamline ID27 (ESRF, France) [205] apart from the $x=0.6$ sample which was measured at beamline HPCAT BM-D (APS). The monochromatic x-ray signal diffracted by the samples has been collected on a MAR345 imaging plate system, located at distance of ≈ 200 and ≈ 300 mm at ID27 and HPCAT BM16 respectively. The signal was then circularly integrated using the FIT2D software [266].

At ID27, samples of $15 \times 15 \mu\text{m}$ size were charged in a membrane Le-Toullec DAC with He gas as transmitting medium. At HPCAT $50 \times 50 \mu\text{m}$ sized samples were charged in a screw Symmetric piston-cylinder DAC and the transmitting medium was Ne gas. Pressure was estimated using the ruby fluorescence method [187] on 2-3 ruby spheres placed in different positions in the DAC.

	$x = 0.5$		$x = 0.5$ an	$x = 0.6$		$x = 0.75$		$x = 0.9$
	Co K-edge	Fe K-edge	Co K-edge	Co K-edge	Fe K-edge	Co K-edge	Fe K-edge	Co K-edge
ID24			X	X				X
ODE	X	X				X	X	
4ID-D					X			

Table 5.1: XAS measurements of the $\text{Fe}_{1-x}\text{Co}_x$ alloys in different beamlines.

Diffraction data were analyzed using the GSAS program [269, 270] and d-spacing were determined using a Le Bail fit [271, 272]. The obtained compression data, were then fitted to a third order Birch-Murnaghan equation of state [273]:

$$P(V) = \frac{3K_0}{2} \left[\left(\frac{V_0}{V} \right)^{\frac{7}{3}} - \left(\frac{V_0}{V} \right)^{\frac{5}{3}} \right] \left\{ 1 + \frac{3}{4} (K'_0 - 4) \left[\left(\frac{V_0}{V} \right)^{\frac{2}{3}} - 1 \right] \right\}. \quad (5.1)$$

where V_0 is the ambient pressure volume, K_0 is the bulk modulus and K'_0 is its first derivative.

The different experimental conditions for both XAS and XRD experiments are summarized in Table 5.2.

beamline	Magnetic Field (Tesla)	FWHM (μm)	hole diameter (μm)	sample size (μm)	transmitting medium
ID24	0.7	5x5	100-120	50x50	silicone oil
ODE	1.3	25x35	120-140	100x100	silicone oil
4ID-D	0.6	20x30	120	100x100	silicone oil
ID27		2x2	100	10X20	He
HPCAT BM-D		10x20	100	30X40	Ne

Table 5.2: Experimental conditions for XAS and XRD experiments.

5.4 Results and discussion

Equiatomic and nearly equiatomic samples: $\text{Fe}_{0.5}\text{Co}_{0.5}$ and $\text{Fe}_{0.5}\text{Co}_{0.6}$

In Figs. 5.10 and 5.11 we represent high pressure combined XANES-XMCD measurements for $\text{Fe}_{0.5}\text{Co}_{0.5}$ and $\text{Fe}_{0.4}\text{Co}_{0.6}$ respectively at the Co K-edge (upper panels a) and b)) and Fe K-edge (lower panels c) and d)).

In both samples the ambient profile of the XANES is characteristic of the bcc structure. A slight difference can be observed between the two edges in the pre-edge feature a being more resolved at the Fe K-edge. The pressure evolution of the XANES is similar at the Fe and Co edges: the pre-edge shoulder a ($E \approx 4$ eV) continuously grows in intensity and becomes more pronounced, the "white line" feature b ($E \approx 20$ eV) loses intensity, the double-shaped first oscillation c at ≈ 50 eV turns into a single rounded one while the second and third oscillations d and d' (≈ 84 and 109 eV) merge into a single oscillation. These changes mark the bcc-hcp transformation just like in the iron case [93, 95]. The hcp

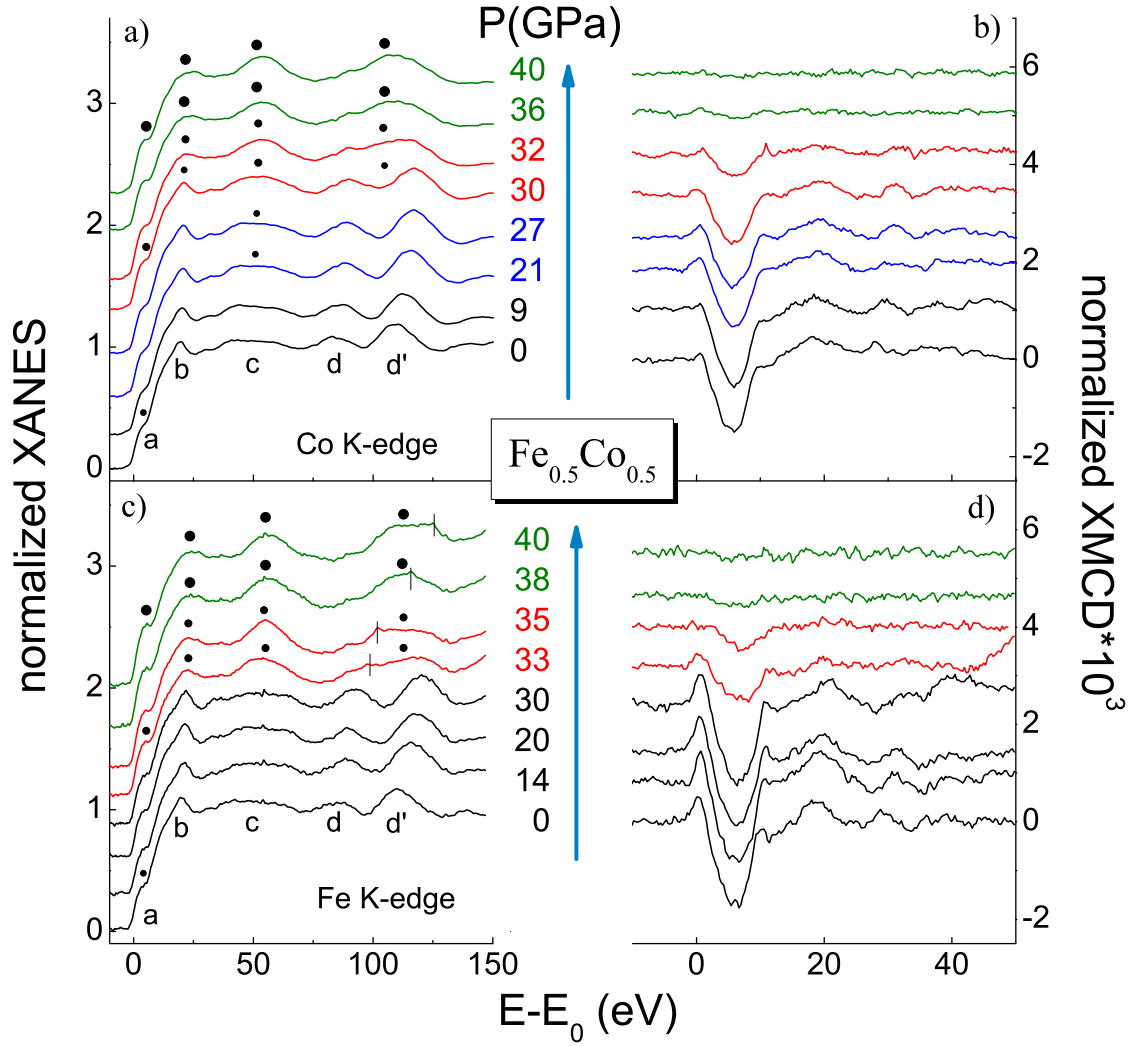


Figure 5.10: a) and b): normalized XANES and XMCD spectra of $\text{Fe}_{0.5}\text{Co}_{0.5}$ at Co K-edge; c) and d) normalized XANES and XMCD spectra of $\text{Fe}_{0.5}\text{Co}_{0.5}$ at Fe-K-edge. In panel c) the presence of a diamond glitch is signaled by short lines.

structure is stable from around 36-38 GPa as no further transformations are observed. In $\text{Fe}_{0.5}\text{Co}_{0.5}$, at the Co K-edge, the modification of feature *c*, becoming rounder, anticipates that of the other features (*b*, *d*, *d'*), while at the Fe K-edge the *b c d* and *d'* features change together and abruptly at 33 GPa. In the $x=0.6$ sample, the change in the feature *c* (around 20 GPa at the Fe K-edge and even before at the Co K-edge ≈ 12 GPa) anticipates that of the other features at both edges; however this effect is still stronger at the Co K-edge. These evidences suggest the presence of local bcc-hcp distortion anticipating the total transition around 30 GPa.

The simultaneous XMCD measurements show a different ambient shape of the XMCD signal at the Fe and Co K-edge: at the Fe K-edge the main negative valley has stronger intensity and is accompanied by a pre-edge positive lobe which is almost absent at the

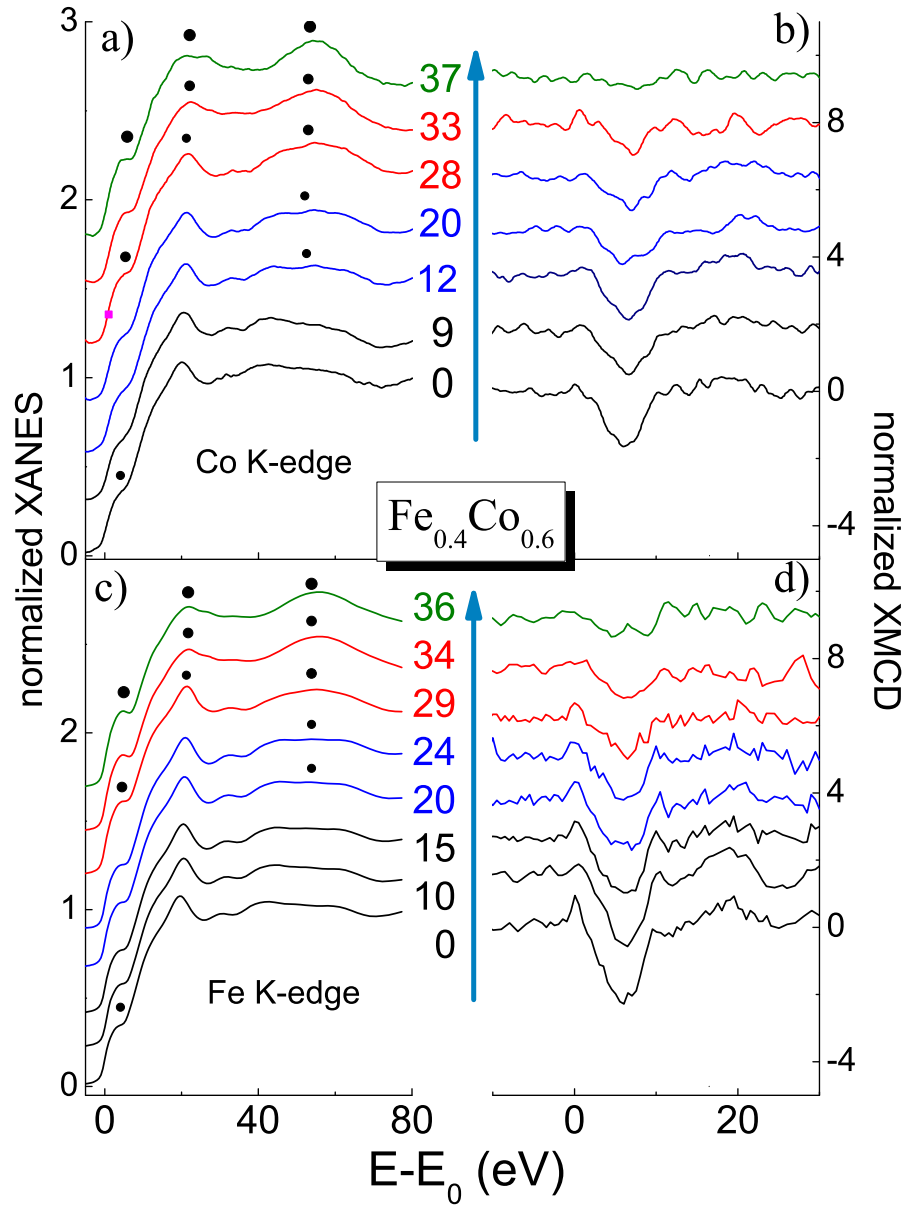


Figure 5.11: a) and b): normalized XANES and XMCD spectra of $\text{Fe}_{0.4}\text{Co}_{0.6}$ at Co K-edge; c) and d) normalized XANES and XMCD spectra of $\text{Fe}_{0.4}\text{Co}_{0.6}$ at Fe-K-edge.

Co K-edge. This difference has been already highlighted by Pizzini and co-workers [188]. Compression leads to the decrease of the XMCD signal with total extinction occurring in correspondence with the bcc to hcp transition, indicating that the high pressure hcp structure in $\text{Fe}_{0.5}\text{Co}_{0.5}$ is non ferromagnetic, just like in iron.

XRD measurements were performed to check the structural transition (shown in Figs. 5.12 and 5.13 upper panel). The appearance of the hcp phase (ϵ) reflections is observed at 31 GPa and the transition is completed around 36 GPa. The observed local distortions in the XANES in the 20-30 GPa range do not correspond to any modification in the XRD.

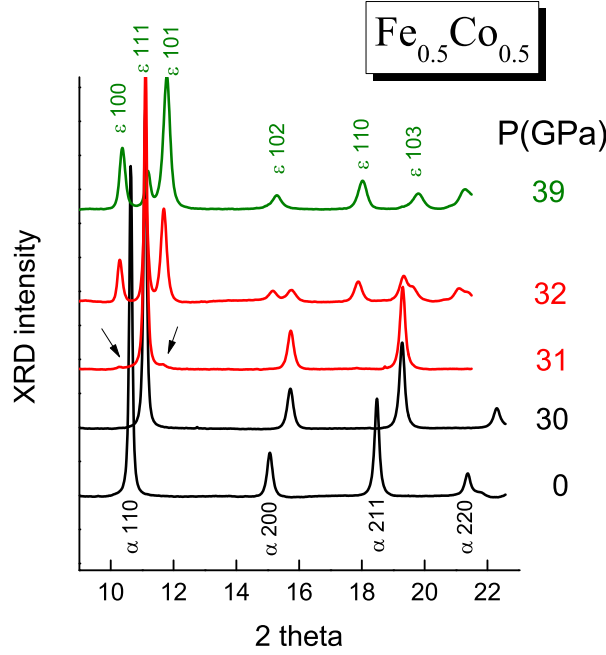


Figure 5.12: Selection of XRD patterns of $\text{Fe}_{0.5}\text{Co}_{0.5}$ as a function of pressure. The bcc (α) and hcp (ϵ) phase reflections are indicated.

This difference could in principle be due to the different hydrostatic conditions as XAS measurements were performed using Silicone oil while He and Ne gas was used for XRD. However the estimated pressure gradient for Silicone oil in this pressure range is around 2-3 GPa, well below the observed difference in the pressure onset of XANES and XRD modifications. Indeed, it is not surprising that precursor signs of the bcc/hcp transition are only visible in the XANES - which is a local (short order) probe - as the presence of randomly distributed small ($<10\text{\AA}$) clusters of distorted FeCo would be invisible to XRD - a long range order probe.

In Fig. 5.14 we compare the pressure evolution of the integral of the main XMCD peak at both edges with the pressure evolution of the bcc/hcp phase fraction as estimated from the Rietveld analysis [267, 268] of diffraction data, for the $x=0.5$ (upper panel) and $x=0.6$ (bottom panel) samples. The phase fraction error is around 10% and the pressure error is within the symbols size. In both samples a sharp decrease of the XMCD signal integral is observed starting from around 30 GPa at both edges, in concurrence to the structural transformation into hcp, indicating that the magnetic and structural transition are simultaneous. The fact that the structural transition, as seen by XRD, occurs over a smaller pressure range (30-36 GPa) is due to the different hydrostatic conditions. Indeed Silicone oil, which was used in the absorption experiment, is not an hydrostatic medium at the pressure of investigation and can give rise to pressure gradients responsible for the transition range broadening (see the *Experimental Methods* chapter for further details). In the $x=0.5$ sample, at both edges, a residual XMCD signal (less than 10%) remains above

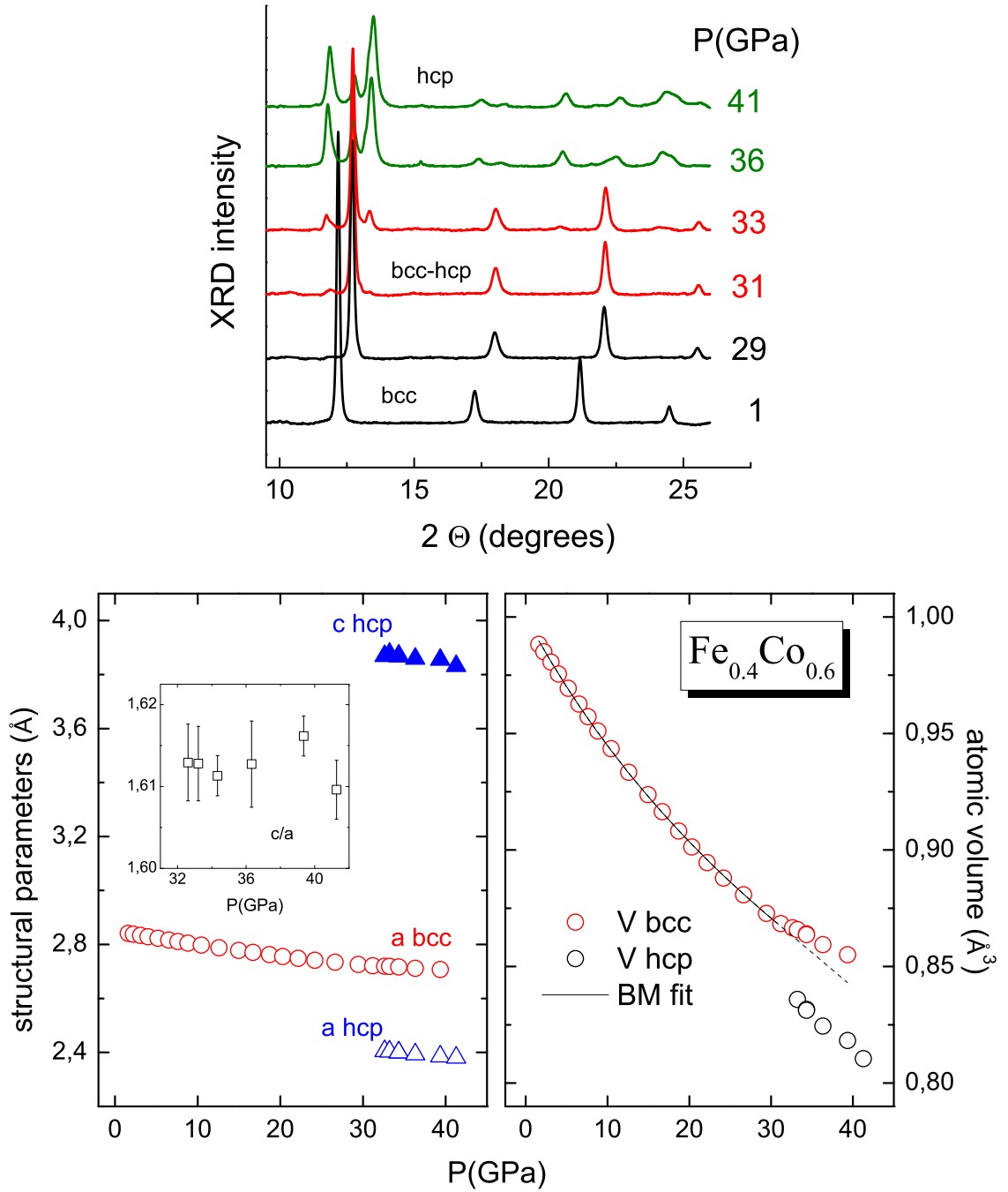


Figure 5.13: Top: selection of XRD patterns of Fe_{0.4}Co_{0.6} as a function of pressure. Bottom: high pressure structural parameters for Fe_{0.4}Co_{0.6} (left); compression curve of Fe_{0.4}Co_{0.6} (right). The uncertainties on volume and pressure are smaller than the symbols. The solid line is a third-order Birch-Murnaghan fit to the experimental data.

the transition. Interestingly, different behaviours are observed in the XMCD in the lower pressure range: in the $x=0.5$ sample, a smooth decrease of the XMCD integral is observed before the transition (between 16 and 30 GPa) only at the Co K-edge while in the $x=0.6$ sample the initial decay of the XMCD integral is stronger ($\approx 55\%$ at 30 GPa) and is the

same at the two edges within the error bar. The comparison between XANES and XMCD behavior suggests that this pre-transition decrease of the XMCD integral is related to the observed modification of the XANES feature *c* in the 20-30 range. The major sensitivity to pressure at the Co site in sample $x=0.5$ is perhaps related to the more asymmetrical shape of the magnetization density around Co (see Fig.1.7 in Chap.1), which may result in earlier magnetic instabilities and associated structural distortions, and the Co excess in the $x=0.6$ sample is likely responsible for making this effect less local, i.e. appearing at both edges.

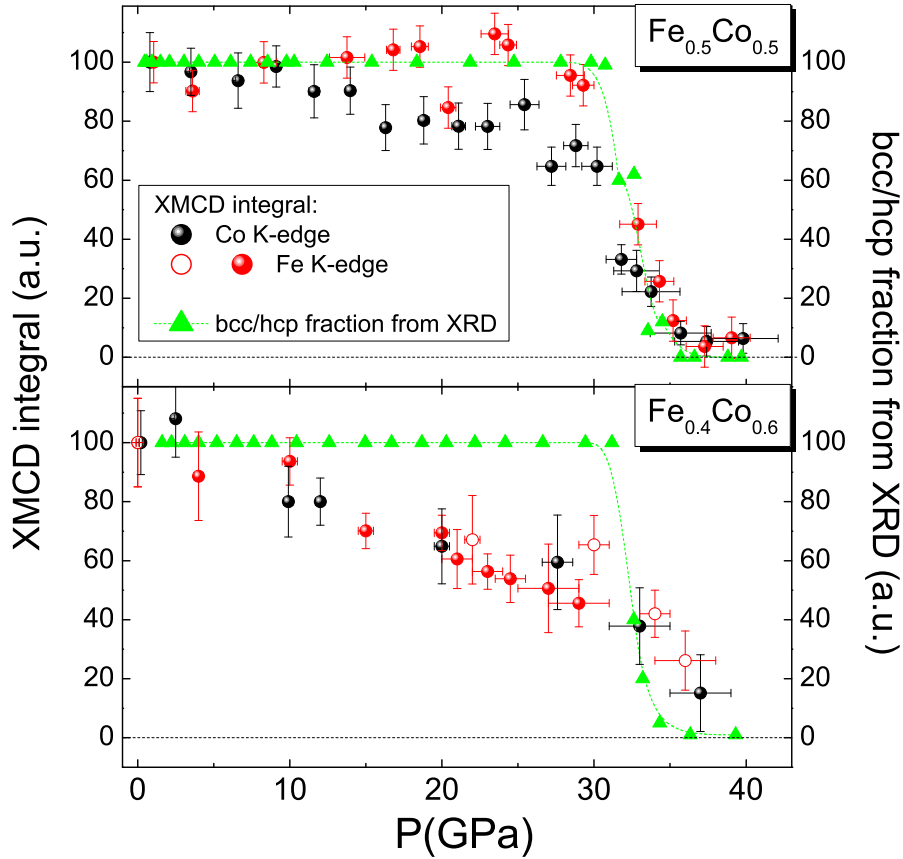


Figure 5.14: Integral of the XMCD signal at Co and Fe edge (black and red full circles respectively) and comparison with bcc/hcp phase fraction from XRD (green full triangle) for sample $x=0.5$ (upper panel) and $x=0.6$ (bottom panel). The phase fraction error is around 10 % and its pressure error is within the symbol size.

The $\text{Fe}_{0.5}\text{Co}_{0.5}$ sample was annealed at 350 °C for 24 h to investigate whether the preparation route can determine differences in the ambient and high pressure properties with respect to the *as prepared* sample. Both absorption (Fig. 5.15, only Co K-edge) and diffraction (Fig. 5.16 top panel) data show that the pressure-induced bcc ferromagnetic to hcp non ferromagnetic transition in the annealed sample is retarded by about 7 GPa compared to the *as prepared* sample, pointing out that the annealing procedure provides a major resistance to pressure.

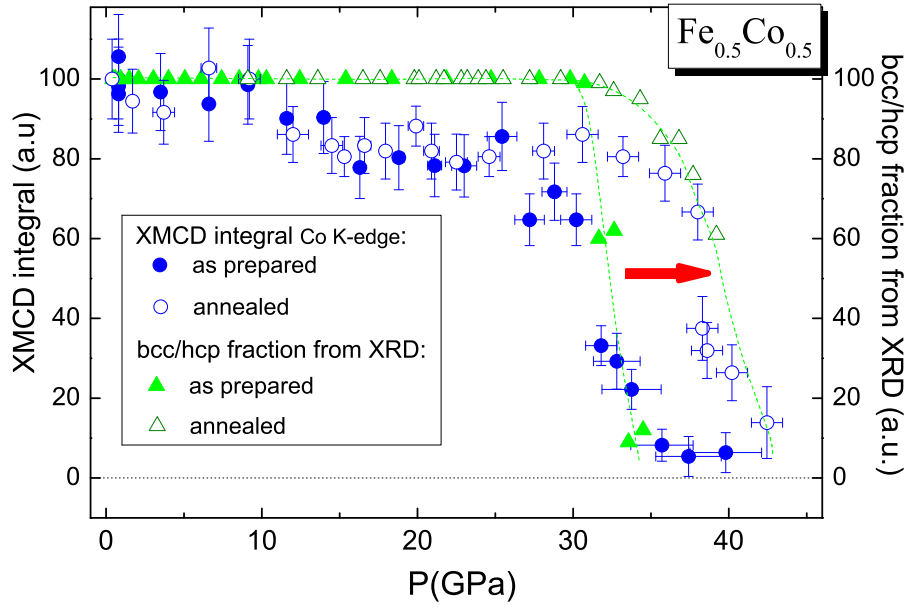


Figure 5.15: Pressure evolution of the Co K-edge XMCD integral of annealed (empty circles) and *as prepared* (full circles) $\text{Fe}_{0.5}\text{Co}_{0.5}$ and comparison with bcc/hcp phase fraction estimated from XRD (empty and full triangles). The phase fraction error is around 10 % and its pressure error is within the symbol size.

Compression data are shown in Table 5.3. The ambient lattice parameter a^{bcc} results bigger for the annealed sample by a 0.2%. This enhanced lattice parameter is likely related to a major degree of order according to Fig. 5.2 and indicates that the annealing has an effect on the ordering reaction. The bcc phases in both annealed and *as prepared* samples show similar compressibility as represented in Fig. 5.17. In the *as prepared* $\text{Fe}_{0.5}\text{Co}_{0.5}$ the a^{bcc} parameter deviates from its compression trend as soon as the bcc to hcp transition starts (Fig. 5.16 bottom right panel); correspondingly the c/a ratio of the hcp structure shows some scattered behavior before reaching the constant value $c/a=1.607\pm0.004$ (Fig. 5.16 bottom right panel). Similar anomalies have been observed in the P-induced bcc-hcp transition in iron and attributed to interfacial strain between the bcc and the hcp phases [88]. A more regular behavior is observed in the annealed sample and the c/a ratio of the newly formed hcp structure results bigger ($c/a=1.614\pm3$). Just like in the iron case, the bcc-hcp transition in $\text{Fe}_{0.5}\text{Co}_{0.5}$ is a first order transition as it occurs with a volume change which results bigger in the annealed sample case.

These results demonstrate that the sample annealing does not change the sample compressibility but increases the sample resistance to pressure as the structural-magnetic bcc-hcp phase transition is delayed by ≈ 7 GPa. Moreover the higher a parameter suggests that this enhanced stability is related to a higher degree of chemical order induced by the annealing.

With respect to the $x=0.5$ sample, the $x=0.6$ sample presents a smaller ambient a^{bcc} parameter ($a^{bcc}=2.852\pm0.003$), volume change ($\Delta V=0.030\pm0.007$) and bulk modulus

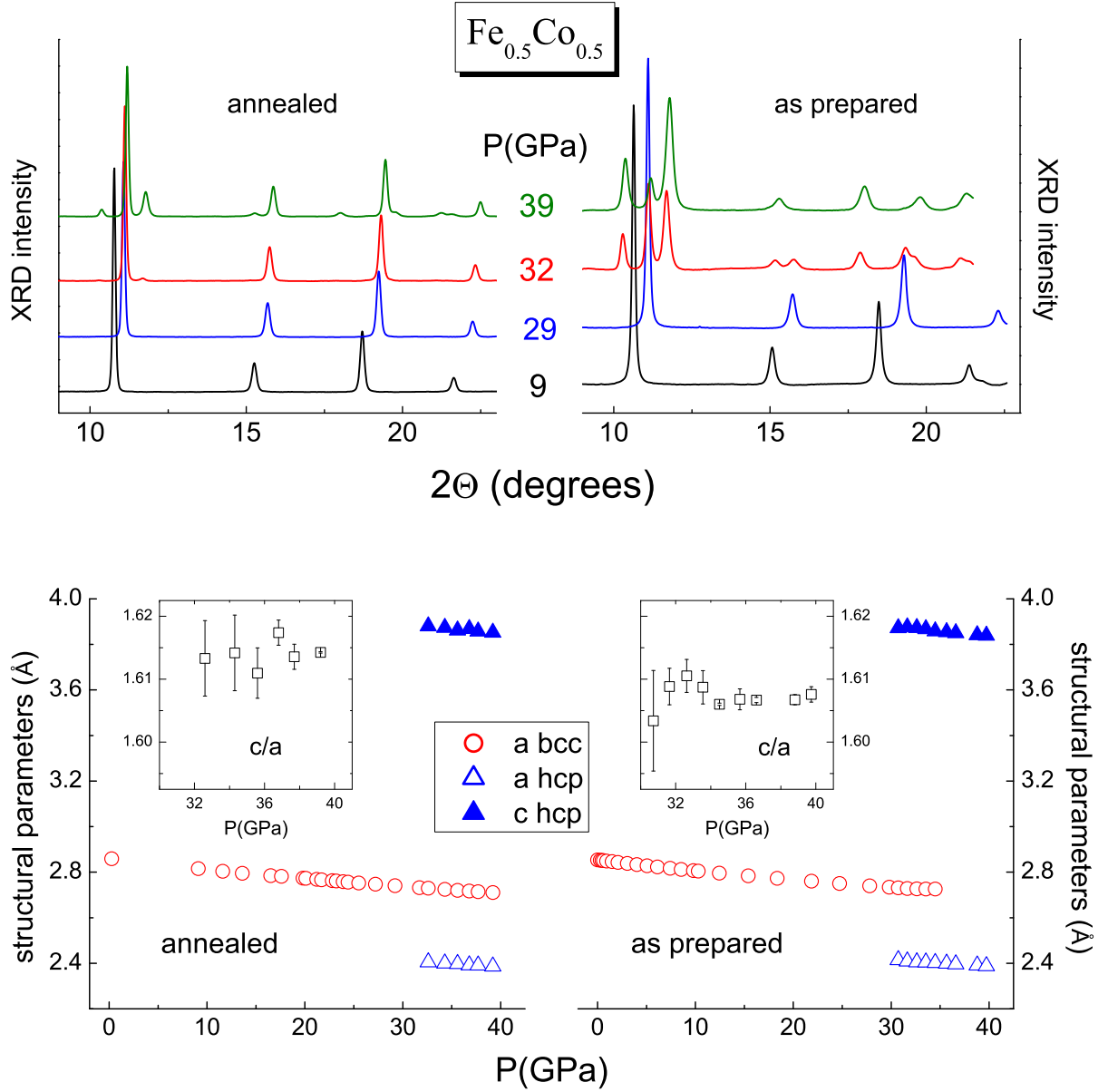


Figure 5.16: Top: selection of XRD patterns of annealed (left) and *as prepared* (right) $\text{Fe}_{0.5}\text{Co}_{0.5}$ as a function of pressure. Bottom: high pressure structural parameters for annealed (left) and *as prepared* (right) $\text{Fe}_{0.5}\text{Co}_{0.5}$.

($K_0=167\pm6$) but a larger c/a ratio of the newly formed hcp structure ($c/a=1.613\pm0.003$). Like in the $x=0.5$ case, the a^{bcc} parameter deviates from the low pressure trend as soon as the transition starts.

In Fig. 5.18 we compare ambient and high pressure structural parameters of the $x=0.5$ and $x=0.6$ samples, obtained from the analysis of the XRD data [271], to those of the lower Co content series reported by Papantonis and co-workers [259]. In that work the Birch-Murnaghan EOS fit was performed keeping the bulk modulus derivative constant $K'_0=4$ which is considered a good approximation for the metals. So, in order to properly

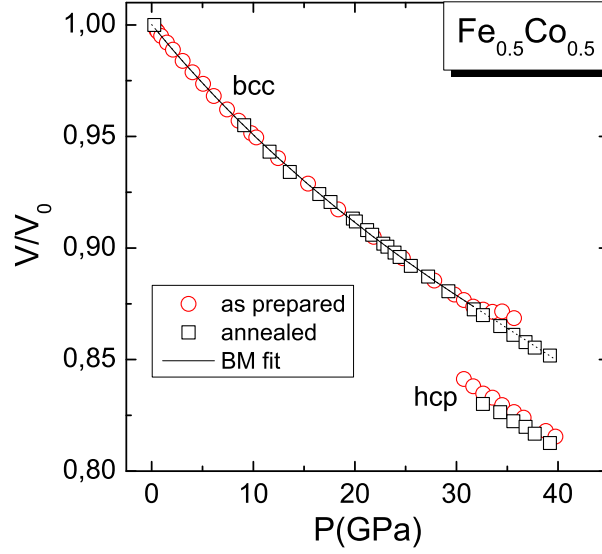


Figure 5.17: Compression curve of annealed (black empty squares) and "as prepared" (red empty circles) $\text{Fe}_{0.5}\text{Co}_{0.5}$. The uncertainties on volume and pressure are smaller than the symbols. The solid line is a third-order Birch-Murnaghan fit to the experimental data.

$\text{Fe}_{1-x}\text{Co}_x$	a bcc (\AA)	c/a hcp	V_0 ($\text{\AA}^3/\text{atom}$)	ΔV ($\text{\AA}^3/\text{atom}$)	K_0 (GPa)	K'_0
x=0.5 as prepared	2.8540(16)	1.6074(35)	11.623(1)	0.0354(1)	177(6)	4.1(1)
			11.622(1)		179(6)	4
x=0.5 annealed	2.860(3)	1.614(3)	11.69(2)	0.0398(1)	181(8)	3.6(1)
	2.861(3)		11.71(2)		174(8)	4
x=0.6	2.852(3)	1.613(3)	11.60(3)	0.0354(1)	152(8)	5.1(1)
	2.850(3)		11.58(3)		166(8)	4

Table 5.3: High pressure structural parameters for annealed and *as prepared* $\text{Fe}_{0.5}\text{Co}_{0.5}$ and for $\text{Fe}_{0.4}\text{Co}_{0.6}$. The bold values have been fixed in the fit.

compare the results, our fits were performed both by fixing K'_0 to 4 and letting it free. We found that while the ambient volume parameter is almost unaffected by this choice, some appreciable change can be found in the bulk modulus. The a^{bcc} parameter, the c/a ratio of the P-induced hcp structure and the transition volume change ΔV obtained in the case of the annealed x=0.5 sample are in very good agreement with the lower Co % range behaviour, while this is not the case for the *as prepared* x=0.5 and x=0.6 samples. In fact, the samples used in the [259] were prepared by melting mixtures of pure component metal powders in multiple-hearth argon arc furnace and were also annealed [259, 260]. This evidence underlines the sensitivity of the structural properties to the preparation route.

Nevertheless the *as prepared* x=0.5 and x=0.6 samples reproduce the relative trend as a function of Co % (a major Co content correspond to larger a^{bcc} and $c/a(\text{hcp})$ and a smaller ΔV) if a rigid shift is considered. The bulk modulus values, obtained with $K'_0=4$ and K'_0 left free, fall in the error bar for the x=0.5 samples but not for the x=0.6 sample. The K_0 obtained for the x=0.5 annealed sample is not in trend reported by [259].

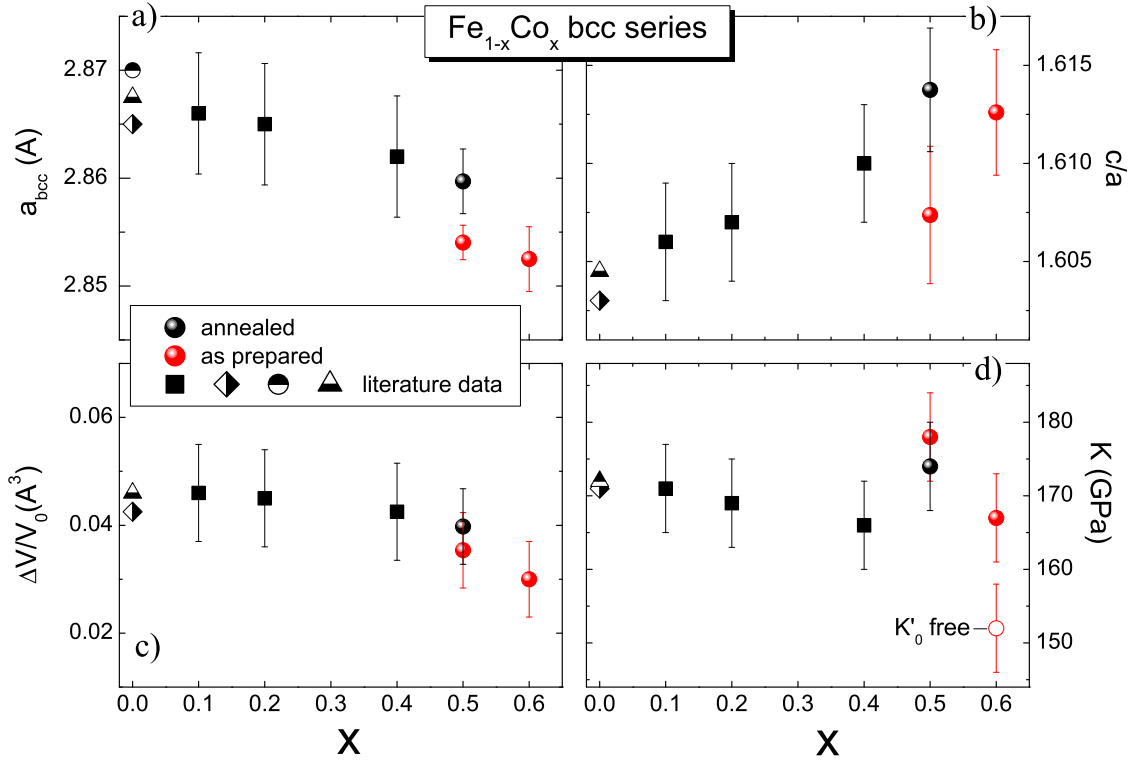


Figure 5.18: Structural ambient and high pressure parameters in $\text{Fe}_{1-x}\text{Co}_x$ for $0.5 \leq x \leq 0.75$: ambient a^{bcc} parameter (panel a), HP hcp structure c/a ratio (panel b), bcc-hcp transition volume change $\Delta V/V_0$ (panel c) and bulk modulus K_0 (panel d). Black and red full circles are from this work for annealed and *as prepared* samples respectively. For the bulk modulus plotted value are those obtained with the $K'_0=4$ approximation; for the $x=0.6$ also the value obtained leaving K'_0 free is shown. Black squares are from [259], half filled rhombus, triangle and circle are from [62, 274, 275] respectively.

The *as prepared* $x=0.5$ and $x=0.6$ samples reproduce the relative behavior as a major Co concentration corresponds to a smaller K_0 , however the rate of this decrease is higher than that indicated by data from [259]. Because this parameter is strongly constrained by the very low pressure range (0-10 GPa) we believe that our values should be more reliable, as only few pressure point were reported in the work by Papantonis and co-workers in that range.

Finally we plot the observed structural transition pressures in comparison with the previous literature data in Fig. 5.19. The reported existing data had been produced using different techniques: XRD [259], shock wave techniques [263] and electric resistance measurements [260, 261]. Once again our annealed data is in good agreement with literature data. In the *as prepared* $x=0.6$ sample the bcc-hcp structural transition occurs at a slightly higher pressure compared to the *as prepared* $x=0.5$ sample, indeed the transition pressure increase is much smaller than expected from the lower Co% data. In Fig. 5.18 we have shown that, apart from a rigid shift, the $x=0.5$ and $x=0.6$ samples well reproduce

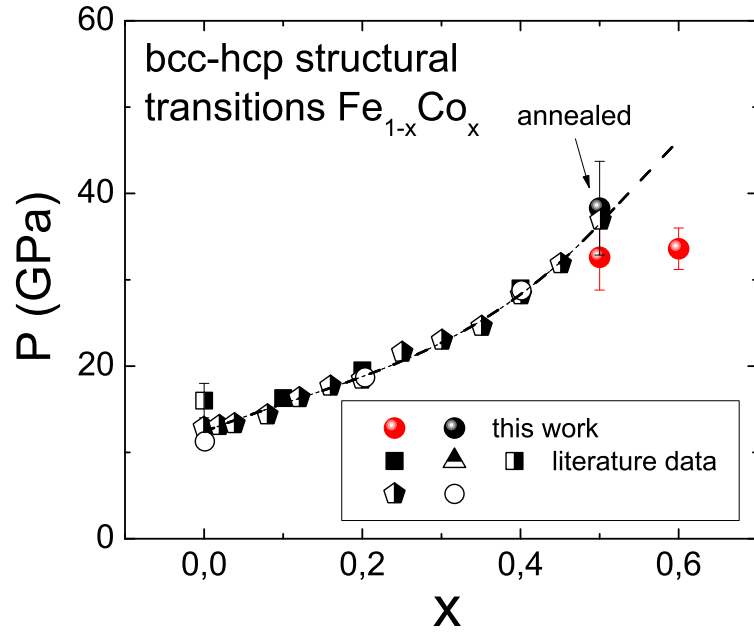


Figure 5.19: bcc-hcp transition in FeCo as a function of composition. Red full and empty circles are from this work; black squares are from [259]; half filled square, rhombus, triangle and pentagon are from [63, 260, 262, 263] respectively.

the lower Co concentration trend reported by XRD [259] for ambient and high pressure structural parameters with the exception of the bulk modulus K which is, however, the less reliable quantity reported by [259]. This fact suggests that the observed slope change may be not strictly related to the synthesis strategy but apply more generally to different kinds of samples.

$\text{Fe}_{0.25}\text{Co}_{0.75}$

$X=0.75$ is the limit concentration where the bcc symmetry starts to be unstable towards the hcp at ambient pressure [188, 226, 229]. Therefore, different regions of our film were analyzed by XAS out of the diamond anvil cell. XANES profiles from "bcc-like" to "hcp-like" shape were found even within few microns distance. Interestingly, the corresponding XMCD signals are different both in shape and intensity (an example is shown in Fig. 5.20); this evidence underlines the strong relation between magnetism and structure in the 3d metals.

High pressure combined XANES-XMCD measurements were performed at the Co (Fig. 5.21 panels a) and b)) and Fe (Fig. 5.21 panels c) and d)) K-edge at beamline ODE (SOLEIL). The ambient profile of the sample at the two edges is remarkably different, being "hcp-like" at the Fe K-edge and "bcc-like" at the Co K-edge. Indeed this difference must be attributed to the fact that the two edges were measured in two separate shifts with different charging (i.e. with different portion of the sample), since it was not possible

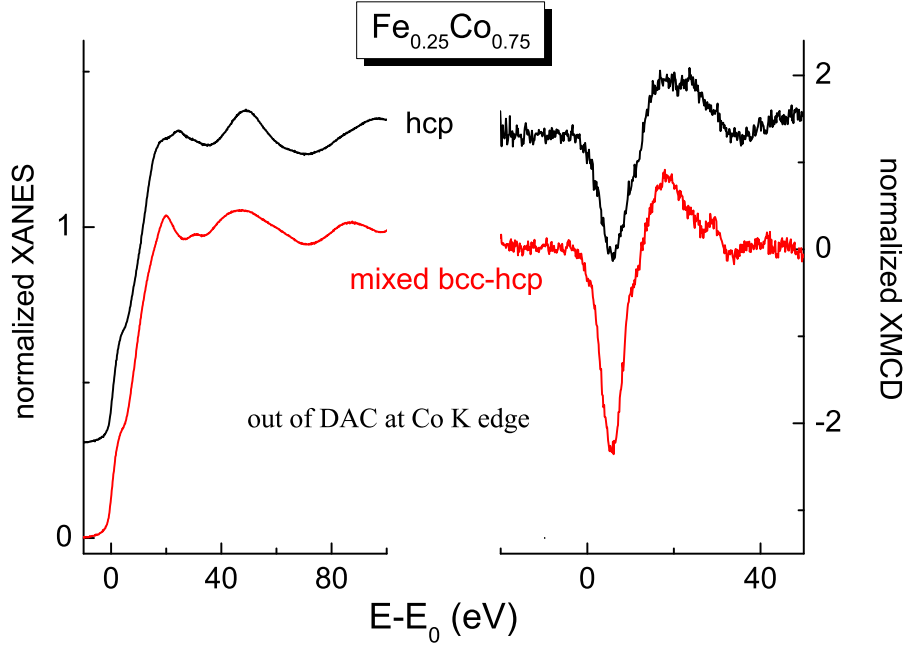


Figure 5.20: Left: Co K-edge XANES spectra of the $\text{Fe}_{0.25}\text{Co}_{0.75}$ sample foil in two different regions of the sample out of the DAC. Right: corresponding XMCD spectra.

to measure the same piece of sample simultaneously at the two edges. A fit of the ambient XANES spectra with a linear combination of bcc and hcp reference spectra reveals that the relative bcc-hcp symmetry fraction is 85% at for the sample measured at the Co K-edge and 54 % for the sample measured at the Fe K-edge.

At the Co K-edge, the bcc-like $\text{Fe}_{0.25}\text{Co}_{0.75}$ shows the evolution already encountered in samples $x=0.5, 0.6$. The change in feature *c* is seen from 21 GPa anticipating the total structural bcc-hcp transition which starts around 26 and is completed around 31 GPa. In the ambient Fe K-edge spectra, the *b* and *c* features shape can be associated to a "hcp-like" structure while the profile of *d* and *d'* is typical of the bcc symmetry. A transition to a pure hcp structure can however be recognized occurring at 26 GPa. The presence of a diamond glitch appearing around 26 GPa is signaled by short lines in the picture (Fig. 5.21 panel c)), to distinguish it from real oscillations.

In Fig. 5.22 we plot the pressure evolution of the XMCD main peak integral at Fe and Co K-edges. Even though the two data sets cannot in principle be compared, because the samples used at the two edges presented a different ambient bcc/hcp symmetry ratio, some general considerations can be given. In the 0-26 GPa pressure range a stronger linear decrease of the XMCD integral is observed at the Co K-edge; again this can be related to the XANES feature *c* modifications occurring prior to the bcc-hcp transition. A sharper decrease starts around 26 GPa for both edges, in correspondence with the hcp-bcc structural transition onset as seen by XANES, but suppression of the XMCD signal is reached before at the Co K-edge for the bcc-like sample (around 30 GPa) than at the Fe

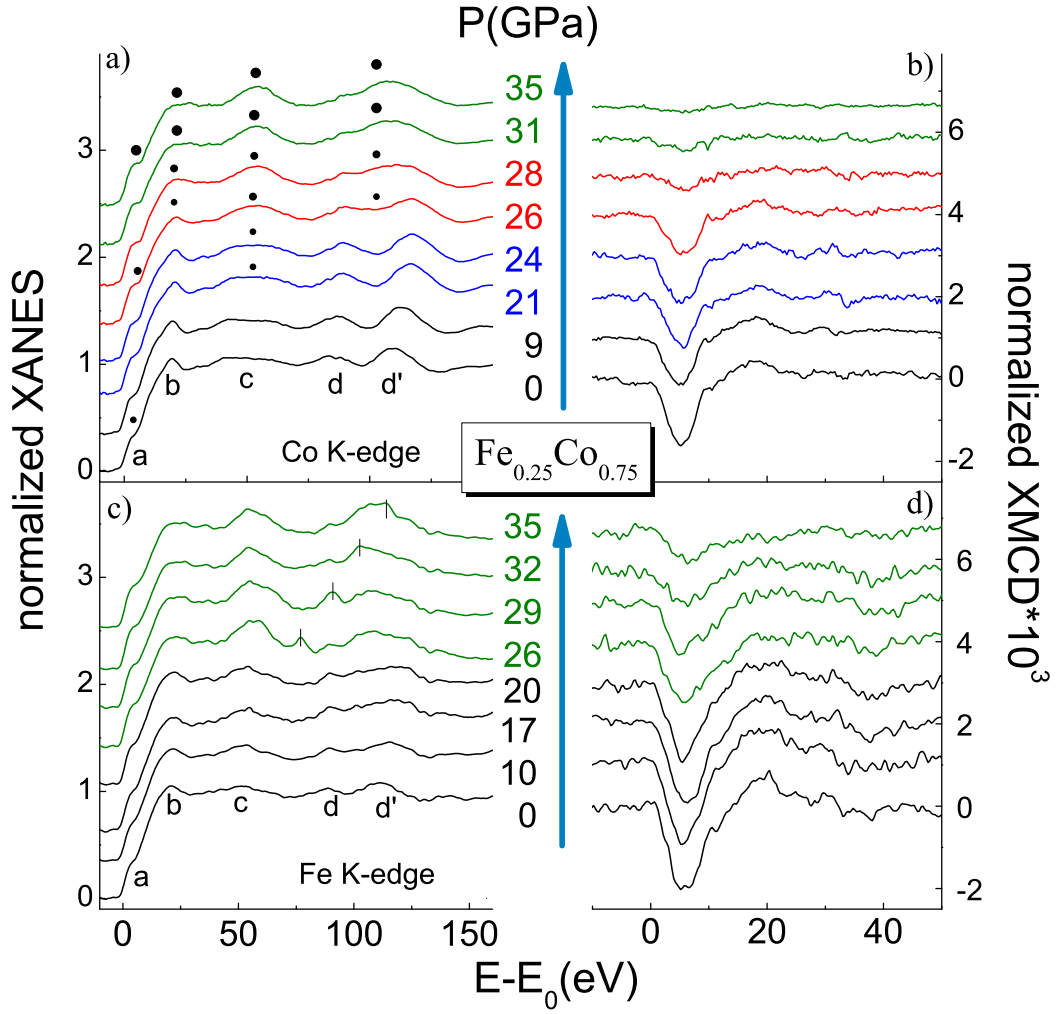


Figure 5.21: a) and b): normalized XANES and XMCD spectra of $\text{Fe}_{0.25}\text{Co}_{0.75}$ at Co K-edge; c) and d) normalized XANES and XMCD spectra of $\text{Fe}_{0.25}\text{Co}_{0.75}$ at Fe-K-edge. The presence of a diamond glitch is signaled by short lines in panel c).

K-edge for the hcp-like sample (around 40 GPa). At the Co K-edge, a residual signal of 5-10% could be observed well above the transition.

Because of the spatial inhomogeneity of the sample and the impossibility to perform simultaneous XRD and XAS measurements, comparison to XRD data could not be discussed. However, in the $x=0.5$ and 0.6 sample we observed that the sharp decrease of the XMCD signal corresponds to the bcc-hcp global (long range) structural transformation. Assuming that this also applies to the $x=0.75$ sample, the data in Fig. 5.22 indicate that the bcc-hcp transition occurs at a higher pressures in hcp-like samples, i.e. that the hcp structure furnish a major resistance to pressure. This is in agreement with the general behavior of the $3d$ metals as bcc iron loses its ferromagnetism at much lower pressure (≈ 13 GPa) than the closed packed arranged metals Co and Ni (120 GPa and above 400 GPa (estimated) respectively).

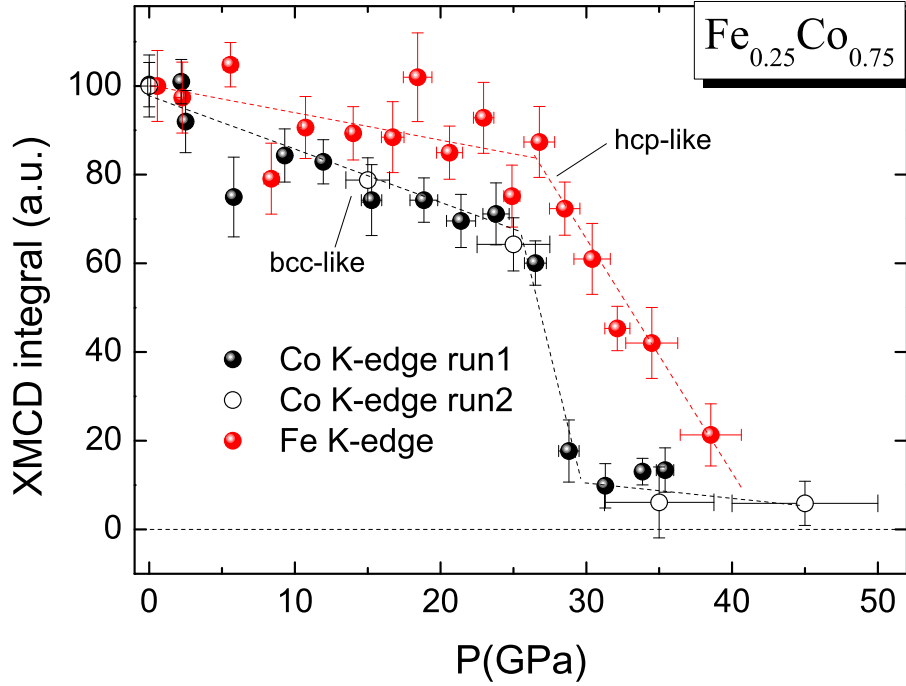


Figure 5.22: Pressure evolution of the XMCD integral of $\text{Fe}_{0.25}\text{Co}_{0.75}$ at Fe (red full circles) and Co K edges (black full and empty circles)

Despite the complexity due to the bcc/hcp mixing in the $\text{Fe}_{0.25}\text{Co}_{0.75}$ sample, the collected data allow to identify a pressure range in which the P-induced magnetic and structural transition should be placed.

The FeCo bcc series

In this section we summarize the results obtained for magnetic and structural transitions in the FeCo bcc series, for $0.5 \leq x \leq 0.75$.

In Fig. 5.23 we plot the pressure evolution of the XMCD signal integral of $\text{Fe}_{1-x}\text{Co}_x$ for $0.5 \leq x \leq 0.75$ at the Co K-edge (upper panel) and for $x=0.5, 0.6$ at the K-edge Fe (power panel) K-edge. Due to the hcp-like symmetry of the $x=0.75$ sample measured at the Fe K-edge, it cannot be compared with the other samples.

The behavior of the XMCD integrals under pressure can be divided into two regions: a first initial smooth decrease corresponding to local bcc-hcp distortions only visible in the XANES and a sharper decay up to total suppression (magnetic transition) which corresponds to the long range bcc-hcp structural transition as seen by XRD. In all the analyzed samples the pre-transition effects appeared stronger at the Co K-edge, with the only exception of the $x=0.6$ sample in which the XMCD signal initial decay was found to be the same at both edges, within the error bars.

In Fig. 5.24 we plot the structural and magnetic transition pressures as a function of composition. The symbols indicate half way of the transition and the error bars indicate

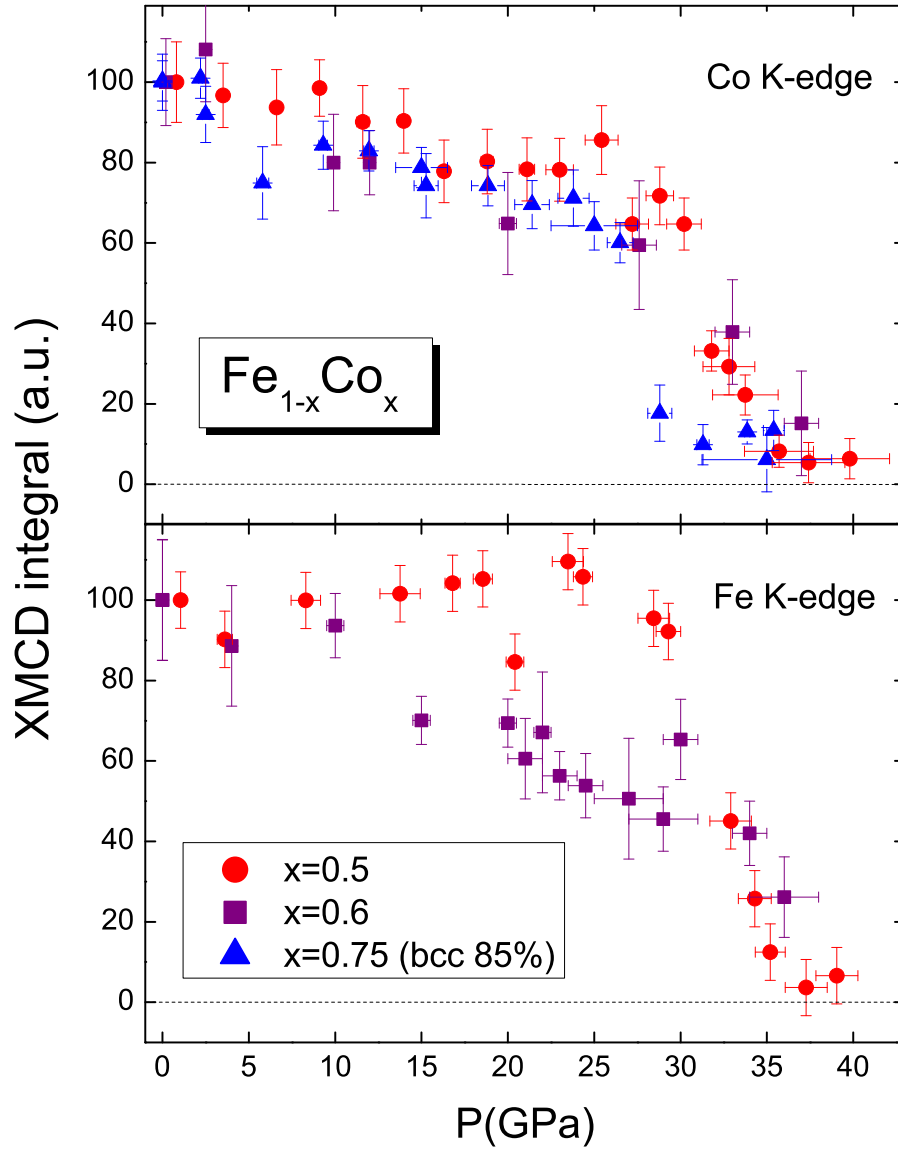


Figure 5.23: Pressure evolution of the XMCD integral of $\text{Fe}_{1-x}\text{Co}_x$ for $0.5 \leq x \leq 0.75$ at Co K-edge (upper panel) and for $x=0.5; 0.6$ at Fe K-edge (lower panel). $x=0.5; 0.6; 0.75$ are red circles, purple squares and blue triangles respectively.

the transition range. In the $x=0.5$ and $x=0.6$ samples the magnetic transitions occur simultaneously at the two edges and in correspondence to the structural transition, within the error bar. Globally, the magnetic/structural transition in the $x=0.6$ sample occurs at a slightly higher pressure with respect to the $x=0.5$ (not annealed) sample, however, with respect to the lower Co% trend reported in the literature [259], some tendency to saturation is observed (see Fig. 5.19). In the $x=0.75$ sample the magnetic transition of a bcc-like sample occurs at lower pressures (26-30 GPa). Although this could not be observed at both edges, it is quite reasonable to assume that it would occur at the same pressure, as we discussed in the previous section. This lower transition pressure can be related to

the higher number of Co-Co homopolar bonds in this sample, as we will show in the next section.

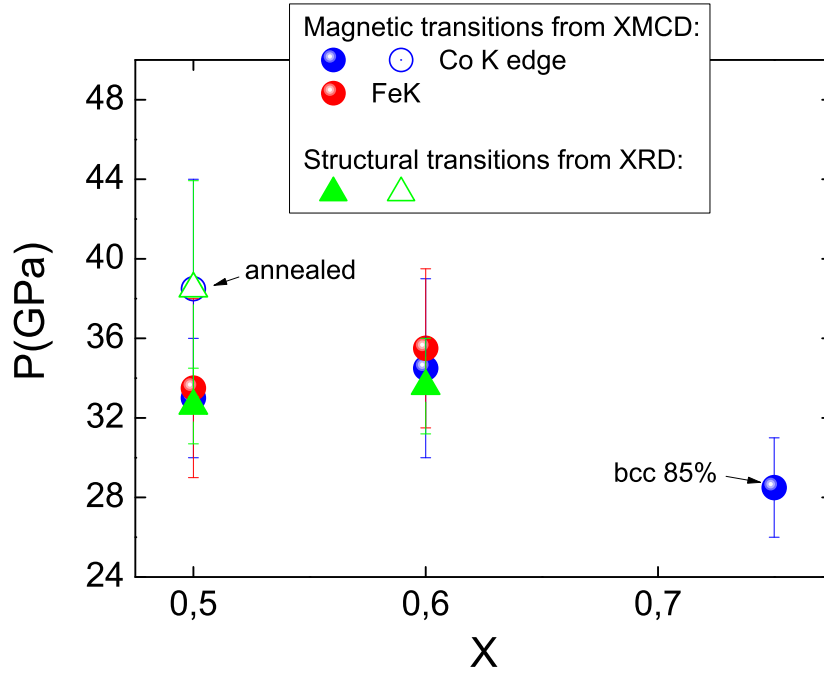


Figure 5.24: Magnetic and structural transitions in $\text{Fe}_{1-x}\text{Co}_x$. Full and empty green triangles are from XRD data, blue full and empty circles are from XMCD data at the Co K-edge and red full circles are from XMCD data at the Fe K-edge. The symbols indicate half way of the transitions and the error bars indicate the transitions range.

Order and disorder

As already discussed, nearly equiatomic FeCo samples are found in an ordered CsCl structure, while disordered samples can only be obtained with very fast cooling. This is also confirmed by theoretical calculations which show the bcc CsCl phase to be the most favorite one for concentration around $x=0.5$ (see for example [276]). Ordering increases the lattice parameter (Fig. 5.2 right panel) and the saturation magnetization (Fig. 5.4 right panel) but does not strongly affect their variation with composition.

In order to shed light on the role played by the ratio between the homopolar (FeFe and CoCo) and heteropolar (FeCo) bonds on the high pressure structural and magnetic properties in FeCo, DFT total spin calculations were performed by Dr. L. Genovese (from the ESRF Theory group) using the VASP package [277]. In the *Results and discussion* section of the *Nickel* chapter we discussed how the high pressure K-edge XMCD trend in nickel is related to that of p-projected orbital moment rather than to that of the total spin moment. However, in the case of iron, total spin magnetization calculations well reproduce the K-edge XMCD behavior under pressure [43, 45]. Due to the similarities between pure Fe and the FeCo system this should also apply to the iron-cobalt alloys. Moreover, spin

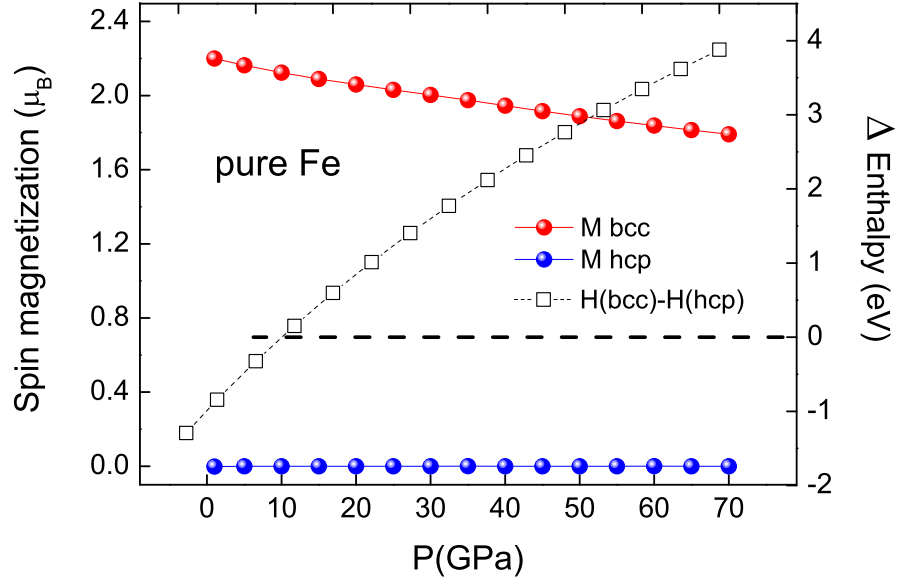


Figure 5.25: Total spin magnetization calculation as a function of pressure for the Fe in bcc symmetry (red full circles) and hcp symmetry (blue full circles); reference scale for total spin magnetization is on the left axis. Empty squares represent the difference in enthalpy between the bcc and hcp structures; its reference scale is on the right axis.

calculations are however expected to properly describe the transition pressure region, since orbital and spin terms are suppressed at the same time.¹

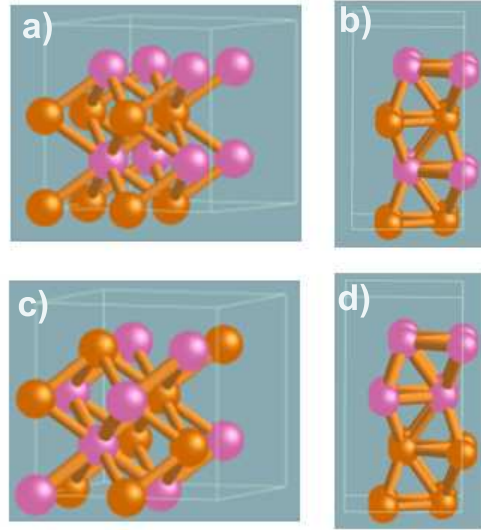


Figure 5.26: a): CsCl structure for $\text{Fe}_{0.5}\text{Co}_{0.5}$ and corresponding hcp structure (b). c): Zintl structure for $\text{Fe}_{0.5}\text{Co}_{0.5}$ and corresponding hcp structure (d).

¹We are currently working in cooperation with the ESRF Theory group to complete the comparison between high pressure K-edge XMCD measurements and high pressure orbital (so far missing in the literature) and spin moments calculations for all the 3d metals in order to shed light on the observed differences.

The Projector Augmented Wave method was used, with Perdew Burke Ernzerhof exchange correlation approximation [221]. Calculations were performed with a supercell of 16 atoms, such as to test different atomic configurations. An 800 eV energy cutoff was chosen to ensure convergence with respect to the basis set, together with a k-point sampling equivalent to a length of 40 a.u. The enthalpy was used as a criterion to establish the most convenient structure as a function of the pressure. Magnetization around atoms was measured within a Wigner-Seitz radius of 1.3 Å.

A preliminary test was performed on pure iron and reported in Fig. 5.25. Under compression, the spin magnetization for the bcc phase (M bcc, in red full circles) decreases smoothly from its ambient value ($2.2 \mu_B$) while the spin magnetization for the hcp phase (M hcp, in blue full circles) is zero in the whole pressure range. The bcc-hcp enthalpy difference ($H(\text{bcc}) - H(\text{hcp})$) in empty squares, reference scale on the right axis) changes sign around 11 GPa indicating that Fe undergoes a transition from the FM bcc to the NM hcp at this pressure in agreement with previous calculations and experiments [63, 71, 88, 93, 95, 100–102, 274].

To describe order and disorder in equiatomic FeCo we considered the ordered CsCl structure, characterized by each atom being coordinated with 8 atoms of the other type, and the Zintl structure characterized by each atom being coordinated with 4 atoms of the same type and 4 of the other type. The two structures and corresponding hcp structures are represented in Fig. 5.26. The comparison between the calculated enthalpies for the different structure confirms that the bcc ordered phase (CsCl) is the most favorite at ambient pressure (Fig. 5.27).

Assuming, as a first approximation, that chemical transitions would not be induced by the application of pressure, the expected transition for the ordered and disordered phases are described in Fig. 5.28. The ambient magnetization for the bcc ordered (CsCl) phase is higher than for the disordered (Zintl) phase, in agreement with previous theory and experiments [23, 246]. In the ordered CsCl structure the bcc magnetization decreases smoothly until the non magnetic hcp phase becomes favorite around 34 GPa; the structural/magnetic transition occurs exactly like in iron but at higher pressure. In the disordered Zintl structure the difference in enthalpy between bcc and hcp structure is smaller and the transition becomes sluggish: the hcp phase is favorite at 20 GPa and preserves a non-zero magnetism up to 70 GPa. The higher resistance to compression of the ordered structure is in agreement with our observations on the annealed sample, as the major degree of chemical order produced by the annealing pushes the transition to higher pressures. Differently from the ambient structural and magnetic properties, these findings point out that the chemical order - i.e. the ratio between homopolar and heteropolar bonds - plays a crucial role in tuning the high pressure magnetic and structural response.

The comparison with experimental results confirms that the nearly equiatomic samples $x=0.5, 0.6$ that we analyzed are all quite chemically ordered - i.e. they maximize the number of heteropolar bonds - as the bcc ferromagnetic to hcp non ferromagnetic transition

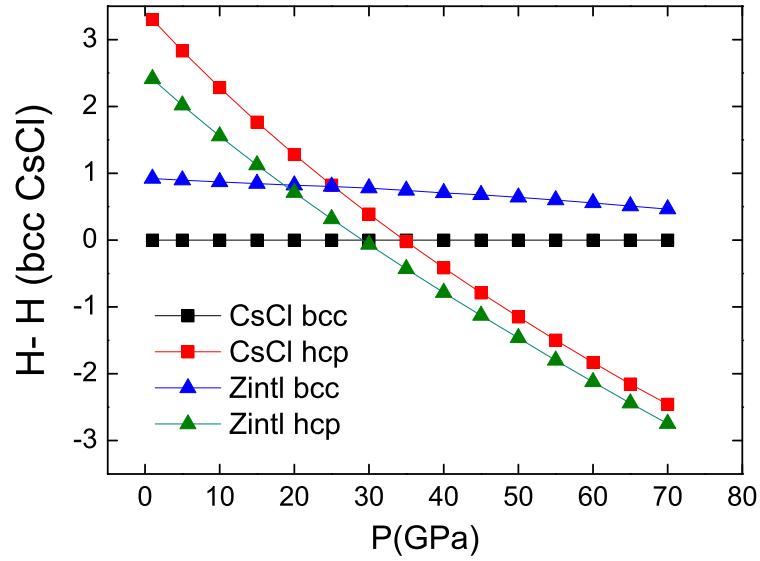


Figure 5.27: Calculated enthalpy differences for the ordered CsCl hcp phase (red squares) and disordered Zintl phases (bcc and hcp in blue and green triangles respectively) with respect to the ordered CsCl phase (in black squares).

in these samples was observed in the 30-40 GPa range. Interestingly, the pressure at which the hcp symmetry becomes favorite (20 GPa) in the calculated disordered Zintl structure corresponds to the observed onset of local bcc-hcp distortions, suggesting that these precursor transformation could be related to the presence of a small amount of chemical disorder in the samples (already present at ambient conditions). In the previous section we noted that these pre-transition effects are more evident at the Co site. Fig. 1.7 in Chap. 1 points out that the magnetization density around Co is rather asymmetric. Now, if a small number of Co-Co homopolar bonds - i.e. a certain degree of chemical disorder - is present, a major magnetic instability to compression is expected around the Co site giving rise to associated local distortions.

In the $x=0.75$ sample, if the Fe_3Al structure proposed by Schwarz and co-workers is assumed, the average number of heteropolar bonds reduces to 5. In fact in this structure, each Fe atoms is surrounded by 8 Co atoms, and two crystallographically inequivalent Co sites exist, one entirely surrounded by Co and the other with 4 Fe and 4 Co neighbors (Fig. 5.5). This situation is quite similar to the calculated Zintl structure for the $x=0.5$ concentration where the number of heteropolar bonds amounts to 4 (see Table 5.4), which explains the lowering of the transition pressure and the observation of a residual signal up to above 40 GPa in the $x=0.75$ sample.

In summary the increasing number of Co-Co homopolar bonds on going from $x=0.5$ to $x=0.75$ would be responsible for the initial bcc-hcp distortions and smooth decrease of the XMCD signal in nearly equiatomic samples ($x=0.5, 0.6$) and a lowering of the transition pressure in the $x=0.75$ sample. This simple model which correlates the high pressure magnetic and structural properties of the studied FeCo alloys to their chemical order

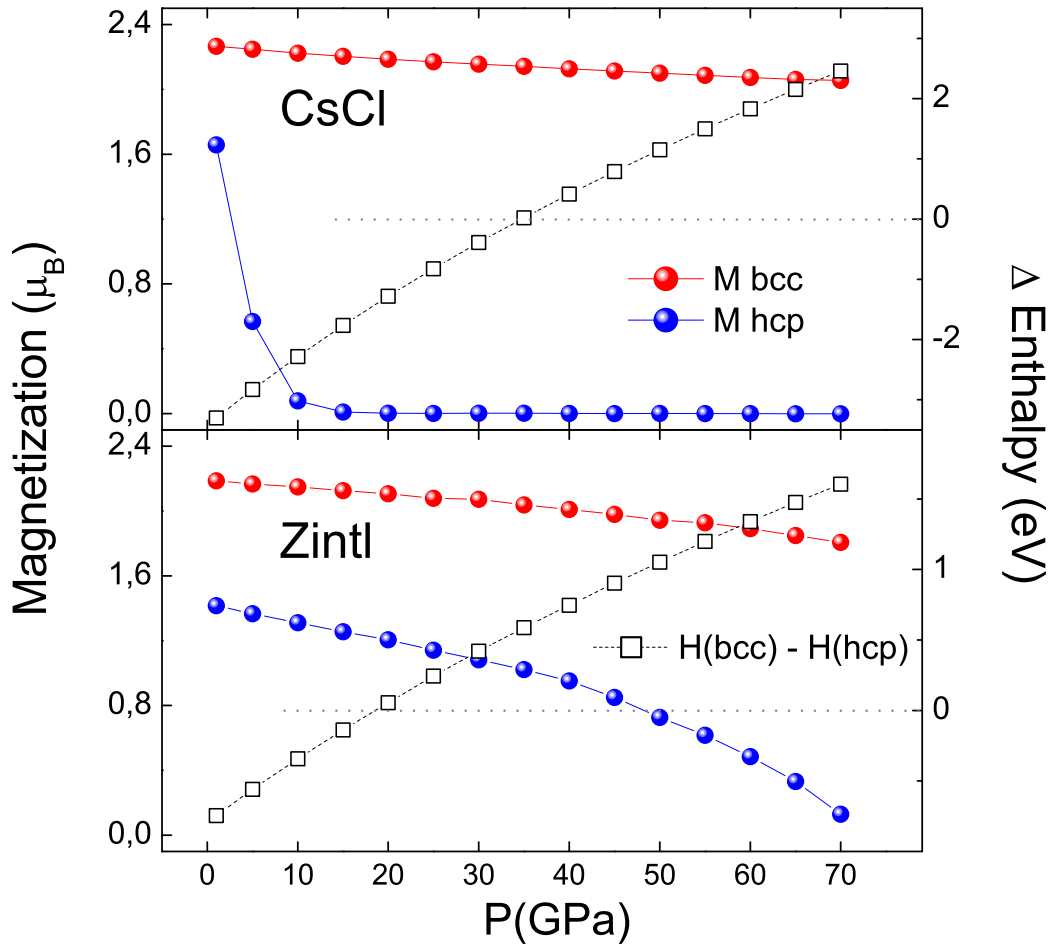


Figure 5.28: Upper panel: total spin magnetization calculation as a function of pressure for the $\text{Fe}_{0.5}\text{Co}_{0.5}$ CsCl structure in bcc symmetry (red full circles) and corresponding hcp symmetry (blue full circles); Bottom panel: the same for the Zintl structure. The reference scale for total spin magnetizations is on the left axis. In both panels empty squares represent the difference in enthalpy between the bcc and hcp structures; the corresponding reference scale is on the right axis.

allows to explain the main details of the experimentally observed behaviors. It however presents some shortcomings: i) it does not explain why the structural/magnetic transition in the $x=0.6$ sample is more sluggish (at both edges) than in the 0.75 sample and ii) why its complete (long range) transformation into hcp non-ferromagnetic does not occur at a lower pressure compared to the $x=0.5$ sample.

In order to clarify these points, further theoretical study is envisaged by the ESRF Theory group to precisely account for all the studied concentrations, including elementary moments predictions (separated Fe and Co contribution) and orbital moments terms.

In the discussion above we have neglected the possible occurrence of pressure induced chemical transitions while Fig. 5.27 indicates that the hcp disordered phase is favorite with respect to the hcp ordered one at high pressure, which would thus be a metastable phase.

Heteropolar bonds in $\text{Fe}_{1-x}\text{Co}_x$		
x=5	CsCl	8
	Zintl	4
x=0.75	Co_3Al	5

Table 5.4: Average heteropolar bonds in $\text{Fe}_{1-x}\text{Co}_x$ for the structures proposed in [23].

However, the transition from bcc ordered to hcp disordered looks unlikely, first because the disordered hcp phase is expected to be still quite magnetic while in our sample only a residual signal was observed; secondly it would require sufficient energy to break 4 bonds and remove 4 nearest neighbors. Nevertheless this scenario cannot in principle be ruled out and another development of this study will be to precisely analyse if the condition at which the system has been probed (high pressure, ambient temperature) would allow, from an energetical point of view, a structural-chemical transition.

$\text{Fe}_{0.1}\text{Co}_{0.9}$

High pressure combined XANES-XMCD measurements were performed for the $\text{Fe}_{0.1}\text{Co}_{0.9}$ sample at the Co K-edge at beamline ID24 (ESRF) (Fig. 5.29). The ambient XANES profile is typical of the fcc symmetry [63–65, 206] and resembles that of pure Nickel (see the *Nickel* chapter). The XANES evolution under pressure involves the intensity enhancement of the pre-edge shoulder *a*, the inversion in the relative height of the "white line" features *b* and *b'*, the intensity increase of the first oscillation *c* and its movement to higher energies. Diffraction confirmed a stable fcc structure (see Fig.5.30) in the whole pressure range of study. Therefore, like in the Nickel case, the observed XANES transformations result from simple compression.

Simultaneous XMCD measurements (Fig. 5.29 right panel) show that the Co K-edge XMCD signal decreases with pressure and is extinguished before 70 GPa. This pressure is remarkably low with respect to pure Co in which the ferromagnetic to non-ferromagnetic transition occurs around 120 GPa (see the *Cobalt* chapter) [64]. Fe impurities addition to Co thus strongly influences the high pressure magnetic response. The Co sensitivity to Fe impurities is also evident in the structural instability characteristic of the low Fe% range (0-10%) where fcc, hcp and d-hcp (double-hcp) structures are encountered [230]. In Fig. 5.31 right panel we plot the pressure evolution of the XMCD main peak integral. A constant value is observed within the error bar up to around 30 GPa where a continuous linear decrease starts up to total suppression.

Two sets of diffraction measurement were performed: up to 50 GPa (set1) and up to 70 GPa (set 2). The ambient phase of $\text{Fe}_{0.1}\text{Co}_{0.9}$ was found to be fcc (γ) with some features belonging to the hcp (ϵ) symmetry. Traces of the ϵ (100) and (101) reflections have been indicated in the ambient spectrum of Fig.5.30; the ϵ (002) and γ (111) reflections

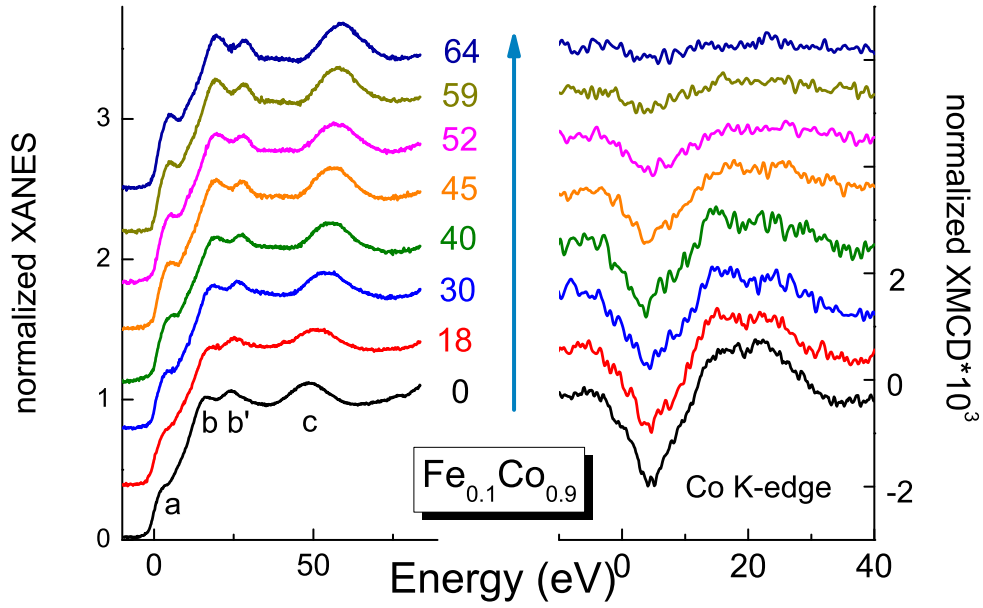


Figure 5.29: High pressure combined XANES (left panel) and XMCD (right panel) of $\text{Fe}_{0.1}\text{Co}_{0.9}$ at the Co K-edge.

are superimposed. Rietveld analysis [267] reveals that the hcp/fcc phase fraction amounts to 1-10% and is retained up to the highest pressure reached (72 GPa).

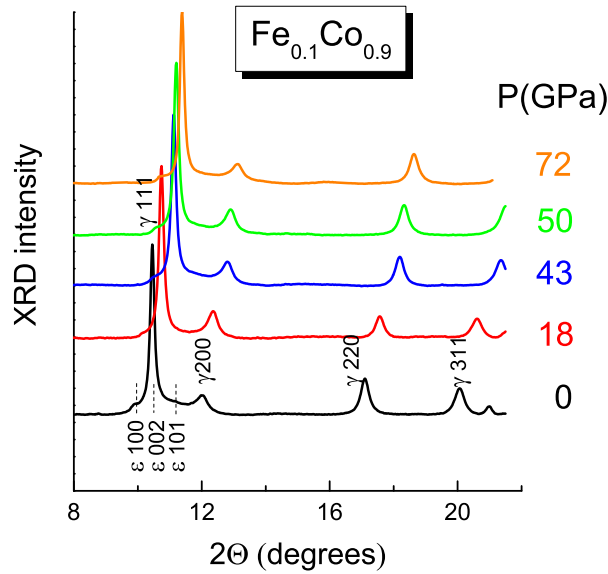


Figure 5.30: Selection of XRD patterns of $\text{Fe}_{0.1}\text{Co}_{0.9}$ as a function of pressure. Reflections from fcc (γ) and hcp (ϵ) $\text{Fe}_{0.1}\text{Co}_{0.9}$ are indicated.

This fact is responsible for a larger error in the lattice parameter a^{fcc} since the phase coexistence gives rise to interfacial strain; also, the superimposition of reflections belonging to different phases hinders a precise determination of a^{fcc} . Therefore, in order to account for possible errors in the Le Bail fitting, a^{fcc} was also evaluated from the d -spacings

individually determined.

The fcc lattice parameter was found to be $a^{fcc}=3.550\pm0.005$. In Fig. 5.31 left panel we plot the compression curves obtained in the two data sets. Interestingly, an isostructural transition with volume change $\Delta V/V_0=0.007$ is observed after 30 GPa in correspondence to the onset of the magnetic transition. This finding suggests that the isostructural transition is actually induced by the magnetic instability following compression. In the field of P-induced structural-magnetic transitions, an intense debate is still open to establish whether the loss of magnetic moment in the metal is the driving force or simply a consequence of the structural transition. A driving role of magnetism has been already proposed in the case of pure Fe by Mathon and co-workers [93]. The total suppression of ferromagnetism occurs at higher pressure (≈ 70 GPa) in the domain of the P-induced lower volume fcc structure. This result confirms the fcc structure to be the most stable symmetry in the ferromagnetic 3d metals as only an isostructural transition could be obtained by compression. To the best of our knowledge no structural transition has been ever observed starting from the fcc structure in any metal under compression.

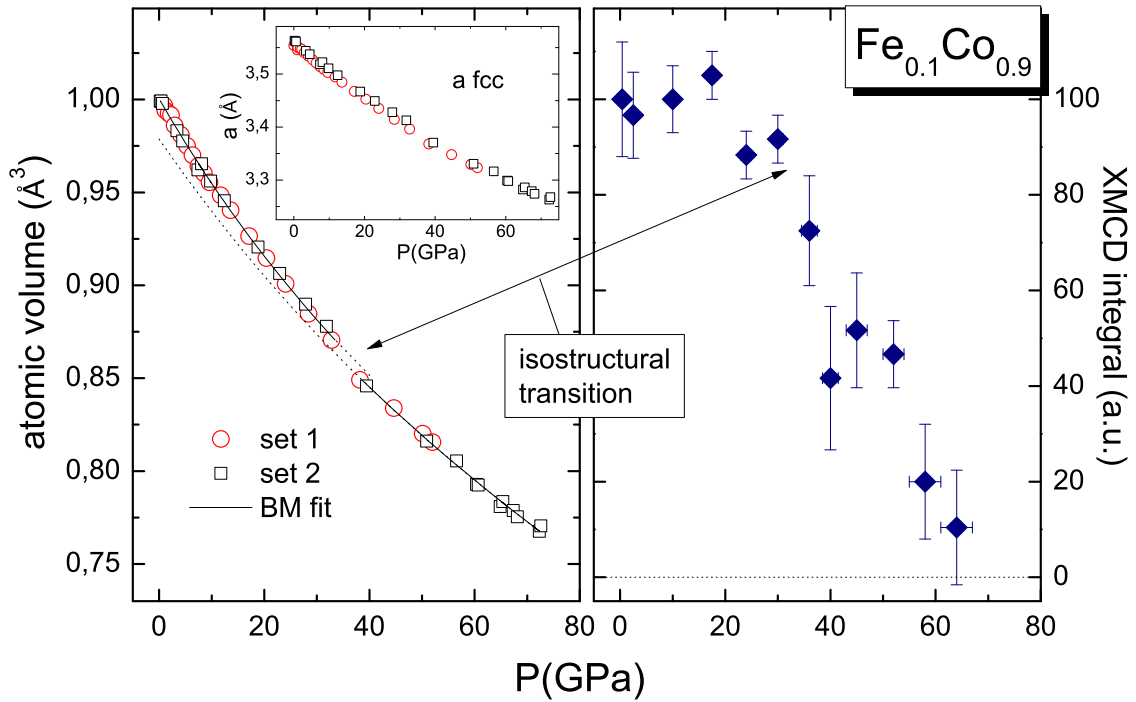


Figure 5.31: Left: Compression curve of $\text{Fe}_{0.1}\text{Co}_{0.9}$. The uncertainties on volume and relative pressure are smaller than the symbols. The solid line is a Birch-Murnaghan fit to the experimental data. Inset: pressure evolution of the lattice parameter. Right: Pressure evolution of the main XMCD peak integral.

The two branches of the compression curve were fitted to a third order Birch-Murnaghan EOS to compute the ambient volume V_0 , the bulk modulus K_0 and its derivative K'_0 . Results are shown in Table 5.4. If the K'_0 parameter is left free, the compressibility of the low pressure (LP) fcc phase in $\text{Fe}_{0.1}\text{Co}_{0.9}$ is the same of that of hcp Co and the compressibility

of the high pressure (HP) fcc $\text{Fe}_{0.1}\text{Co}_{0.9}$ phase is similar to that of fcc Co.

Sample	structure	V_0 ($\text{\AA}^3/\text{atom}$)	K_0 (GPa)	K'_0	source
$\text{Fe}_{0.1}\text{Co}_{0.9}$	LP fcc	11.34(3)	201(6)	2.7(1)	this work
	LP fcc	11.31(3)	182(6)	4	this work
	HP fcc	11.0(1)	233(10)	2.4(1)	this work
Co	hcp	11.00	199	3.6	[61]
	fcc	10.33	224	5.8	[61]

Table 5.5: Compression parameters of $\text{Fe}_{0.1}\text{Co}_{0.9}$ obtained from fit to Birch-Murnaghan EOS. Data for pure Co are from [61]. Numbers in bold have been fixed.

From Fe to Co

In this section we summarize all the results obtained for structural and magnetic transitions in $\text{Fe}_{1-x}\text{Co}_x$ in the studied composition range ($0.5 \leq x \leq 1$) and compare them with literature data for FeCo in lower concentration range ($0 \leq x \leq 0.4$), pure Fe and pure Co.

In Fig. 5.32 we compare the pressure evolution of the Fe K-edge XMCD integral in $\text{Fe}_{1-x}\text{Co}_x$ as a function of composition with that of pure iron. Co addition to Fe pushes the magnetic transition to higher pressures and enlarges the transition width. In the metals a major resistance of ferromagnetism to compression is generally associated to the ambient strong ferromagnetism (filling of the majority band) [42, 63]. The enhanced stability of FM in the bcc $x=0.5, 0.6, 0.75$ samples with respect to pure Fe, is thus in agreement with bcc bands calculations [23] which predict $\text{Fe}_{1-x}\text{Co}_x$ to be a strong ferromagnet for $x \geq 0.3$.

In Fig. 5.33 the pressure evolution of the Co K-edge XMCD integral in FeCo as a function of composition with that of pure cobalt is compared. With respect to cobalt, whose K-edge XMCD integral decrease is linear, the $x=0.5, 0.6, 0.75$ samples present a step-like suppression of the Co K-edge XMCD signal - characterized by an initial slow linear decrease followed by a sharper decay in the 30-40 GPa region - rather similar to the pure iron trend. Interestingly, the fcc $x=0.9$ sample preserves the kink in the XMCD reduction around 30 GPa but the following drop rate is smoother, roughly resembling that of pure Co.

The compression curves of the analyzed FeCo samples are included between those of pure Fe and pure Co, as shown in Fig. 5.34. In the low compression region the compressibility of the $x=0.5$ and $x=0.6$ samples is similar to that of pure Fe but they present a lower volume change at the bcc-hcp transition. The compression curve of the fcc $x=0.9$ sample is similar to that of pure cobalt at low pressure. It is worth noticing that the isostructural volume change in sample $x=0.9$ occurs in the same pressure region of the bcc-hcp transition onset for the $x=0.5, 0.6$ samples meaning that, despite the different

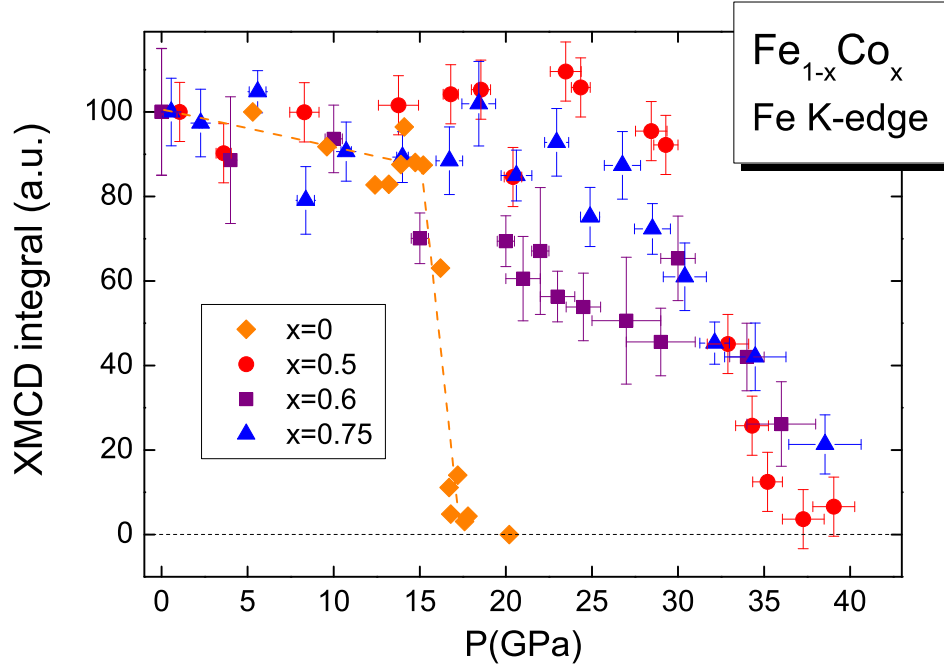


Figure 5.32: Pressure evolution of the Fe K-edge XMCD integral in FeCo as a function of composition.

ambient structure, the fcc $x=0.9$ sample maintains some common features with the bcc FeCo series also from the structural point of view.

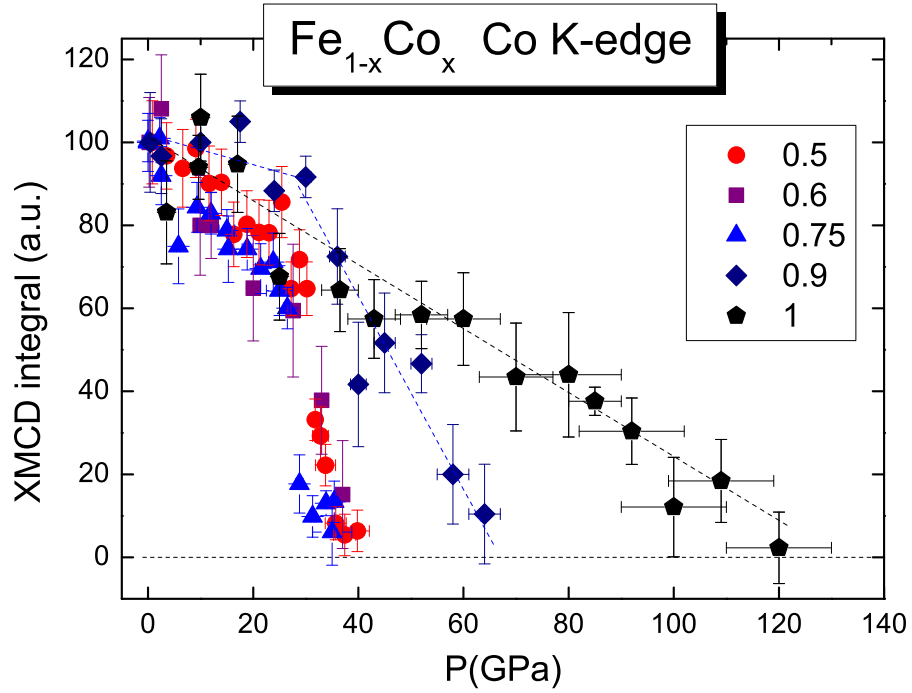


Figure 5.33: Pressure evolution of the Co K-edge XMCD integral in FeCo as a function of composition.

In Fig. 5.35 we plot the ambient and compression parameters of FeCo. If a rigid shift between the annealed and not-annealed samples is taken into account, a rather continuous decreasing behavior of both atomic ambient volume (V_0) and volume change at the structural transition ($\Delta V/V_0$) can be recognized in the complete FeCo series, from pure iron to pure cobalt. Even though jumps are expected at the boundaries between different structures (bcc, hcp, fcc), this evidence suggests that structural ambient and high pressure parameters in FeCo are mainly determined by the composition.

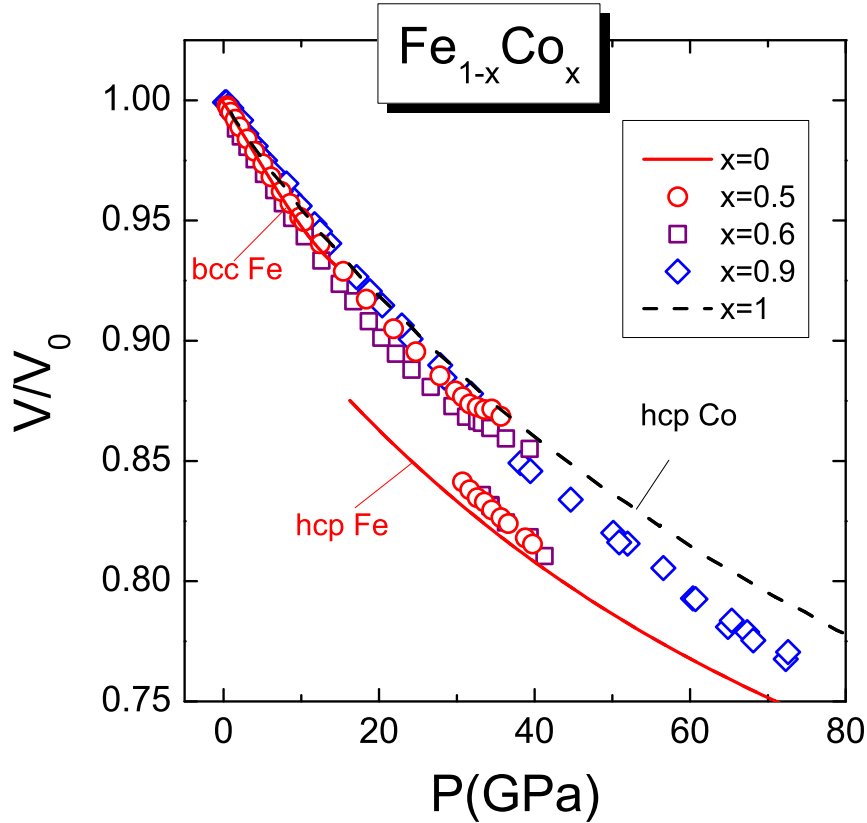


Figure 5.34: Compression curves of FeCo as a function of composition.

For the bulk modulus both values obtained by fixing K'_0 to 4 and leaving it free were calculated. While they are within the error bar for the $x=0.5$ samples this is not the case for the $x=0.6$ and $x=0.9$ samples, indicating that the approximation used by Papantonis and co-workers [259] is no longer valid in the high Co concentration range. A more complex behavior is observed for K_0 : the smooth linear decrease in the low Co% range is followed by a slope inversion in the higher Co content range with K_0 increasing up to the maximum value of pure Co. However, an anomalous high value is found for the $x=0.5$ sample (both *as prepared* and annealed sample) maybe related to the long range CsCl order expected at this concentration, and some variation is reported in the pure cobalt literature values. Indeed further XRD HP data are needed in the 50%-100% Co range to precisely determine the bulk modulus behaviour as a function of Co content.

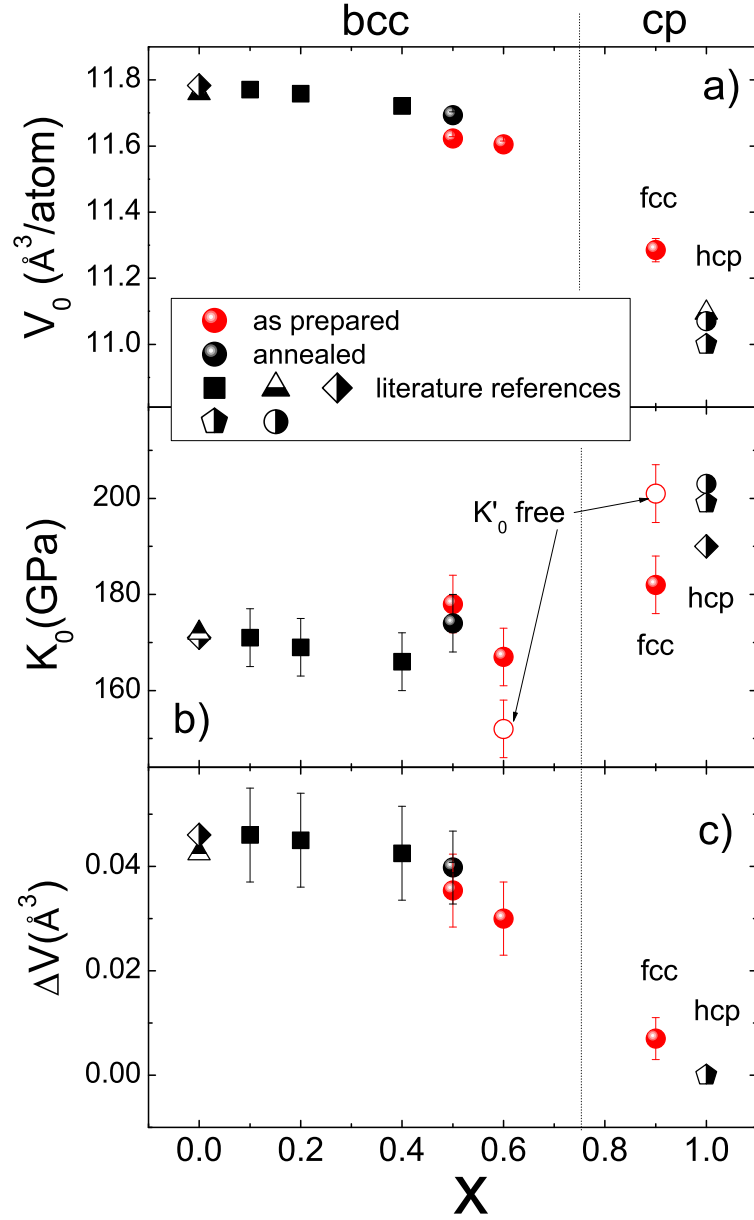


Figure 5.35: a) ambient atomic volume (V_0), b) bulk modulus (K_0) and c) volume change ($\Delta V/V_0$) in FeCo as a function of composition. Circles are from this work: black is for the annealed sample, red is for the *as prepared* samples. In panel b) full circles are K_0 obtained fixing K'_0 to 4 and empty circles are values obtained with K'_0 free. Black full squares are from [259]; half filled triangles, pentagons, rhombus and circles are from [62], [61], citeBasset, and [166] respectively.

A summary of structural and magnetic transitions in FeCo is reported in Fig. 5.36. In the left panel the structural transition pressures observed by XRD and analogous literature data are reported. The scatters represent half way of the transition and error bars represent the transition width. In the right panel the pressures for total suppression of

ferromagnetism as seen by XMCD are shown. The represented data are chosen as the maximum zero signal pressure obtained between Co and Fe K-edge. The scatters represent the end of the magnetic transition while continuous lines and dash lines represent its width. The structural and magnetic transition pressure in the bcc series increases with Co content with some tendency to saturation after $x=0.5$. In the $x=0.9$ sample the iso-structural fcc transition is still found in the saturation plateau while the moment suppression is placed half way between that of the $x=0.75$ and the $x=1$ samples.

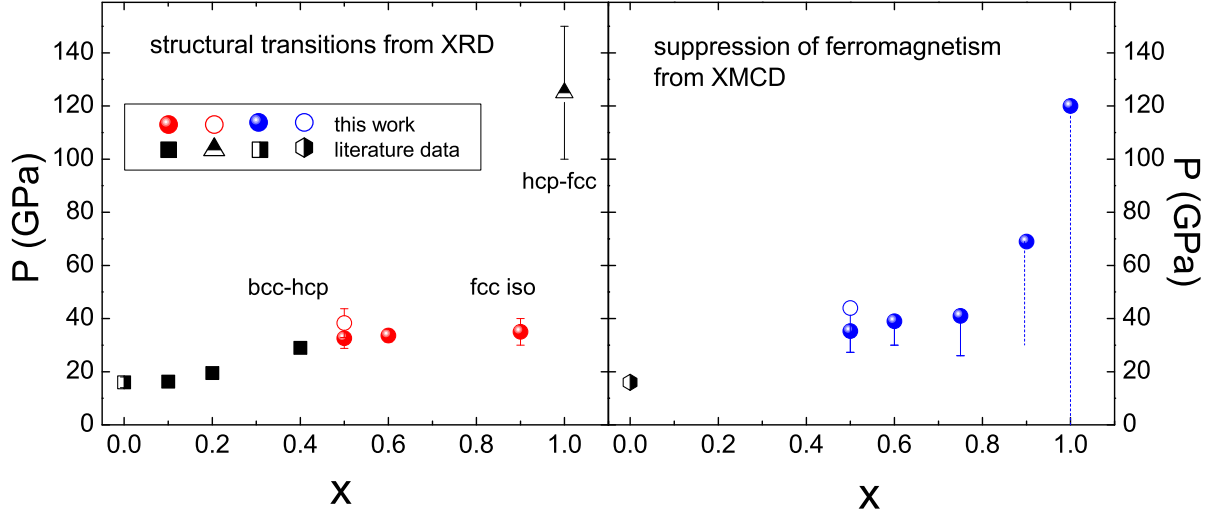


Figure 5.36: Left: Structural transitions pressure in FeCo as seen by XRD as a function of composition. The scatters represent half way of the transition and error bars represent the transition width. Right: suppression of ferromagnetism as seen by XMCD. The scatters represent the end of the transition while continuous lines represent its width. Full circles are from this work (empty circles are for the annealed sample); black full squares are from [259]; half filled triangles, pentagons and squares are from [61], [93] and [63] respectively.

In the pure 3d metals, it was observed [42, 63] that the pressure of ferromagnetism suppression relates inversely to the ambient magnetic moment, i.e. the lower the ambient magnetic moment the higher the pressure of ferromagnetism extinction (Fig. 5.37 top panel). This was interpreted as due to the weak (Fe) or strong (Co and Ni) ferromagnetism. In FeCo, the relationship between the critical pressure for ferromagnetism stability (P^{NM}) and the ambient moment ($\mu(\text{FeCo})$) as a function of composition is far more complex (Fig. 5.37 bottom panel). In the bcc range ($x=0-0.5$) both P^{NM} and $\mu_B(\text{FeCo})$ increase while they start showing opposite behavior only after $x=0.75$, in the closed packed structures. This should be related to the band filling modifications. In fact, moving from Fe to Ni corresponds to a progressive filling of the minority d band, while the d majority bands changes slightly. However, as was discussed in the 5.2.2 section, in the Fe rich region of FeCo a comparable change in the occupancy of both majority and minority states occurs at the Fe site, determining the peculiar shape of the ambient saturation magnetization curve. The P-induced drop of the magnetic moment origins from the bands broadening

which follows from the compression of interatomic distances and is therefore intrinsically related to the band structure. It is worth noticing that the trend of the P^{NM} resembles that of the Fe magnetic moment (Fig. 5.4) up to $x=0.75$: increasing up to $x=0.5$ and then saturating.

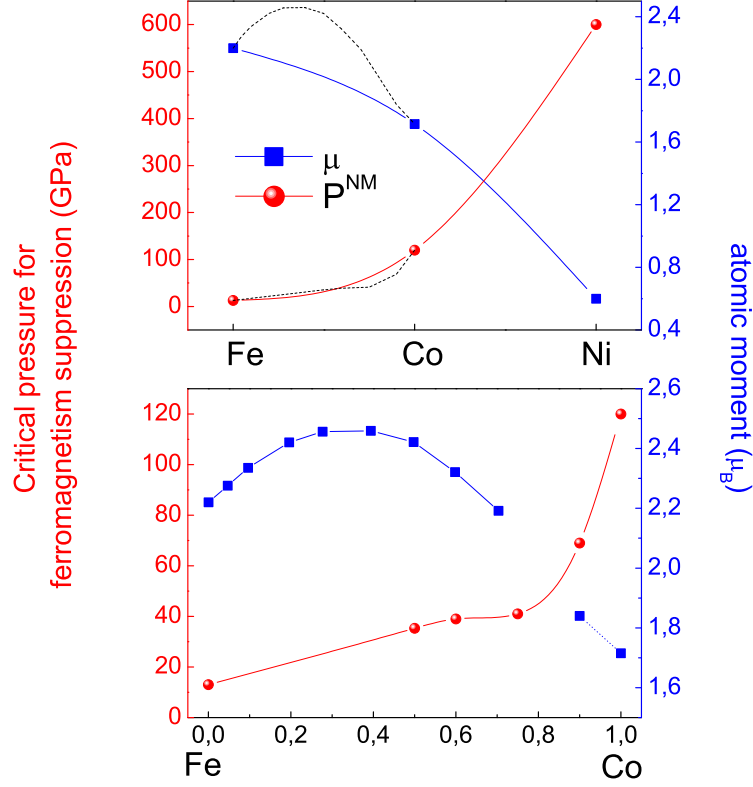


Figure 5.37: Top: Comparison between the ambient magnetic moment μ of Fe, Co and Ni (blue squares, reference scale right axis) and their critical pressure for ferromagnetism stability (P^{NM} , reference scale left axis). Bottom: Comparison between the ambient magnetic moment μ of FeCo (blue squares, reference scale right axis) and its critical pressure for ferromagnetism stability (P^{NM} , reference scale left axis) as a function of composition.

Putting together the informations from left and right panels of Fig. 5.36 a magnetic and structural phase diagram can be drawn for FeCo as a function of pressure and composition (Fig. 5.38). It is important to note that the proposed diagram lies on the following assumptions:

1. the bcc to hcp structural transition in the low Co % range ($0 < x \leq 40$) is accompanied by the loss of ferromagnetism just like in pure iron ($x=0.5$) and in the higher Co content bcc series ($50 \leq x \leq 75$);
2. the shift in the transition pressure given by sample annealing would be the same at all the concentrations in the bcc series. In the diagram in Fig 5.38 the bcc FM and hcp non-FM co-existence region, represented by a dashed area, has been chosen to

contain both as prepared and annealed samples under this assumption;

3. the XMCD signal suppression occurs at the same pressure for both Fe and Co K-edge in all samples.

As far as the complex $x=0.75$ sample is concerned, the bcc FM to hcp non-FM co-existence interval in the diagram has been chosen to contain the different transition pressures observed by XANES-XMCD at the two edges.

5.5 Conclusions

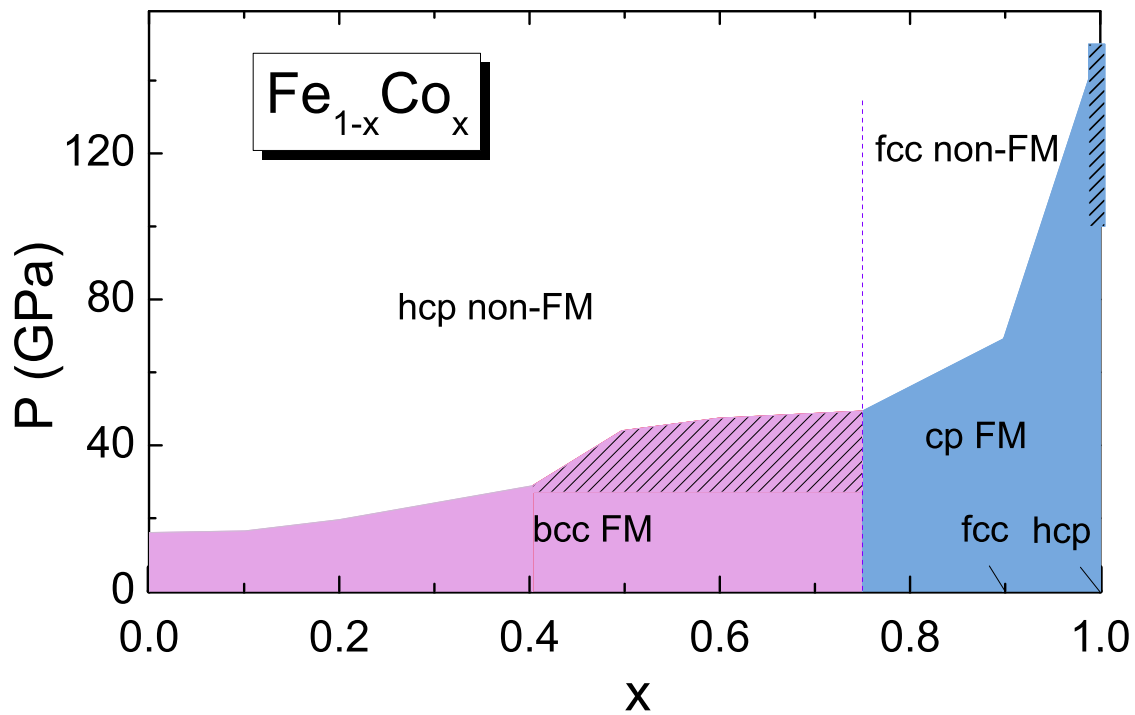


Figure 5.38: Structural and magnetic FeCo diagram as a function of pressure and composition. Dashed regions represent co-existence regions.

In summary, we have carried out a systematic study on the P-induced structural and magnetic transitions in $\text{Fe}_{1-x}\text{Co}_x$ in the high Co content range ($0.5 \leq x \leq 0.9$) by means of XRD and combined XANES-XMCD measurements and a detailed comparison with previous lower Co% data.

The most important outputs of this study are here summarized:

- In the bcc series, up to $x=0.75$, Co addition to Fe pushes the structural bcc-hcp transition to higher pressure in the 30-40 GPa range and the P-induced hcp phase is non-ferromagnetic like in the iron case. The enhanced stability of the FM bcc structure under pressure, with respect to pure Fe, follows from the filling of the

majority band. In the pressure region before the transition we detect a smooth linear decrease of the XMCD signal which can be associated to local bcc-hcp distortion anticipating the long-range order transition.

- The chemical order (disorder) can crucially influence the high pressure structural and magnetic response in the bcc FeCo alloy. Calculations show that chemically ordered structures are more resistant to compression than their disordered counterparts and undergo a sharp structural/magnetic transition around 34 GPa. In the disordered phases the transition is more sluggish, the hcp phase becoming favorite at 20 GPa but retaining a non-zero magnetic moment up to 70 GPa. The comparison with experimental findings suggest that the number of Co-Co homopolar bonds plays a key role in determining the high pressure magnetic and structural properties.
- In the fcc $x=0.9$ sample an isostructural transition is observed in correspondence to the onset of the K-edge XMCD signal decay suggesting that magnetic instabilities induced by compression play a driving role in the transition. The fcc symmetry is confirmed to be the most stable structure for the FM metals. Globally, the $x=0.9$ sample presents an intermediate behavior between that of the bcc series and that of pure Co. In fact the (iso)structural transition and the kink in the XMCD signal reduction occur around 30-40 GPa, in the same pressure region of the bcc FM - hcp non-FM transitions of the bcc series. On the other hand the XMCD decay after 40 GPa is smoother resembling that of pure Co. Indeed the suppression of ferromagnetism in $x=0.9$ occurs at a remarkably lower pressure (≈ 70 GPa) compared to pure cobalt (≈ 120 GPa) indicating that adding Fe impurities in Co strongly affects its HP magnetic response.
- Different sample preparation routes can determine different ambient structural parameters. However, the relative structural behavior as a function of pressure is in general the same, i.e. the annealing only causing a rigid pressure shift. Annealed samples show a larger lattice parameter (indicating a major degree of chemical order) and result to be more resistant to compression as the structural-magnetic transition is observed at higher pressures.
- The critical pressure for ferromagnetism stability in FeCo does not relate inversely to the ambient magnetic moment like in the pure metals, its behavior being largely determined by the complex interplay between majority and minority bands filling in the Fe rich region.

The collected data allowed to draw a high pressure magnetic and structural phase diagram for FeCo as a function of composition, so far missing in the literature.

Some preliminary results of this chapter have been published in *High Pressure Research* [278]. Completing papers are under preparation.

Conclusions

This Thesis deals with the study of the magnetic and structural properties of the 3d metals under extreme compression conditions by means of polarized X-ray absorption coupled to X-ray diffraction and DTF calculations. The squeezing of the interatomic distances, caused by the applied pressure, naturally involves important changes in the band structure and induces magnetic and structural instabilities. Its study can therefore bring an important contribution to the understanding of the complex interplay between structural, magnetic and electronic degrees of freedom that characterizes these metals. Fully exploiting the recent development of the diamond anvil cell coupled to the potential of a third generation synchrotron radiation source, this study allowed to fix some new important constraint in the high pressure magnetic and structural phase diagram of cobalt, nickel and iron-cobalt alloys. Moreover in Co relevant differences were highlighted with respect to the neighbor and widely investigated element Fe; in FeCo the role of chemical order in tuning the high pressure properties was addressed and the case of Ni offered the opportunity to get a deeper insight into the interpretation of the K-edge XMCD signal under compression, so far still controversial.

In these last pages, the main results obtained for these three systems will be resumed and finally some general conclusions will be drawn.

Cobalt

Combined K-edge XANES and XMCD measurements were carried out up to 120 ± 10 GPa on pure cobalt. Local fcc-like atomic configuration are observed in the XANES starting around 80 GPa in correspondence to the onset of elastic and structural anomalies reported in the literature at the same pressure. XANES simulations indicate that at 120 GPa the fcc phase is present at 40% or more and that the transformation into the fcc symmetry corresponds to a progressive symmetrization of the first shells around the absorber. The K-edge XMCD signal decreases linearly and continuously up to the total suppression around 120 GPa. Differently from the Fe case, where ferromagnetism is almost unaffected by compression until its abrupt suppression at the bcc-hcp phase transition,

in cobalt compression produces an immediate decay of the XMCD signal, long before the structural transition observed at 80 GPa. Spin magnetization DFT calculations reproduce the magnetic transition pressure within the pressure error bars, and suggest that the pressure induced phase is actually non magnetic (with zero elementary moment). However a quite different behavior between the evolution of the calculated spin magnetization and the K-edge XMCD signal integral is observed prior to the structural transition ($P < 80$ GPa).

Nickel

Simultaneous K-edge XANES-XMCD and XRD measurements were performed on pure nickel up to a relative compression of $V/V_0 = 0.66$ corresponding to around 200 GPa, a record pressure for absorption techniques. Our data show a stable fcc structure and a resistant ferromagnetism throughout the whole pressure range of study, contrary to the recent prediction of an abrupt transition to the paramagnetic state at 160 GPa. The high structural stability of nickel over a wide pressure range offers the opportunity to investigate the effect of the compression on magnetism, without the complexity given by the insurgence of a structural transition. This motivated us to go deeper into the still not established interpretation of the K-edge XMCD signal, exploiting the fruitful collaboration with the ESRF Theory group. Like in the cobalt case in the region prior to the structural transition, spin magnetization calculation do not reproduce the Ni K-edge XMCD signal decay under compression, whereas its behavior closely follows that of the calculated p -projected orbital moment. Our calculations point out that the spin polarization of the p states mainly originates from the p - d bands hybridization and that the p orbital moment is due to both $3d$ and $4p$ SO coupling.

FeCo

A systematic investigation was carried out on $\text{Fe}_x\text{Co}_{1-x}$ alloys in an unexplored pressure ($P < 70$ GPa) and concentration range ($0.5 \leq x \leq 0.9$) by means of polarized absorption and X-ray diffraction. In the bcc samples ($x = 0.5, 0.6$) the bcc ferromagnetic to hcp non ferromagnetic transition is observed just like in the pure iron case but at higher pressures (in the 30-40 GPa range) as a consequence of the strong ferromagnetism induced by the filling of the majority band due to the Co addition. Local bcc-hcp distortion and a corresponding smooth initial decay of the XMCD signal are detected around 20 GPa, before the global magnetic and structural transition. This effects seem to be stronger around the Co site and are likely related to the presence of some chemical disorder. Indeed DTF calculations show that the chemical order plays a crucial role in tuning the high pressure structural and magnetic behavior: in the disordered structures the hcp phase becomes favorite at lower pressures (20 GPa) but remains magnetic up to higher pressures (70 GPa).

At $x=0.75$ the sample is found in a mixed bcc-hcp phase at ambient conditions, however a pressure induced transition to pure hcp can still be recognized around 30-40 GPa.

In the $x=0.9$ fcc sample the onset of magnetic instabilities induces an isostructural transition around 30 GPa; however the total suppression of ferromagnetism occurs, in the lower volume fcc phase, at quite higher pressures around 70 GPa.

Finally we found that the preparation route can influence the high pressure magnetic and structural properties: in particular the sample annealing, enhancing the chemical order, increases the ferromagnetism resistance to pressure.

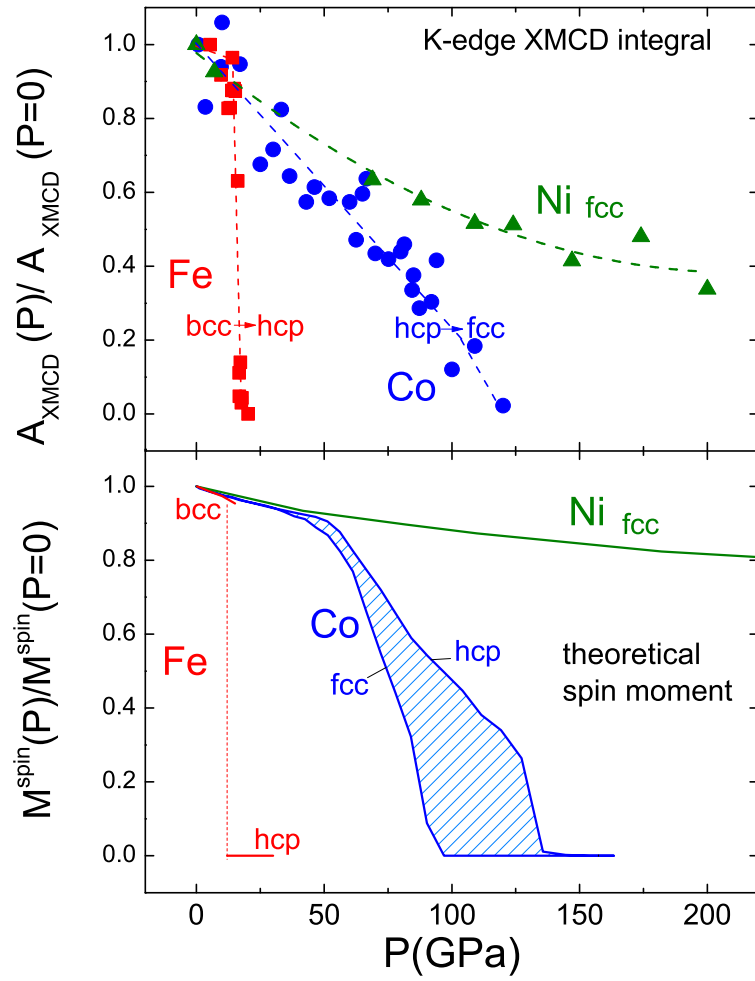


Figure 6.1: Top: normalized K-edge XMCD integrals, labeled A_{XMCD} , for Fe (red squares), Co (blue circles) and Ni (green triangles) as a function of pressure. Fe data are from [93], Co and Ni data are from this Thesis. Pressure and integrals errors are not indicated. Bottom: ab initio GGA spin magnetization calculation for Fe [43], Co and Ni (from this Thesis).

General conclusions

The collected results allow to formulate some general conclusions:

- Under pressure a bcc ferromagnetic 3d metal transforms into a non magnetic hcp phase and an hcp ferromagnetic 3d metal becomes a fcc non magnetic one, in agreement with the equilibrium structures expected for the non magnetic counterparts from the filling of the *3d* electronic band. No further structural transformation is expected to occur in fcc 3d metals; in fact only an isostructural transition could be induced in the fcc $\text{Fe}_{0.1}\text{Co}_{0.9}$ sample.
- The close packed arrangements (hcp and fcc) furnish a major magnetic resistance to compression: in bcc Fe and bcc FeCo the suppression of ferromagnetism occurs below 40 GPa, while in fcc $\text{Fe}_{0.1}\text{Co}_{0.9}$, hcp Co and fcc Ni magnetic order is kept up to 70 GPa, 120 GPa and well over respectively. Interestingly, the fcc structure is not necessarily magnetically more stable than the hcp, as it is seen by comparing $\text{Fe}_{0.1}\text{Co}_{0.9}$ to pure hcp Co.
- In the bcc structures (pure Fe and FeCo up to $x=0.75$) the magnetic and structural transition are simultaneous and occur quite abruptly (within 10 GPa). The evolution of the XMCD signal shows a "step like" shape, characterized by an initial smooth decrease followed by a sharper drop. In the close packed structures ($\text{Fe}_{0.1}\text{Co}_{0.9}$ and pure Co) the suppression of ferromagnetism covers a quite wide pressure range and the relation to the structural instability is less straightforward: in $\text{Fe}_{0.1}\text{Co}_{0.9}$ the onset of the XMCD decay corresponds to an isostructural transition (30 GPa) however the total suppression occurs at much higher pressures (70 GPa); in cobalt, the decrease of XMCD signal starts immediately, long before the onset of the structural instabilities (80 GPa), and the total extinction occurs in a likely mixed hcp-fcc phase (120 GPa).

K-edge XMCD is nowadays the only magnetic probe able to reach the 10^2 GPa range, however a complete understanding of the scientific information carried by this technique is still not achieved. Therefore, a second aim of this Thesis has been to go deeper into the interpretation of the K-edge XMCD signal, still debated in the literature. On one side the atomic dipolar sum rule indicates a proportionality of the signal integral to the orbital *p*-projected moment; on the other hand multiple scattering approaches point out a dominant role played by the spin polarization of the *3d* band. Following this latter approach, the

K-edge XMCD signal under pressure is generally compared to the calculated spin magnetization, as in Fig. 6.1. These spin calculations describe successfully the Fe case, the bcc spin magnetization decreasing slowly until the hcp non magnetic phase becomes favorite at 12 GPa. In cobalt, the pressure for magnetism extinction indicated by the calculations roughly corresponds to that indicated by the experimental data, nevertheless the trend is not reproduced in the pressure region before the structural transition ($P < 80$ GPa) and the same stands for nickel in the whole range studied.

Our new calculations show that the Ni K-edge XMCD decay under compression is better represented by that of the calculated p -projected orbital moment. Interestingly the calculated spin magnetization decay is "step like" - i.e. characterized by an initial smooth decrease followed by a sharper drop - whereas the p orbital moment decreases continuously up to a sharper inflection which brings to total extinction occurring simultaneously with the spin suppression. This is not surprising since in the 3d metals the orbital moment, largely quenched by the crystal field, only arises from the spin orbit interaction. Therefore the existence of a non zero K-edge XMCD signal is related to the presence of non zero net spin moment and the suppression of the signal indicates the loss of ferromagnetism, explaining why the spin magnetization calculations can successfully describe the ferromagnetism suppression pressure. The results obtained for nickel suggest that p orbital calculations could also reproduce the K-edge XMCD behavior in cobalt for $P < 80$ GPa. In iron the range before the transition is too small (10 GPa) to appreciate any difference between the available K-edge XMCD and spin magnetization behavior, and more accurate measurements (more pressure points and lower error bars) are needed. However it is important to note that iron indeed differs from Co and Ni because it is a weak ferromagnet, having both majority and minority bands unfilled. It was already pointed out, in the FeCo chapter, that this weak ferromagnetism plays a crucial role for example in determining the anomalous magnetization behavior in the FeCo series. Also, it crystallizes in a bcc symmetry, quite different from the close packed arrangements of Co (hcp) and Ni (fcc).

Another aspect that needs to be considered is that XMCD is only sensible to the existence of a net orbital moment (ferromagnetism or ferrimagnetism) and does not allow to distinguish between zero net moment magnetic states (paramagnetism, diamagnetism or antiferromagnetism). Therefore Curie temperature effects, disrupting the magnetic order cannot in principle be excluded. However, the coinciding suppression of K-edge XMCD signal and calculated spin moment in Fe and Co suggest that the pressure induced magnetic state in these systems is actually non magnetic, i.e. with zero magnetic atomic moment.

On the base of the discussion above, these studies stimulate two natural developments: on the experimental side the coupling of high pressure to low temperature conditions appears necessary, which would allow to separate thermal order effects from elementary moment changes. A high pressure-low temperature setup is currently under development on beamline ID24. On the theoretical side, volume dependent orbital moment calculations, so far missing in the literature, will be completed by the ESRF Theory group and compared with the present K-edge XMCD results in order to clarify if the results obtained for nickel can be generalized to the other 3d metals.

Bibliography

- [1] N.F. Mott, Proc. Phys. Soc. (London) **47** (1935) 571
- [2] J.C. Slater, Phys. Rev. **49** (1936) 537
- [3] J.C. Slater, Phys. Rev. **49** (1936) 931
- [4] E.C. Stoner, Proc. Roy. Soc. (London) A **154** (1936) 656
- [5] E.C. Stoner, Proc. Roy. Soc. (London) A **165** (1938) 372
- [6] W. Heisenberg, Zeitsch. f. Physik. **38** (1926) 441
- [7] F. Bloch, *Phys. Rev.* **70**, (1946) 460
- [8] T. Moriya and Y. Takahashi, *J. Phys. Soc. Jpn.* **45**, 397 (1978).
- [9] J. Hubbard, *Phys. Rev. B* **20**, 4584 (1979).
- [10] H. Hasegawa, *Solid State Commun.* **31**, 597 (1979).
- [11] V. Korenman, J. L. Murray, and R. E. Prange, *Phys. Rev. B* **16**, 4032 (1977).
- [12] B.L. Gyorffy, A.J. Pindor, J. Staunton, G. M. Stocks and H. Winter, *J. Phys. F* **15**, 1337 (1985).
- [13] M.D. Edwards, *J. Phys. F* **12**, 1789 (1982).
- [14] T. Moriya, *Spin Fluctuations in Itinerant Electron Magnetism* (Springer, Berlin, 1985).
- [15] H. Capellmann, *Metallic Magnetism* (Springer, Berlin, 1987).
- [16] J. Stöhr and H.C. Siegmann, *Magnetism from fundamentals to nanoscale dynamics*, (Springer, New York, 2006)

- [17] J.B. Staunton, *Rep. Prog. Phys.* **57** (1994) 1289-1344
- [18] J.Mathon, A. Umerski, *Physics of low dimensional systems*, ed. by J. Morán-López (Kluwer/Plenum, New York, 2001), p. 363
- [19] R. Wu, D. Wang, A.J. Freeman, *Phys. Rev. Lett.* **71** (1993) 3581
- [20] R. Wu, A.J. Freeman, *Phys. Rev. Lett.* **73** (1994) 1994
- [21] O. Eriksson, B. Johansson, R.C. Alberts and A.M. Boring, *Phys. Rev. B* **42**, 2707 (1990).
- [22] A.R. Williams, R. Zeller, V.L. Moruzzi, C.D. Gelatt Jr., and J.Kübler, *J. Appl. Phys.* **52** 2067 (1981)
- [23] K. Schwarz, P. Mohn, P. Blaha, J. Kübler, *J. Phys. F: Met. Phys.* **14** (1984) pp. 2659-2671.
- [24] J. M. Maclaren, T. C. Schulthess, W. H. Butler, R. B. Sutton, and M. E. McHenry, *J. Appl. Phys.* **85**(1999) 4833.
- [25] P. Mohn, *Magnetism in the Solid State* (Springer, New York, 2006).
- [26] Stearns, *Landolt-Börstein Numerical Data and Functional Relationships in Science and Technology* (Springer-Verlag Berlin, 1986) B.C.H.Krutzen and F.Springelkamp, *J. Phys. Condens. Mater*, **1**, 8369 (1989)M.B.
- [27] D.G. Pettifor, *Materials Science and Technology* **4** (1988) 2480
- [28] H.L. Skriver, *Phys. Rev. B* **31**, 1909 (1985)
- [29] J.C Duthie and D.G. Pettifor, *Phys. Rev. Lett.* **38** (1977) 564
- [30] P. Söderlind, R. Ahuja, O. Eriksson, J.M. Wills, B. Johansson, *Phys. Rev. B* **50**, 5918 (1994)
- [31] Y. B. Zeldovich and Y. P. Raizer, *Physics of shock waves and high temperature hydrodynamic phenomena* (Academic Press, New York, 1967), Vol. 1 and 2.
- [32] R.A. Graham, *Solids under high-pressure shock compression: mechanics, physics, and chemistry*(Springer-Verlag, New York, 1993).
- [33] J.-W. G. Bos, B. B. Van Aken, and T.T.M. Palstra, *Chem. Mater.* **13**, 4804 (2001).
- [34] E.V. Zarochentsev and E. P. Troitskaya, *Phys. of the Solid State* **44**, 1370 (2002).
- [35] A. K. McMahan and R. C. Alberts, *Phys. Rev. Lett.* **49**, 1198 (1982).
- [36] M. Citroni, M. Ceppatelli, R. Bini, and V. Schettino, *High Press. Res.* **22**, 507 (2002).

- [37] J.M. Leger, C. Loriers-Susse, and B. Vodar, *Phys. Rev. B* **6** (1972) 4250
- [38] M. Shiga, *Solid St. Commun.* **7**, (1969) 559-562
- [39] V. Heine, *Phys. Rev.* **153** 673-82 1969
- [40] G. Krasko, *Solid State Commun.*, **20** (1989) 1099-1103
- [41] V.L. Moruzzi and P.M. Marcus, *Phys. Rev. B* **38** (1988) 1613-1620
- [42] V. Iota, J.P. Klepeis, C. Yoo, J. Lang, D. Haskel, G. Srajer, APL **90**,042505 (2007).
- [43] Y.S.Mohammed, Y.Yan, H.Wang, K.Li, X.Du, *Jour. Mag. Mag. Mat.*, **322** (2010)653-657
- [44] J. Xie, S.P. Chen, H.V. Brand and R.L. Rabie, *J. Phys.: Condens. Matter* **12**, 8953-8962 (2000).
- [45] T. Jarlborg, *Physica C* **385**,513-524 (2003)
- [46] M. Ekman, B. Sadigh, K. Einarsdotter, P. Blaha, *Phys. Rev. B* **58**(1998)5296.
- [47] J. Zhu, X.W. Wang, S.G. Louie, *Phys.Rev.B* **45**(1992) 8887.
- [48] T.C. Leung, C.T. Chan, B.N. Harmon, *Phys. Rev. B* **44** (1991) 2923.
- [49] E.G. Moroni, G. Kresse, J. Hafner, and J. Furthmüller, *Phys. Rev. B* **56**, 15629 (1997)
- [50] P.Modak *et al.*, *Phys. Rev. B* **74**, 012103 (2006)
- [51] J.E. Saal *et al.*, S. Shang, Y. Wang and Z. Liu, *J. Phys.: Condens. Matter* **22**, 096006(2010).
- [52] G.Steinle-Neumann *et al.*, *Phys. Rev. B* **77**,104109 (2008)
- [53] M. Brouha and A.G. Rijnbeek, *High Temp. High Pres.*, **6** (1974) 519-524
- [54] P. Lazor (1994) PhD Thesis Uppsala University
- [55] Y. Takehashi, *Phys. Rev. B* **38** (1988) 6928-6940
- [56] S.Morán, C. Ederer, and M. Fähnle, *Phys. Rev. B* **67**, (2003) 012407
- [57] M. Shimizu, *Jour. Phys. Soc. Jpn.*, **44**(1978) 3
- [58] S. Shang, Y. Wang, and Z. Liu, *Phys. Rev. B* **82** (2010) 014425
- [59] V.G. Tissen, *Sov. Phys. Solid. State* **25**(11), 1983
- [60] S. Shang, J. E. Saal, Z.G. Mei, Y. Wang, and Z.K. Liu, *J. Appl. Phys.* **108**, 123514 (2010).

- [61] C.S. Yoo, H. Cynn, P. Sonderlind, V. Iota, *Phys. Rev. Lett.*, **84**, 4132-4135 (2000).
- [62] A. Dewaele, M. Torrent P. Loubeyre, M. Mezouar , *Phys. Rev. B* **78**, 104102 (2008).
- [63] N. Ishimatsu, H. Maruyama, N. Kawamura, M. Suzuki, Y. Ohishi, O. Shimomura, *Jour. Phys. Soc. Jap.* **76**(2007) 064703
- [64] *Pressure-induced collapse of ferromagnetism in cobalt up to 120 GPa as seen via x-ray magnetic circular dichroism*, R. Torchio, A. Monza, F. Baudalet, S. Pascarelli, O. Mathon, E. Pugh, D. Antonangeli, J. Paul Itié, *Phys. Rev. B Rapid communications*, *Phys. Rev. B* **84**, 060403(R) (2011)
- [65] N.Ishimatsu, N.Kawamura, H.Maruyama, M.Mizumaki, T.Matsuoka, H.Yumoto, H.Ohashi and M.Suzuki, *Phys. Rev. B* **83**, 180409(R) (2011)
- [66] H. Hasegawa and D.G. Pettifor, *Phys. Rev. Lett.* **50** 130 (1983)
- [67] L. Stixrude, R. E. Cohen, and D. J. Singh, *Phys. Rev. B* **50**, 6442 (1994).
- [68] R. Jeanloz, *Annu. Rev. Earth Planet Sci.* **18**, 357 (1990).
- [69] M.V. You, V. Heine, A.J. Holden, and P.J. Lin-Chung, *Phys. Rev. Lett.***44** (1980) 1282
- [70] H. Hasegawa, M.W. Finnis, and D.G. Pettifor, *J. Phys. F: Met. Phys.* **15** (1985) 19-34
- [71] D. Bancroft, E.L. Peterson, S. Minshall, *J. Appl. Phys.* **27** (1956) 291
- [72] M. Nicol and G. Jura (1963) *Science* **141** 1035
- [73] K. Shimizu, T.Kimura, S. Furomoto, K. Takeda, K. Kontani, Y. Onuki and K. Amaya, *Nature*, **412**, 6844 (2001)
- [74] S.K. Bose , O.V. Dolgov, J. Kortus, O. Jepsen and O.K. Andersen, *Phys. Rev. B* **67**(2003) 214518
- [75] C.S. Yoo, P. Söderlind, J.A. Moriarty and A.J. Campbell, *Phys. Lett. A* **214** (1996) 65-70
- [76] S.K. Saxena , L.S. Dubrovinsky , P. Häggkvist , Y. Cerenius, G. Shen and H.K. Mao, *Science* **269** (1995) 1703
- [77] M. Ross, D.A. Young and R. Grover, *J. Geophys. Res.* **95** (1990) 21713.
- [78] R. Boehler, *Nature* **363**(1993) 534.
- [79] S.K. Saxena, G. Shen and P. Lazor, *Science* **260** (1993) 1312.

- [80] J.A. Moriarty, in: *High pressure science and technology- 1993*, Part I, eds. S.C. Schmidt et al. (AIP Press, New York, 1994) p. 233
- [81] T. Asada and K. Terakura, *Phys. Rev. B* **46** (1992) 13599
- [82] H. C. Herper, E. Hoffmann, and P. Entel, *Phys. Rev. B* **60**, 3839 (1999).
- [83] P. Söderlind and J. A. Moriarty, *Phys. Rev. B* **53**, 14 063 (1996).
- [84] W. Pepperhoff and M. Acet, *Constitution and Magnetism of Iron and its Alloys* (Springer-Verlag, Berlin, Heidelberg, 2001).
- [85] K. J. Caspersen, A. Lew, M. Ortiz, and E. A. Carter, *Phys. Rev. Lett.* **93**, 115501 (2004).
- [86] V. Thakor, J.B. Stauton, J. Poulter, S. Ostanin, B. Ginatempo, and E. Bruno, *Phys. Rev. B* **67**, 180405(R) (2003).
- [87] E. Huang, W. A. Bassett, and P. L. Tao, *J. Geophys. Res. Solid Earth Planets* **92**, 8129 (1987).
- [88] F.M. Wang and R. Ingalls, *Phys. Rev. B* **57**, 5647 (1998)
- [89] G. Cort, R. D. Taylor, and J. O. Willis, *J. Appl. Phys.* **53**, 2064 (1982).
- [90] R.D. Taylor, G. Cort, and J. O. Willis, *J. Appl. Phys.* **53**, 8199 (1982).
- [91] R.D. Taylor, M. P. Pasternak, and R. Jeanloz, *J. Appl. Phys.* **69**, 6126 (1991).
- [92] J. P. Rueff, M. Krisch, Y.W. Cai, A. Kaprolat, M. Hanfland, M. Lorenzen, C. Maschiovecchio, R. Verbeni, and F. Sette, *Phys. Rev. B* **60**, 14 510 (1999).
- [93] O. Mathon, F. Baudelet, J.P. Ité, A. Polian, M. d'Astuto, J. C. Chervin, and S. Pascarelli, *Phys. Rev. Lett.* **93**, 255503 (2004).
- [94] O.Mathon, F. Baudelet, J.P. Ité, S. Pasternak, A. Polian and S. Pascarelli, *J. Synchrotron Radiat.* **11**, 423 (2004).
- [95] F. Baudelet, S. Pascarelli, O. Mathon, J.P. Itié, A. Polian, M.d' Astuto, J.C. Chervin, *J. Phys.: Condens. Matter* **17** (2005) pp. 957-966
- [96] S. Klotz and M. Braden, *Phys. Rev. Lett.* **85**, 3209 (2000).
- [97] R. M. Bozorth, *Ferromagnetism*, first published 1951, reprinted 1993 by IEEE Press, New York
- [98] T. Mitsui, N. Hirao, Y. Ohishi, R. Masuda, Y. Nakamura, H. Enoki, K. Sakaki and M. Seto, *J. Synchrotron Radiat.* **16**, 723-729 (2009).

- [99] G. Steinle-Neumann *et al.*, Phys. Rev. B **60**, 791 (1999)
- [100] H.K. Mao, W.A. Bassett, T. Takahashi, *J.Appl.Phys.* **38** (1967) 272.
- [101] A.P. Jephcoat, H.K. Mao, P.M. Bell, *J.Geophys.Res.* **91**(1986) 4677.
- [102] W.A. Bassett, E. Huang, *Science* **238**(1987)780.
- [103] M.I. Eremets, High Pressure Experimental Methods (Oxford University Press,Oxford, 1996).
- [104] J. A. Xu, H. K. Mao, and P. M Bell, *Science* **232**, 1404 (1996).
- [105] C. E. Wier, E. R. Lippincott, A. Valkenburg, and E. N. Bunting, Journal of Research, National Bureau of Standards 63A, 55 (1959).
- [106] A. Jayaraman, *Rev. of Mod. Phys.* **55**, 65 (1983).
- [107] J. C. Chervin, B. Canny, J. M. Besson, and Ph. Pruzan, *Rev. Sci. Instrum.*, **66** 2595-2598.(1995)
- [108] R. Le Toullec, J. P. Pinceaux, and P. Loubeyre, *High Pressure Res.* **1**, 77 (1988).
- [109] W.L. Mao and H.K. Mao, *J. Phys.: Condens. Matter*, **18** (2006) S1069-S1073.
- [110] A. Dadashev, M. P. Pasternak, G. Kh. Rozenberg, and R. D. Taylor, *Rev. Sci. Instrum.*, **72** (2001) 6
- [111] A. Van Valkenburg, Conference Internationale Sur-les-Hautes Pressions, LeCreusot, Saone-et-Loire, France (1965).
- [112] H. K. Mao and P. M Bell, *Science* **200**, 1145 (1978).
- [113] D. J. Dunstan, Rev. Sci. Instrum. **60**, 3789 (1989)
- [114] G. J. Piermarini, S. Block, and J. S. Barnett, J. Appl. Phys. **44**, 5377 (1973).
- [115] A. Dewaele, P. Loubeyre, High. Prss. Res. **27**, 419 (2001)
- [116] K. Syassen, *High Press. Res.* **28**, 75 (2008).
- [117] J. Freund and R. Ingalls, *Phys. Rev B* **39** (1989) 12537-12547
- [118] R.A. Forman, G. J. Piermarini, J. D. Barnett, and S. Block, *Science* **176**, 284 (1972).
- [119] J.D. Barnett, S. Block, and G. J. Piermarini, Rev. Sci. Instrum. **44**, 1 (1972).
- [120] G.J. Piermarini and S. Block, *Rev. Sci. Instrum.* **46**, 973 (1975).
- [121] H.K. Mao, J. Xu, and P.M. Bell, *J. Geophys. Res.* **91**, 4673 (1986).

- [122] H.K. Mao, in *Simple molecular systems at very high density*, edited by A. Polian and N. Boccara (Plenum Press, New York, 1989), Chap. *Static compression of simple molecular systems in the megabar range*, pp. 221-236.
- [123] W. L. Vos and J. A. Schouten, *J. Appl. Phys.* **69**, 6744 (1991).
- [124] S. Rekhi, L. Dubrovinsky, and S. Saxena, *High Temp. - High Press.* **31**, 299 (1999).
- [125] F. Goncharov, J.M. Zaug, J.C. Crowhurst, and E. Gregoryanz, *J. Appl. Phys.* **97**, 094917 (2005).
- [126] G. Schütz, W. Wagner, W. Wilhelm, P. Kienle, R. Zeller, R. Frahm, G. Materlik, *Phys. Rev. Lett.* **58**, 737 (1987)
- [127] J. Stohr and Y. Wu, in A.S. Schlachter and F.J. Wuilleumier (Eds.), *New Directions in Research with Third- Generation Soft X-Ray Synchrotron Radiation Sources*, Kluwer Academic Publishers, Netherlands, 1994, p. 221.
- [128] U. Fano, *Phys. Rev.* **178** (1969) 131-136
- [129] J. Stöhr, H. König, *Phys. Rev. Lett.* **75**, 3748 (1995)
- [130] P. Carra, B.T. Thole, M. Altarelli and X. Wang, *Phys. Rev. Lett.*, **70** (1993) 694.
- [131] B.T. Thole, P. Carra, F. Sette and G. van der Laan, *Phys. Rev. Lett.* **68**, 1943 (1992)
- [132] C.T. Chen et al., *Phys. Rev. Lett.* **75**, 152 (1995)
- [133] G.Y. Guo, *J. Phys.: Condens. Matter*, **8**, L747-L752 (1996); *Phys. Rev. B*, **55**, 11619-11628 (1998).
- [134] J. Igarashi and K. Hirai, *Phys. Rev. B* **50**, 17 820 (1994)
- [135] H. Ebert, P. Strange, and B. Gyorffy, *Z. Phys. B* **73**, 77 (1988).
- [136] H.J. Gotsis and P. Strange, *J. Phys.: Condens. Matter* **6**, 1409 (1994).
- [137] M.S.S. Brooks and B. Johansson, in *Spin-Orbit Influenced Spectroscopies*, edited by H. Ebert and G. Schultz Springer, Heidelberg, 1996, p. 211.
- [138] V.N. Antonov, B.N. Harmon, A.N. Yaresko, *Phys. Rev. B* **67**, 024417 (2003)
- [139] A.L. Ankudinov and J. J. Rehr, *Phys. Rev. B* **52**, 10 214 (1995).
- [140] C. Brouder, M. Alouani, and K. H. Bennemann, *Phys. Rev. B* **54**, 7334 (1996).
- [141] J.P. Rueff *et al.*, *Phys. Rev. B* **58**, 12271-12281 (1998)
- [142] J. Igarashi and K. Hirai, *Phys. Rev. B* **53**, 10 (1996)

- [143] A.L. Cornelius, J.S. Schilling, O. Vogt, K. Mattenberger, and U. Benedict, *J. Magn. Magn. Mater.* **161** (1996) 169-176.
- [144] I.N. Goncharenko and I. Mirebeau, *Europhys. Lett.* **37** (1997) 633-638.
- [145] D. N. Pipkorn, C. K. Edge, P. Debrunner, G. De Pasquali, H. G. Drickamer, and H. Frauenfelder, *Phys. Rev.* **135**, A1603 (1964)
- [146] M. Hagelstein, A. Fontaine, and J. Goulon, *Jpn. J. Appl. Phys.* **32**, 240 (1993).
- [147] M. Hagelstein, A. San Miguel, A. Fontaine, and J. Goulon, *J. Phys. IV, Colloque C2 7*, C2 303 (1997).
- [148] T. Matsushita and R. P. Phizakerley, *Jpn. J. Appl. Phys.* **20**, 2223 (1981).
- [149] R. P. Phizackerley, Z. U. Rek, G. B. Stephenson, S. D. Conradson, K. O. Hodgson, T. Matsushita, and H. Oyanagi, *J. Appl. Cryst.* **16**, 220 (1983).
- [150] A. Fontaine and J. Goulon, ESRF Internal Report on Source Specifications for BL8AF-JG/XAS/ESRF/02-91 (1991).
- [151] A. Koch, M. Hagelstein, A. San Miguel, A. Fontaine, and T. Ressler, *Proc. SPIE* **2416** (1996) 85-93.
- [152] J. Pellicer Porres, A. San Miguel, and A. Fontaine, *J. Synchrotron Rad.* **5**, 1250 (1998).
- [153] A. San Miguel, M. Hagelstein, J. Borrel, G. Marot, and M. Renier, *J. Synchrotron Rad.* **5**, 1396 (1998).
- [154] C. Giles, C. Malgrange, J. Goulon, F. de Bergevin, C. Vettier, E. Dartyge, A. Fontaine, and S. Pizzini, *Nucl. Instrum. Methods* **A349** (1994) 622-625.
- [155] S. Pizzini, M. Bonfim, F. Baudelet, H. Tolentino, A. San Miguel, K. Mackay, C. Malgrange, M. Hagelstein, and A. Fontaine *J. Synchrotron Rad.* **5** (1998) 1298-1303.
- [156] S. Pascarelli, P. Mathon, and G. Aquilanti, *J. Alloy Comp.* **363** (2004) 33-40.
- [157] O. Hignette, G. Rostaing, P. Cloetens, W. Ludwig, and A. Freund, *Proc. SPIE* **4499**(2001) 105-109.
- [158] D. Haskel, Y. C. Tseng, and J. C. Lang, *Rev. Sci. Instrum.* **78** (2007) 083904
- [159] V.F. Puentes, K. M. Krishnan, and A. P. Alivisatos, *Science* **291**, 2115 (2001).
- [160] V.A. de la Peña O'shea, P. Ramirez de la Piscina, N. Homs, G. Aromí, and J. L. G. Fierro, *Chem. Mater.* **21**, 5637 (2009).

- [161] V. A. de la Peña OShea, J. M. Campos-Martin, and J. L. G. Fierro, *Catal. Commun.* **5**, 635 (2004).
- [162] E.Pugh, *Phil. Trans. R. Soc. Lond. A*, **361**, 2715-2729 (2003).
- [163] D.A. Young, *Phase Diagrams of the Elements* (Livermore. CA: University of California Press) 1991
- [231] T. Nishizawa and K. Ishida 1983 *Bull. Alloy Phase Diagrams* **4** 387
- [165] H.Fujihisa and K. Takemura, *Phys. Rev. B* **54**, 5 (1996).
- [166] D.Antonangeli, L.R. Benedetti, D.L. Farber, G. SteinleNeumann, A. Auzende, J. Badro, M.Hanfland, and M. Krisch, *Appl. Phys. Lett.* **92**, 111911 (2008)
- [167] A. R. Troiano and J. L. Tokich, *Trans. AZME*, **175**, 728 (1948).
- [168] J. W. Christian, *Proc. R. Soc.* **206 A**, 51 (1951).
- [169] J. B. Hess and C. S. Barrett, *Trans. Am. Inst. Min. Met. Eng.* **194**, 645 (1952).
- [170] H. Bibring and F. Sebillleal, *Rev. Met.* **52**, 569 (1955).
- [171] A. Seeger, *Z. Metallkunde* **47**, 653 (1956).
- [172] J.E. Bidaux, R. Schaller and W. Benoit, *acta metall.* Vol. 37, No. 3, pp. 803-81 I, 1989
- [173] F Frey, W Prandl, J Schneider. C Zeyen and K Ziebeck, *J. Phys. F: Metal Phys.* Vol. 9. No 4. 1979.
- [174] B. Strauss, F. Frey, W. Petry, J. Trampenau, K. Nicolaus, S. M. Shapiro and J. Bossy, *Phys. Rev. B* **54**, 6035-6038 (1996).
- [175] C.S.Yoo, P. Söderlind and H. Cynn, *J. phys. : Condens. Matter* **10**, L311 (1998)
- [176] C.S. Yoo , J. Akella , A. Campbell , H.K. Mao and R. J. Hemley, *Science* **270** (1995) 1473
- [202] A.Y.Liu,D.G.Singh,*Phys.Rev.B*47(1993)8515
- [275] C.Kittel, *Introduction to Solid State Physics*,6thed.(Wiley, NewYork,1986).
- [179] H. Olijnyk and A. P. Jephcoat, *Solid State Commun.* **115**, 335 (2000).
- [180] J.C. Upadhyaya, D. K. Sharma, D. Prakash, and S. C. Upadhyaya, *Can. J. Phys.* **72**, 61 (1994)
- [181] A. Goncharov, J. Crowhurst, and J.M. Zaug , *Phys. Rev. Lett.* **92**, 115502 (2004)

- [182] D. Antonangeli, M. Krisch, G. Fiquet, J. Badro, D. L. Farber, A. Bossak, and S. Merkel, *Phys. Rev. B* **72**, 134303 (2005)
- [183] H. R. Schober and H. Dederichs, Elastic, Piezoelectric, Pyroelectric, Piezooptic, Electrooptic Constants and Nonlinear Dielectric Susceptibilities of Crystals, edited by Landolt-Börnstedt, New Series III, Springer, Berlin, (1979), Vol.
- [184] A.I. Akhiezer, V.G. Bariakhtar, and S.V. Peletminskii, *Sov. Phys. JETP* **36**, 157 (1959)
- [185] G. A. Smolenskii et al., *Physics of Magnetic Dielectrics*, edited by G.A. Smolenskii (Nauka, Leningrad, 1974).
- [186] S. Pascarelli, O. Mathon, M. Muñoz, T. Mairs and J. Susini, *J. Synchrotron Rad.* (2006). **13**, 351-358
- [187] H.K. Mao, J. Xu, and P. Bell, *J. Geophys. Res.* **91**, 4673 (1986).
- [188] S. Pizzini, A. Fontaine, E. Dartyge, C. Giorgetti, F. Baudelet, J.P. Kappler, P. Boher and F. Giron, *Phys. Rev. B* **50** (1994) 3779-3788
- [189] M. Hikam, PhD Thesis, Nancy, France, 1993.
- [190] M. Newville, *J. Synchrotron Rad.* **8**, pp 322-324 (2001).
- [191] B. Ravel and M. Newville, *J. Synchrotron Rad.* **12**, pp 537-541 (2005).
- [192] E. Pugh, PhD Thesis, University of Cambridge (1999)
- [193] C.R. Natoli, *EXAFS and Near Edge Structure III*, K. O. Hodgson, B. Hedman, and J. E. Penner-Hahn (Springer, Berlin, Heidelberg, 1994) p. 167.
- [194] A.L. Ankudinov, B. Ravel, J.J. Rehr, S. D. Conradson, *Phys. Rev. B* **58**, 7565 (1998)
- [195] A program written by S. Froyen and adapted by G.J. McMullan was used to generate the atomic charge densities that were used to calculate the initial potentials.
- [196] H.L. Skriver, *The LMTO Method-Muffin Tin Orbitals and Electronic Structure* (Springer-Verlag, New York 1984)
- [197] G.J. McMullan, PhD Thesis, University of Cambridge (1989)
- [198] F. Birch, *J. Geophys. Res.*, **57**, 227 (1952)
- [199] H.P. Meyer and W. Sucksmith, *Proc. R. Soc. London, Ser A* **207**, 427 (1951)
- [200] P. Tolédano *et al.*, *Phys. Rev. B* **64**, 144104 (2001)

- [201] A. Rogalev, F. Wilhelm, N. Jaouen, J. Goulon, and J.P. Kappler, *Lect. Notes Phys.* **697**, 71-93 (2006)
- [202] L. Liu, *Geochem J*, **16** (1982) 179-198.
- [203] P. Lazor, G. Shen, and S.K. Saxena, *Phys Chem Minerals* **20**(1993) 86-90
- [204] A. Dewaele, P. Loubeyre, F. Occelli, M. Mezouar, P. I. Dorogokupets, and M. Torrent, *Phys. Rev. Lett.* **97**, 215504 (2006).
- [205] M. Mezouar, W. A. Crichton, S. Bauchau, F. Thurel, H. Witsch, F. Torrecillas, G. Blattmann, P. Marion, Y. Dabin, J. Chavanne, O. Hignette, C. Morawe and C. Borel, *J. Synchrotron Radiat.* **12**, 659 (2005).
- [206] L.A. Grunes, *Phys. Rev. B* **27** (1983) 2111.
- [207] J.E. Müller, O. Jepsen, and J.W. Wilkins, *Solid State Communications*, **42** (1982) pp.365-368.
- [208] T. Westre, P. Kennepohl, J. G. DeWitt, B.Hedman, K. O. Hodgson, and E. I. Solomon, *J. Am. Chem. Soc.* **119** (1997), 6297-6314
- [209] V.I. Anisimov, F. Aryasetiawan and A.I. Lichtenstein, *J. Phys.: Condens. Matter* **9**, 767-808 (1997).
- [210] L. Uba, S. Uba, V.N. Antonov, T. Ślęzak, J. Korecki, and A.N.
- [211] A. Perlov, A. Yaresko, and V. Antonov, *PY-LMTO, A Spin-polarized Relativistic Linear Muffin-tin Orbitals Package for Electronic Structure Calculations*, unpublished.
- [212] V. Antonov, B. Harmon and Alexander Yaresko, *Electronic structure and magneto-optical properties of solids*, Kluwer Academic Publishers,Dordrecht, Boston, London (2004)
- [213] L.Wilk, M.Nusair, and S.H. Vosko *Can. J. Phys.* **58**, 1200 (1980)
- [214] P.E. Blochl, O. Jepsen and O. K. Andersen, *Phys. Rev. B* **49**, 1622316233(1994)
- [215] P. Blaha *et al.*, WIEN2K: An Augmented Plane Wave and Local Orbitals Program for Calculating Crystal Properties (Vienna University of Technology, Austria, 2001).
- [216] J.Kuneš, P. Novák, M. Diviš, and P. M. Oppeneer, *Phys. Rev. B* **63**, 205111 (2001)
- [217] D.D. Koelling and B N Harmon, *J. Phys. C* **10** 3107 (1977)
- [218] J.P. Perdew and Y. Wang, *Phys. Rev. B* **45**, 13 244 (1992)
- [221] J.P. Perdew, K. Burke, and M. Ernzerhof, *Phys. Rev. Lett.* **77**, 3865 (1996).

- [220] D. M. Ceperley and B. J. Alder, *Phys. Rev. Lett.* **45**, 566 (1980)
- [221] J.P. Perdew, K. Burke, and M. Ernzerhof, *Phys. Rev. Lett.* **77**, 3865 (1996).
- [222] X. Gonze *et al.*, Computer Phys. Commun. **180**, 2582-2615 (2009); Zeit. Kristallogr. **220**, 558-562 (2005).
- [223] Y. Joly, *Phys. Rev. B* **63**, 125120 (2001).
- [224] R. Torchio, Y.O. Kvashnin, S. Pascarelli, O. Mathon, C. Marini, L. Genovese, P. Bruno, G. Garbarino, A. Dewaele, F. Occelli, P. Loubeyre, *XMCD measurements in Ni up to 200 GPa: resistant ferromagnetism.*, *Phys. Rev. Lett.* **107**, 237202 (2011)
- [225] R.S. Sundar and S.C. Deevi, *Int. Mater. Rev.* **50** (2005) 157
- [226] T. Sourmail, *Prog. Mater. Sci.* **50** (2005) 816 2
- [227] R.E. Quigley, Proceedings of the IEEE Applied Power Electronics Conference, 1993, p. 906.
- [228] R. H. Victora and L. M. Falicov, *Phys. Rev. B* **30**, (1984) 259
- [229] W.C. Ellis and E.S. Greiner, *Trans ASM* (1941), 415-433.
- [230] T.Wakiyama, AIP Conf. Proc. Mag. Magn. Mater., **2** (1973) 921.
- [231] T. Nishizawa and K. Ishida, *Binary alloy phase diagrams*, vol. 2, 2nd ed. Metal Park (OH): ASM International; 1990:1186.
- [232] L. Kaufman , H. Nesor, *Z Metallkd* **64** (1973) 249.
- [233] G. Inden, Proc. Project Meeting CALPHAD V, Dusseldorf, **III** (1976) 41
- [234] M. Hillert, M.Jarl CALPHAD **2** (1978), 227.
- [235] F. Guillermet *High Temp-High Pressures*, **19** (1987) 477.
- [236] C.Colinet, G.Inden, R. Kikuchi, *Acta metall mater* **41**(1993)1109.
- [237] C.Colinet, A. Antoni-Zdziobek, *JOM* **52**(7) (2000) 26
- [238] I. Ohnuma, O. Ikeda, R.Kainuma , B.Sundman , K.Ishida *Z Metallkd* **89** (1998) 847.
- [239] I. Ohnuma, H. Enokia, O.Ikeda, R. Kainuma, H. Ohtani, B. Sundman, K. Ishida, *Acta Materialia* **50** (2002) 379-393
- [240] M. Shiga, *Solid State Communications* **10** (1972) 1233-1236
- [241] D.W. Clegg and R.A. Buckley, *Jour. Metal. Sci.* **7** (1973), pp. 48-54.

- [242] C.W. Chen, *J. Appl Phys* **32** (1961) 3, pp. 348S-355S.
- [243] L. Li, *J. Appl. Phys.* **79** (1996) 8, pp. 4578-4580.
- [244] J.E. Goldman and R. Smoluchowski, *Phys. Rev.* **75** (1949), pp. 310-311.
- [245] P. Weiss and R. Forrer, *Ann. Phys.* **12** (1929) 279.
- [246] D.I. Bardos, *Mean Magnetic Moments in bcc Fe-Co alloys*, *J. Appl. Phys.* 40 (1961) pp. 1371-1372.
- [247] C. Kuhrt, L. Schultz, *J. Appl. Phys.* **73** (1993) 6588-90.
- [248] J.Kaspar and D.R. Salahub, *J. Phys. F* **13** (1983) 311.
- [249] R.Richter and H.Eschrig, *J. Phys. F* **18** (1988) 1813.
- [250] H. Hasegawa and J. Kanamori, *J. Phys. Soc. Jpn.* **33** (1972) 1599; **33** (1972) 1607
- [251] N. Hamada, *J. Phys. Soc. Jpn.* **46** (1979) 1759
- [252] A. Diaz-Ortiz, R. Drautz, M. Fähnle, H. Dosch, and J. M. Sanchez, *Phys. Rev. B* **73** (2006) 224208
- [253] A.R. Williams, V.L. Moruzzi, A.P. Malozemoff, and K. Terakura, *IEEE Tran. Magn.* **MAG-19**, (1983) 1983
- [254] E.C. Sowa and L.M. Falicov, *Phys. Rev. B* **37** (1988) 8707
- [255] M.F. Collins, J.B. Forsyth, *Philos. Mag.* **8** (1963) 401.
- [256] A.W. Smith, R.D. Rawlings, *Phys. Stat. Sol. A* **34** (1976) 117-23.
- [257] J.S. Kouvel *Magnetism and Metallurgy*, Berkowitz De Kneller (eds). Academic Press, New York, NY, 1969, p. 547
- [258] B. Window, *J. Appl. Phys.* **44** (1973) 2853
- [259] D. Papantonis, W. A. Bassett, *J. Appl. Phts.* 48 (1977) pp. 3374-3378.
- [260] F.P. Bundy, *J. Appl. Phys.*, **36** (1967) 2446
- [261] F.P. Bundy, *Rev. Sci. Instrum.* **46**, 1318 (1975)
- [262] R.L. Clendenen and H.C. Drickamer, *J. Phys.* **33** (1962) 770
- [263] T.R. Loree, C.M. Fowler, E.G. Zukas, and F.S. Minshall, *J. Appl. Phys.* **37** (1966) 1918
- [264] <http://www.easylab.co.uk/index.asp>

- [265] M.D. Cooke, M.R.J. Gibbs, R.F. Pettifer, *Jour. Magn. Magn. Mat.* **237** (2001) pp. 175-180
- [266] A. Hammersley, S. Stevenson, M. Hanfland, A. Fitch, and D.Häusermann, *High Press. Res.* **14**, 235 (1996)
- [267] Rietveld,H.M.(1967). *Acta Crystallogr.*,**22**,151-2.
- [268] Rietveld,H.M.(1969). *J. Appl. Crystallogr.*,**2**,65-71.
- [269] A.C. Larson and R.B. Von Dreele, "General Structure Analysis System (GSAS)", Los Alamos National Laboratory Report LAUR 86-748 (2000)
- [270] B.H. Toby, EXPGUI, a graphical user interface for GSAS, *J. Appl. Cryst.* **34**, 210-213 (2001)
- [271] A. Le Bail, H. Duroy and J.L. Fourquet, *Mat. Res. Bull.* **23** (1988) 447-452.
- [272] A. Le Bail, *Powder Diffraction* **20** (2005) 316-326.
- [273] F. Birch, *Physical Review* **71** (11) (1947) 809-824.
- [274] T. Takahashi, W.A. Basset, and H.K. Mao, *J. Geophys. Res.* **73** (1968) 4717
- [275] C. Kittel, *Introduction to the Solid State*, Wiley (2004).
- [276] A. Díaz-Ortiz, R. Drautz, M. Fähnle, H. Dosch, and J. M. Sanchez, *Phys. Rev. B*, **B 73**, 224208 (2006)
- [277] G. Kresse and J. Furthmuller *Comput. Mater. Sci.* **6** (1996) 15
- [278] R.Torchio, S. Pascarelli, O. Mathon, C. Marini, S. Anzellini, P. Centomo, C. Meneghini, S. Mobilio, N.A. Morley and M.R.J. Gibbs, *High Pressure Research* **31** (2011) 148-152